UNIVERSITÀ DEGLI STUDI DI PADOVA
DIPARTIMENTO DI INGEGNERIA CIVILE, EDILE E AMBIENTALE
Department Of Civil, Environmental and Architectural Engineering

Corso di Laurea Magistrale in Ingegneria Civile

TESI DI LAUREA

DAMAGE-FRICTIONAL CONSTITUTIVE MODEL WITH CHEMICAL DEGRADATION FOR INTERFACE ELEMENTS IN CEMENT-BASED MATERIALS

Relatore:
Chiar.ma PROF. GIOVANNA XOTTA
Correlatori:
Chiar.ma PROF. VALENTINA SALOMONI
Chiar.mo PROF. CARLOS LÓPEZ
Chiar.mo PROF. IGNACIO CAROL

Laureando: NICOLÒ TOGNON
2036529

ANNO ACCADEMICO 2023-2024

Ai miei genitori

Abstract

Keywords
Interface elements
Constitutive law
Fracture mechanics
Chemical degradation

One of the alternatives proposed to cope with global warming is the injection of carbon dioxide (CO_2) into deep geological formations through a process known as Carbon Capture and Storage (CCS). Due to their geological characteristics, disused hydrocarbon reservoirs are suitable for CO_2 storage. However, these reservoirs are often crossed by abandoned wells, in which ordinary Portland cement has been used to make the various seals. Due to the alkaline nature of the hardened Portland cement paste and the acidity of the surrounding environment, as a result of CO_2 injection, chemical degradation processes of the material can be triggered. It is therefore of fundamental importance to understand the physical and chemical phenomena involved in the problem in order to be able to model them with sufficient accuracy.

Within the framework of the finite element method (FEM), zero-thickness interface elements are frequently used to model physical discontinuities and cracking of quasi-brittle materials under fracture processes caused by mechanical actions. However, it is difficult to find formulations that also include softening of the material due to chemical processes, as for example occurs in the cement paste used in the sealing of old oil wells, which are exposed to acid attack when the reservoirs are subsequently used for CO_2 storage. Recently, within the MECMAT-UPC group, a law was proposed based on the theory of elasto-plasticity that incorporates the effect of degradation of material strength parameters due to chemical processes. However, this law has limitations for the simulation of interface element behaviour under load-unload-reload cycles, due to the fact that in real cases, in pure tensile or tensile-shear states, when unloading occurs, the cracks close either completely or partially, which cannot be represented by an elasto-plastic law in which unloading occurs according to the direction of initial stiffness. This effect leads to unrealistic compression states at the time of unloading.

To improve aspects of the original model's response in load-unload-reload situations, a constitutive model for interface elements has been proposed in which cohesive behaviour based on scalar damage theory, on one side, and frictional behaviour with dilatancy, on the other, are combined in a parallel coupled formulation.

The aim of the present thesis work is the extension of the cohesive-frictional law in order to incorporate the effect of degradation of material strength parameters due to chemical processes. For this purpose, the fracture process is governed by two history variables: one internal, representing the degradation associated with the fracture processes, taken into account with an isotropic damage variable, and the other external, representing the degree of chemical degradation, which varies between values zero (undegraded material) and one (completely degraded material). The behaviour of the law has been verified by means of constitutive examples under some typical loading states: pure tensile, tensile-shear and shear with constant compression, combined with different chemical degradation sequences.

Riassunto

Una delle alternative proposte per affrontare il riscaldamento globale è l'iniezione di anidride carbonica (CO_2) in formazioni geologiche profonde attraverso un processo noto come Carbon Capture and Storage (CCS). In virtù delle loro caratteristiche geologiche, i giacimenti di idrocarburi dismessi sono adatti allo stoccaggio di CO_2. Tuttavia, questi giacimenti sono spesso attraversati da pozzi abbandonati, nei quali è stato utilizzato del comune cemento Portland per realizzare le varie sigillature. A causa della natura alcalina della pasta di cemento Portland indurita e dell'acidità dell'ambiente circostante, come risultato dell'iniezione di CO_2, si possono innescare processi di degradazione chimica del materiale. Pertanto, è di fondamentale importanza comprendere i fenomeni fisici e chimici coinvolti nel problema per poterli modellare in maniera sufficientemente accurata.

Nell'ambito del metodo degli elementi finiti (FEM), gli elementi di interfaccia a spessore nullo sono frequentemente utilizzati per modellare le discontinuità fisiche e la fessurazione di materiali quasi-fragili in seguito a processi di frattura causati da azioni meccaniche. Tuttavia, difficilmente si trovano formulazioni che includano anche il rammollimento del materiale dovuto a processi chimici, come ad esempio avviene nella pasta di cemento utilizzata per la sigillatura di vecchi pozzi petroliferi, esposti all'attacco acido quando i giacimenti vengono successivamente utilizzati per lo stoccaggio di CO_2. Recentemente, all'interno del gruppo MECMAT-UPC, è stata proposta una legge basata sulla teoria dell'elasto-plasticità che incorpora l'effetto della degradazione dei parametri di resistenza del materiale dovuta a processi chimici. Tuttavia, questa legge presenta delle limitazioni per la simulazione del comportamento degli elementi interfaccia sotto cicli di carico-scarico-ricarico, a causa del fatto che nei casi reali, negli stati di trazione pura o di trazione-taglio, quando si verifica lo scarico, le fessure si chiudono completamente o parzialmente, aspetto che non può essere colto da una legge elasto-plastica in cui lo scarico avviene secondo la direzione della rigidezza iniziale. Questo effetto porta a stati di compressione non realistici al momento dello scarico.

Per migliorare gli aspetti della risposta del modello originale in situazioni di carico-scarico-ricarico, è stato proposto un modello costitutivo per elementi interfaccia in cui si combina, in una formulazione accoppiata parallela, da un lato, un comportamento coesivo basato sulla teoria del danno scalare e, dall'altro lato, un comportamento di attrito con dilatanza.

Lo scopo del presente lavoro di tesi è l'estensione della legge coesivo-attrattiva al fine di incorporare l'effetto del degrado dei parametri di resistenza del materiale dovuto a processi chimici. A questo scopo, il processo di frattura è governato da due variabili di storia: una

interna, che rappresenta il degrado associato ai processi di frattura, presi in considerazione con una variabile di danno isotropa, e l'altra esterna, che rappresenta il grado di degradazione chimica, che varia tra i valori zero (materiale non degradato) e uno (materiale completamente degradato). Il comportamento della legge è stato verificato mediante esempi a livello costitutivo sotto alcuni stati di carico tipici: trazione pura, trazione-taglio e taglio con compressione costante, combinati con diverse sequenze di degradazione chimica.

Acknowledgements

I would like to thank everyone that has been linked in any way to this thesis and contributed to its realization in different ways.

First of all, I would like to express my deepest gratitude to Professor Carlos López for guiding me throughout this Master Thesis period. I appreciate all of his contributions,starting with the amount of time he has spent on me during these months, the new ideas he proposed to me, the patience and the explanations he gave me on a daily basis with constancy, to make this experience productive and stimulating. I would also like to thank Professor Ignacio Carol: he was the person without whose availability all this would not have been possible. I also thank him for enriching this thesis with valuable advice.

Special thanks go to Professor Giovanna Xotta. Thanks for solving many problems personally, being always available in any eventuality, but above all for organising with Professor Carol the internship at the UPC. I would also like to thank Professor Valentina Salomoni who informed me about the possibility of a thesis experience abroad and took an interest in the matter.

Now I want to thank those who have become my friends during this experience. I can only begin by thanking Hao, the best office mate I could have had, Laurin, Lluís and Diego, partners of a thousand adventures, David, the gymbro, Paul, Alex and Natalia for all the lunches we shared together. Special thanks to Laura and Lucia who, besides hosting me in their office in the first few days, were always available to help me with any problem. I also thank Win Feng, Andreu, Jan Thao, David E. for all the good times we spent together. I thank Caterina, who introduced me to all. Thank you all for making me feel welcomed into this wonderful group.

I want to thank the girls with whom I shared their home during this time and who taught me a lot: María in Plaça del Raspall and Nago and Marta in Carrer de Terol.

Finally, I would like to thank my family, especially my mum and dad, for their support and endless love that has been shown to me during all these months.

Contents

Chapter 1

Introduction

One of the proposed alternatives to cope with global warming is the carbon dioxide (CO_2) injection into deep geological formations through a process known as Carbon Capture and Storage (CCS). Due to their geological characteristics, disused hydrocarbon reservoirs are suitable for storing CO_2 (Metz et al. 2005). However, these reservoirs are often crossed by abandoned wells, in which common Portland cement has been used to make the various seals. Due to the alkaline nature of the hardened Portland cement paste and the acidity of the surrounding environment, as a result of CO_2 injection, chemical degradation processes of the material can be triggered (Gasda, Bachu, and Celia 2004). Therefore, it is of fundamental importance to comprehend the physical and chemical phenomena involved in the problem in order to be able to model them with sufficient accuracy.

Within the finite element method (FEM), zero-thickness interface elements are frequently used to model physical discontinuities and cracking of quasi-brittle materials under fracture processes caused by mechanical actions. However, formulations that also include softening of the material due to chemical processes, as for example occurs in the cement paste used in the sealing of old oil wells, exposed to acid attack when the reservoirs are subsequently used for CO_2 storage, are hardly found. Recently, within the UPC group, a constitutive law based on the theory of elasto-plasticity has been proposed that incorporates the effect of degradation of material strength parameters due to chemical processes (Martínez et al. 2022). However, this law has limitations for simulating interfaces behaviour under load-unload-reload cycles, because in real cases, in pure traction or traction-shear states, upon unloading, cracks close completely or partially, which cannot be represented by an elasto-plastic law in which unloading occurs in the direction of the initial stiffness. This effect leads to unrealistic compression states upon unloading.

To improve aspects of the original model's response in load-unload-reload situations, an interface constitutive model has been proposed in which cohesive behaviour based on scalar damage theory, on the one hand, and frictional behaviour with dilatancy, on the other hand, are combined in a parallel coupled formulation.

1.1 Motivation and objectives

Taking into account the above, the main motivation of this master's thesis project is to improve the behaviour of the cohesive-frictional interface constitutive law in the presence of chemical processes. The main objective of the present thesis work is the extension of an existing interface constitutive law within the MECMAT-UPC group, which combines, on the one hand, a cohesive behaviour and, on the other hand, a frictional behaviour with dilatancy, in order to incorporate the effect of degradation of material strength parameters due to chemical processes.

The main specific objectives include the following:

1. to understand fracture phenomena in quasi-brittle materials such as concrete and rock;
2. to become familiar with the tools of the research group (MECMAT), in particular the subroutines of interface constitutive laws;
3. to incorporate into the available cohesive type constitutive law, based on scalar damage theory, the effect of the degradation of material strength parameters due to chemical processes. For this purpose, two history variables governing the fracture process are defined, one internal, representing the degradation associated with fracture processes that are taken into account with an isotropic damage variable, and the other external, representing the amount of chemical degradation that varies between values zero (non-degraded material) and one (completely degraded material);
4. to adopt a constitutive law that allows to simulate a Coulomb type frictional behaviour (without cohesion) with dilatancy;
5. to verify the behaviour of the model through numerical simulations of simple traditional tests such as pure tensile, tensile combined with shear and shear with constant compression compared to different sequences of chemical degradation.

1.2 Methodology

The development of this master thesis is carried out within the research group MECMAT (Mechanics and Nanotechnology of Engineering Materials) of the Polytechnic University of Catalonia (UPC). One of the main research topics of this group is the modelling of fracture in the field of concrete and rock mechanics, both under mechanical and environmental actions, and the combination of these (P. C. Prat et al. 1993; López 1999; Caballero, López, and Carol 2006; Caballero, Carol, and López 2007; Segura and Carol 2008; Idiart, López, and Carol 2011; Liaudat, López, and Carol 2018).

The literature review focused first on the safety aspects of carbon dioxide storage reservoirs, in particular on the evaluation of well sealing elements made of ordinary Portland cement.

Subsequently, deeper understanding of cracking theories and models, in particular models of discontinuity behaviour, has been developed. Familiarisation with the research group's interface tools and constitutive laws included solving examples of the elasto-plastic law (Carol, P. C. Prat, and López 1997) and the cohesive-frictional law (Puiggrós 2017), before addressing the incorporation of the effect of chemical degradation in the second of these laws.

For the implementation of the new constitutive law, a series of two-dimensional analysis subroutines have been used, called by a main program that performs an iterative process when some prescribed degrees of freedom coincide with the stresses. These subroutines, once verified, can be incorporated into a finite element based calculation program.

Once the correct operation of the new law subroutines has been verified, numerical tests have been performed under different typical loading states combined with different chemical degradation sequences.

1.3 Thesis content organisation

In addition to this introductory chapter, the content of the thesis has been organised into the four chapters summarised below:

- Chapter 2. Literature review. The concepts of Carbon Capture and Storage and the main characteristics of acid attack on oil well cementations made with ordinary Portland cement, when exposed to carbonated water from CO_2 injection, are briefly described. Next, the main aspects of the mechanical behaviour of quasi-brittle materials such as concrete or rock are presented. Finally, the main concepts of Fracture Mechanics and the existing cracking approximation models in the literature are described in order to introduce the theoretical basis of the behaviour of interface elements used in the modelling of discontinuities;
- Chapter 3. Interface constitutive laws. The concept of the zero-thickness interface element used to simulate discontinuities in materials, present in many practical concrete engineering problems, is presented. First, the interface constitutive law proposed by Carol, P. C. Prat, and López (1997), formulated in the framework of elastoplasticity theory, which includes fracture mechanics concepts and fracture energy parameters, is briefly described. Subsequently, the constitutive model combining cohesive behaviour based on scalar damage theory with frictional behaviour with dilatancy is presented, incorporating the effect of chemical degradation on the material strength parameters due to acid attack;

- Chapter 4. Results. This chapter presents the results of the interface model obtained from the combination of the damage and friction models with the addition of chemical degradation. The behaviour of the law has been verified through constitutive examples under some typical loading states: pure tensile, tensile-shear and shear with constant compression, combined with different sequences of chemical degradation;
- Chapter 5. Summary, conclusions and future work. The conclusions of this work and some considerations for possible future research are presented.

Finally, in the References section, the bibliographical sources consulted during the development of this thesis are listed.

Chapter 2

Literature review

This chapter sums up the main aspects of the state of knowledge in which this work is framed. First, the basic concepts and main characteristics of carbon dioxide capture and storage in geological formations are briefly presented, followed by a discussion of the main aspects of wells and possible related fluid leakage (Section 2.1).

In Section 2.2, the main characteristics of acid attack in well cement due to interaction with carbon dioxide are described, the carbonation mechanism and the chemical reactions involved are presented. The approach used follows the review works of Shukla et al. (2010), Zhang and Bachu (2011), Choi et al. (2013), Carroll et al. (2016), and Bagheri, Shariatipour, and Ganjian (2018), as well as the technical report of the United Nations Intergovernmental Panel on Climate Change (IPCC) (Metz et al. 2005).

Finally, in Section 2.3, the main concepts of Fracture Mechanics are discussed to introduce the theoretical basis of the behaviour of zero-thickness interface elements, whose constitutive law is presented in this work.

2.1 Carbon and Capture Storage

The Carbon and Capture Storage (CCS) process is a set of technologies that, among other processes, includes (Metz et al. 2005):

- the capture and separation of CO_2 from large sources generated by human activity (e.g. power plants or cement factories);
- CO_2 transport, usually through pipelines;
- long-term storage of CO_2 through injections into geological formations, between one and four kilometres deep (Bachu 2003; Zhang and Bachu 2011), such as aquifers or depleted oil or gas reservoirs. In general, these reservoirs are composed of almost impermeable rock layers (caprock), which allow storage and prevent possible escape paths to the upper layers.

Suitable sites for storage include depleted oil or gas reservoirs, deep saline aquifers and coal deposits. CO_2 storage in exhausted oil and gas reservoirs is a very promising procedure.

This option is very promising firstly because the hidrocarbons that have originally formed and accumulated have not escaped, in some cases for millions of years, which demonstrates their integrity and security; more specifically, the particular security against fluid leakage is guaranteed by the fact that these natural deposits within the ground are enclosed within a layer of material characterised by a very low permeability. Secondly, because the extensive studies (geologic, geophysical, petrological, etc.) made for oil exploitation purpose, provide very valuable information which would be very expensive to obtain in other sites. However, on the negative side, the security evaluation of many of these disused oil deposits for CO_2 storage purposes raises a major concern: the presence of abandoned wells that cut through the impermeable rock layer that makes up the reservoir and that may constitute potential leakage pathways.

In many cases, the closure of abandoned wells started decades ago, when carbon dioxide storage had not yet been considered, and the main materials used for the steel pipe casing and/or concrete plug used to close the well were Portland cements or cement slurries. Hydrated cement paste (HCP) is thermodynamically unstable in carbon dioxide-rich environments (Robins and Milodowski 1986): this can lead to changes in chemical and physical properties, potentially affecting the integrity and safety of the fluid storage due to the formation of leakage pathways to the surface, other reservoirs or adjacent aquifers (Gasda, Bachu, and Celia 2004). If the hydrated cement paste in the abandoned well comes into contact with the injected CO_2, two possible outcomes can be expected (Duguid and Scherer 2010):

1. if the hydrated cement paste is not immersed in water, a process similar to the carbonation of concrete under normal conditions will occur, leading to a slight increase in the strength of the paste and a decrease in its permeability (Kutchko, Strazisar, Dzombak, et al. 2007; Kutchko, Strazisar, Lowry, et al. 2008; Rimmelé et al. 2008);
2. if the hydrated cement paste is immersed in water or brine, which is the most likely long-term scenario in an abandoned well, it will suffer a progressive decalcification process, called acid attack, leading to a drastic loss of mechanical strength and an increase in permeability (Carey et al. 2007; Kutchko, Strazisar, Dzombak, et al. 2007; Kutchko, Strazisar, Lowry, et al. 2008; Rimmelé et al. 2008; Duguid and Scherer 2010; Duguid, Radonjic, and Scherer 2011; Walsh et al. 2013).

Carbon dioxide outflow pathways can be of natural character, e.g. fault reactivation, ground cracks, induced seismicity (Hawkes, McLellan, and Bachu 2005; Orlic 2009; Rutqvist 2012), or of artificial character, mainly due to the presence of wells (Figure 2.1). The evolution over time of the effective stresses in a reservoir due to fluid injection or extraction, combined with the fact that well cementing is performed at different times, can lead to significant changes in the stresses in the system (Mainguy et al. 2007). These stresses can cause cracks to spread, in particular at the interface between the rock formation and the cement, between the casing and the cement, and finally between the casing and the

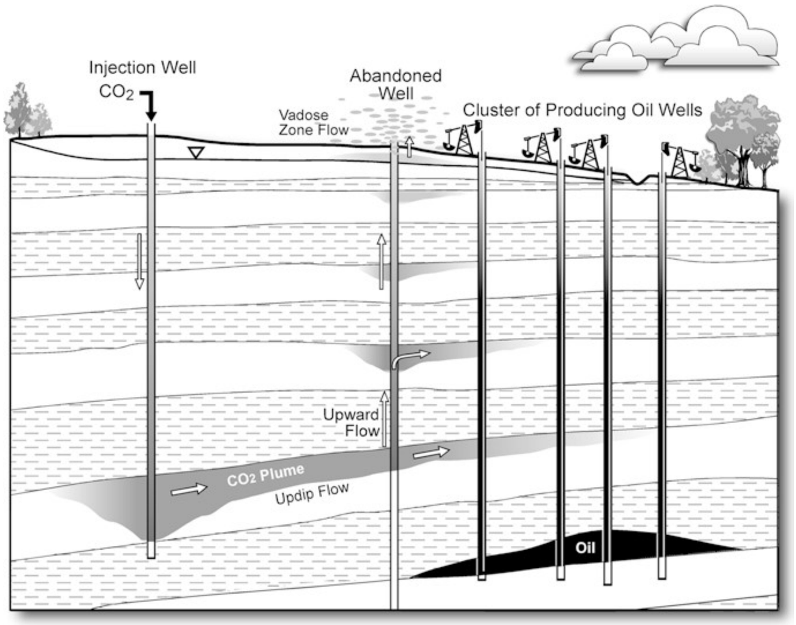

Figure 2.1: Schematic representation of an injection well and of wells penetrating a geological formation (Gasda, Bachu, and Celia 2004).

cement plug that is set after abandonment of the well (Gasda, Bachu, and Celia 2004). If carbonate brine penetrates the cracks that have been created, the reduction in strength due to acid attack at the crack tip may induce crack growth and/or propagation, which may compromise the integrity of the entire well.

2.1.1 CO_2 injection

In the context of storage in geological formations, CO_2 is injected at pressures and temperatures sufficiently high to be in supercritical state (Onan 1984). The state of CO_2 as a supercritical fluid is identified at pressures and temperatures above 7.38 MPa and 31°C, respectively: these certain state conditions make carbon dioxide behave as a hybrid between a liquid and a gas, i.e. it can diffuse as a gas (effusion) and dissolve substances as a liquid (solvent). Above critical conditions, small variations in pressure and temperature produce large variations in the density values of the fluid. Supercritical fluids occupy much less volume and diffuse better than any conventional gas or liquid through the small pore spaces of the reservoir rock formation. However, at high pressures, carbon dioxide is less dense than oil but denser than hydrocarbon gases, so the injected carbon dioxide will naturally migrate to the top of the reservoir due to its buoyancy and diffuse laterally below the impermeable layer. Over time, the carbon dioxide will tend to gradually dissolve in the water present in the rock formation and will slowly sink, as it has a higher density than water.

2.1.2 Potential risks

Due to the large number of wells that penetrate reservoirs once used for oil and gas exploitation, the potential risk of fluid leakage is particularly high. These wells, constructed to extract and/or inject large volumes of fluid, penetrate deep into the reservoir's caprock layer. In the long term, the integrity of the wells is particularly important because of the potential for CO_2, in free phase or dissolved in the reservoir brine, to react with the well construction materials with which it comes into contact and trigger degradation mechanisms. The design and construction of these elaborate infrastructures are generally carried out within wide safety margins, which are also guaranteed by the use of high quality materials. The amount of care that goes into the construction of these works is very high, related to the level of risk and the performance that must be guaranteed during their service life. However, most CO_2 storage sites are characterised by the presence of old wells that were built when regulations were less restrictive, often using obsolete methods or materials (Gasda, Bachu, and Celia 2004). Well integrity can be compromised by structural imperfections that can be detected in both the pre-production and production phases. During these processes, the corrosion and dissolution mechanism, as well as the stresses to which they are exposed, can cause weakening of the well materials and subsequent damage (Teodoriu et al. 2013). The main causes of the risk of CO_2 leakage from the reservoir are as follows:

- pre-production stage:
  - damage to the rock formation due to the drilling of wells;
  - casing eccentricity;
  - inadequate disposal of drilling mud;
  - incomplete cementation and/or poor adhesion between the steel casing-concrete-rock formation. Bachu and Bennion (2009) measured the permeability of the space between the casing and the cement casting: in the case of a good connection, the intrinsic permeability was 10^{-21} m^2, but when the connection was ineffective, then the permeability increased by five to six orders of magnitude;
  - shrinkage phenomenon of cement during the hydration process.
- production stage:
  - mechanical stresses in the concrete coating are often induced by variations in pressure and temperature due to production operations. Production cycles can lead to cracking over time (Asamoto et al. 2013);
  - the wells are exposed to aggressive environments, which may lead to degradation, in particular acid attack, of the materials and, consequently, to a change in their properties.

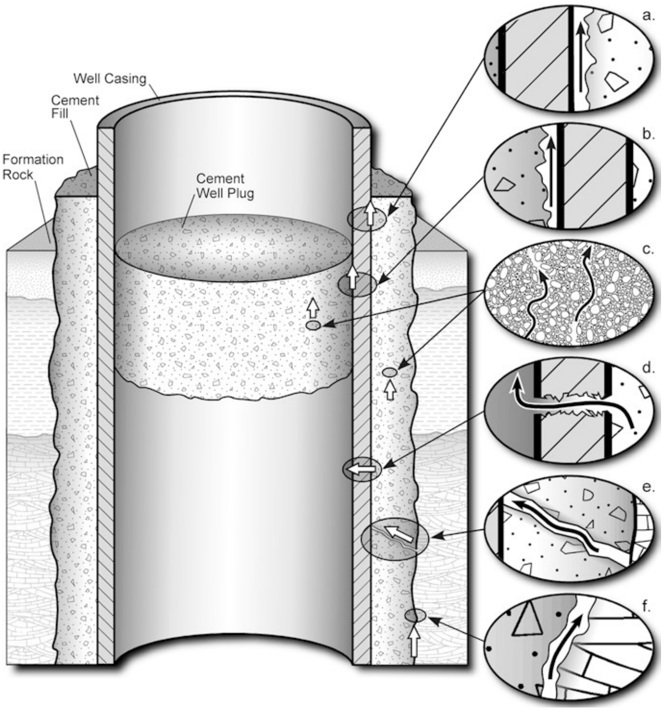

Figure 2.2: Possible leakage pathways for carbon dioxide in existing wells: (a. and b.) through steel-cement interface, (c.) through cement, (d.) through steel casing, (e.) through cracks in cement, and (f.) between cement and rock formation (Gasda, Bachu, and Celia 2004).

The risk of uncontrolled flow through the well as a consequence of its loss of integrity is potentially high. During these phases, the corrosion and dissolution mechanism, as well as the stresses present, can weaken the well material and cause it to fail (Teodoriu et al. 2013). If a CO_2 flow within the storage system reaches an old well, leakage can occur not only through the cement matrix, but also in other ways. These include (Figure 2.2) (Gasda, Bachu, and Celia 2004):

- damaged areas, defects, voids and permeable interfaces between the cement covering the well and the surrounding rocks;
- cracks and other defects in the walls and in the cement plug of the shaft;
- cracks and voids between concrete and steel casing;
- defects in the steel casing.

2.2 Chemical aspects of acid attack on well cement

Before describing the acid attack on hydrated cement paste (HCP), it is necessary to present in general terms the type of material used in oil well construction, its composition and microstructure.

2.2.1 Hydrated Portland cement paste

The clinker composition of Portland cement is mainly characterised by four phases (Nelson 1990):

- tricalcium silicate (Ca_3SiO_5 or C_3S in cement chemistry);
- dicalcium silicate (Ca_2SiO_4 or C_2S in cement chemistry);
- tricalcium aluminate (Ca_2AlO_6 or C_3A in cement chemistry);
- aluminatoferratotretacalcium aluminate ($Ca_4Al_2Fe_2O_{10}$ or C_4AF in cement chemistry).

When water is mixed with cement, hydration of the paste takes place during which C_3S and C_2S are converted into C−S−H gels and Portlandite ($Ca(OH)_2$), as follows:

$$\begin{aligned} 2\,Ca_3SiO_5 + 6\,H_2O &\longrightarrow Ca_3Si_2O_7 \cdot {}_3H_2O + 3\,Ca(OH)_2 \\ 2\,Ca_3SiO_4 + 4\,H_2O &\longrightarrow Ca_3Si_2O_7 \cdot {}_3H_2O + Ca(OH)_2 \end{aligned} \tag{2.1}$$

After hydration, the paste consists mainly of hydrated calcium silicate (C−S−H) and crystalline portlandite. The C−S−H phase consists of fibres or slow-growing needles responsible for the formation of a dense and strong matrix. While C−S−H is primarily responsible for increasing the cement strength, Portlandite offers little mechanical strength, being vulnerable to various agents, such as CO_2, although it is essential for maintaining an alkaline pH. Depending on chemical composition and/or fineness, cement used in well construction is classified into eight classes (A to H) by the American Petroleum Institute (API) (Nelson 1990). Of these, the most commonly used are class G and H cements.

2.2.2 General description of acid attack on hydrated cement paste

A problem regarding the integrity and safety of CO_2 geological storage is posed by Portland cement, which is commonly used in well cementing and plugging to create insulation between steel casing, cement and rock; the chemical reactions that occur in contact with carbonate water weaken the cement and alter its permeability. Contact between carbonate water and Portland cement produces a series of reaction fronts that divide the affected area into four zones (Kutchko, Strazisar, Dzombak, et al. 2007; Kutchko, Strazisar, Lowry, et al. 2008; Mason et al. 2013):

- unaltered zone: the hydrated cement paste remains unaltered. The pH is alkaline, approximately twelve, due to the content of Portlandite and alkaline ions;
- dissolution zone: characterised by the dissolution of Portlandite. The carbonate water/brine diffuses into the hydrated cement paste due to a difference in concentration gradients, lowering the pH of the pore solution, which causes the Portlandite to dissolve. This zone shows an increase in porosity compared to the unaltered zone, but not as much as the amorphous zone;
- carbonated zone: there are optimal conditions for calcite precipitation to occur (carbonation reaction). Degradation of the hydrated cement paste would not be a problem if the process were interrupted at this point, as the calcite temporarily provides a low permeability front; the decrease in permeability and porosity occurs in parallel with an increase in strength, which is slightly higher than in the unaltered zone;
- amorphous zone: the hydrated cement paste (pH approximately twelve, basic) is in direct contact with the carbonated water (pH approximately three, acidic). Once the Portlandite is exhausted, the calcite starts to dissolve due to the decrease in pH and the increase in CO_2 input. As long as the Portlandite is present, the pH remains alkaline, so the calcite remains mostly stable; however, when the Portlandite is depleted, the pH also decreases. As the calcite dissolves, the hydrated cement paste no longer can maintain an alkaline pH, so the hydrated calcium silicate becomes an amorphous silica gel. This new reagent has no structure, so that the hydrated cement paste is completely degraded in this area, with practically no mechanical strength and characterised by high permeability.

Acid attack alters the mechanical properties of the hydrated cement paste, causing a decrease in strength parameters such as the modulus of elasticity. In particular, it is observed that in areas of higher porosity, such as dissolution and amorphous zones, there is a decrease in these parameters, while in the area of lower porosity, such as carbonated and unaltered zones, the opposite occurs (Mason et al. 2013). There is some evidence of carbon dioxide migration between the annular spaces of the rock formation, cement casing, steel casing and cement plug interfaces in several field studies:

- extracting a sample from thirty years old well exposed to carbon dioxide in a reservoir used for oil extraction in Texas (CO_2 Enhanced Oil Recovery, EOR) (Carey et al. 2007);
- extracting a sample recovered from thirty years old well in a natural CO_2 producing reservoir (Crow et al. 2010).

2.2.3 Carbonation process in hydrated cement paste

The carbonation process of cement involves the dissolution of carbon dioxide in the interstitial water of the cement matrix, which reacts with calcium and hydroxyl ions to form calcium carbonate. The totality of the reactions involved can be described as follows (Papadakis, Vayenas, and Fardis 1991):

$$Ca(OH)_{2(s)} + CO_2 \longrightarrow CaCO_3 + H_2O \tag{2.2}$$

A theoretical model of the acid attack mechanism in hydrated cement paste under CO_2 storage conditions in geological formations was described by Kutchko, Strazisar, Dzombak, et al. (2007). The main stages that occur during acid attack on hydrated cement paste from abandoned wells are summarised below (Figure 2.3):

- stage 1: when carbon dioxide dissolves in the aqueous phase within the cement matrix, carbonic acid (H_2CO_3) is formed, leading to a decrease in pH, to a value of about three;
- stage 2: the initial pH within the cement matrix is alkaline, with a value of approximately twelve, due to the content of Portlandite and alkalis. Carbonated water diffuses into the matrix, causing the Portlandite to dissolve (zone 1 or dissolution zone in Figure 2.3(a)). The dissolution of the Portlandite causes an increase in the porosity of the zone and a calcium ion leaching out of the hydrated cement paste;
- stage 3: the transition between zone 1 and zone 2 is evident (Figure 2.3(b)). This front is characterised by the precipitation of calcite in the cement matrix, caused by the carbonation reaction. This precipitation is the result of the outward diffusion of calcium ion in the hydrated cement paste together with the inward diffusion of carbonate brine in the form of carbonate ion. Zone 2, or the carbonated zone, is the least porous along with the unaffected zone, since the available space left by stage 2 is filled with the precipitated solid, thus decreasing the porosity and permeability and increasing the hardness;
- stage 4: once the Portlandite is exhausted, the calcite begins to dissolve. As long as the Portlandite is present, the system maintains a pH above twelve and the most abundant part of carbon dioxide is the carbonate ion (CO_3^{2-}), so the calcite remains stable. However, when the Portlandite is depleted, the pH drops below 11 and the most abundant part becomes the bicarbonate ion (HCO_3^-). This forms calcium bicarbonate, which is soluble in water. This process is called bicarbonation, which is observed at the transition between zones 2 and 3 (Figure 2.3(b));
- stage 5: zone 3, or the amorphous zone, has already been through carbonation and bicarbonation and represents the end of the degradation of the hydrated cement paste. With the dissolution of the calcite, the system no longer can maintain pH and

> the hydrated calcium silicate remaining within the hydrated cement paste becomes an amorphous silica gel (Fabbri, Jacquemet, and Seyedi 2012).

The zones formed are the result of the equilibrium between the chemical dissolution and the aqueous parts shifting due to the gradient difference in concentration. Each zone represents the local equilibrium between the cement matrix and its interstitial water. In addition to chemical processes, carbonation is controlled by diffusion processes. The calcium carbonate zone remains in a dynamic front, as the diffusion of the carbonate water causes a decrease in pH, leading to the dissolution of the previously precipitated calcium carbonate; at the same time, in the proximity, the carbonate water dissolves the portlandite, increasing the pH in the zone.

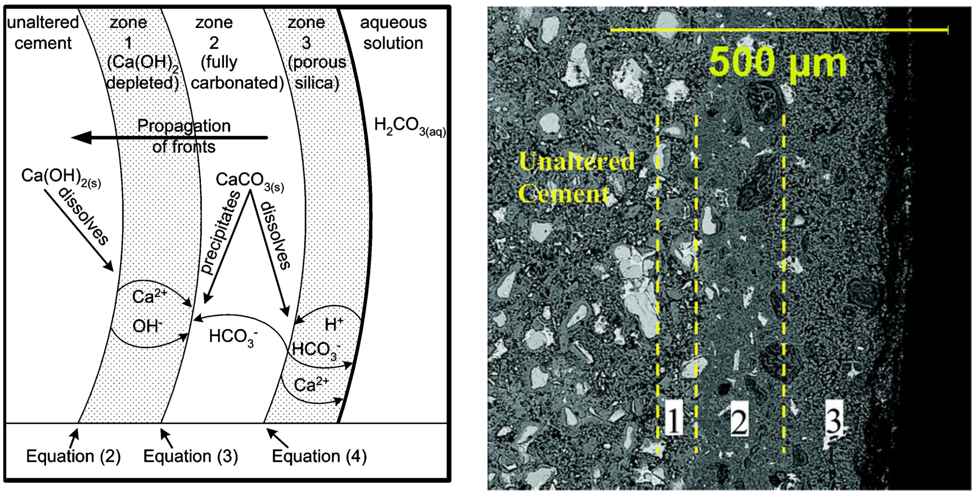

(a) (b)

Figure 2.3: (a) plot showing dissolution, calcium migration and formation of distinct zones in the cement. (b) SEM-BSE image of cement cured for 28 days at 50 °C and 30.3 MPa and exposed for 9 days to aqueous CO_2 at 50 °C and 30.3 MPa. This figure illustrates the typical degradation observed. The degraded region can be divided into three distinct zones, which are described in detail in the text (Kutchko, Strazisar, Dzombak, et al. 2007).

2.2.4 Factors affecting the rate of carbonation process

The rate of carbonation is affected by several factors that control the physical and chemical properties of the cement paste, such as the type of cement, the combination of certain additives with Portland cement that improve its resistance to acidity (Carroll et al. 2016), the water/cement ratio and the hardening conditions. The rate of carbonation is also affected by the conditions under which it occurs, such as temperature, carbon dioxide concentration, the state in which the CO_2 is present, the composition of the surrounding rocks and the exposure time.

2.3 Cracking theories and models

Numerical modelling of quasi-brittle materials' mechanical behavior has followed two main theoretical approaches: smeared approach based on continuum mechanics, and discrete approach based on fracture mechanics. The characteristics of these are summarised below.

2.3.1 Smeared approach based on Continuum Mechanics

The mechanics of the continuum is the most classical way of representing the behaviour of a material by using the stress-strain laws (σ-ϵ), also known as the constitutive equations. The concept of continuous deformations also extends to the softening branch, interpreting strain as the average strain of the material including the presence possible cracks and discontinuities.

2.3.1.1 Non-Linear Elasticity

The first theories were based on linear elasticity; however, linear elasticity is too limited to correctly describe the behaviour of materials such as concrete or rock. Nonlinear elastic models represent the material behaviour more accurately; however, they may have limitations in the formulation of quasi-brittle materials, whose behaviour depends on the loading history and is different in loading and unloading situations.

2.3.1.2 Elasto-plastic Models

The stress-strain behaviour is expressed as the sum of a total recoverable, or elastic, deformation and a non-recoverable, or plastic, deformation. The consideration of internal variables, whose evolution depends on the plastic deformations, allows a non-linear behaviour of hardening, softening, path dependence, unloading and reloading (Figure 2.4(a)). This approach has been successfully used in quasi-brittle materials, as they exhibit highly irreversible processes in advanced states of loading.

2.3.1.3 Models based on Elastic Damage Theory

Elastic degradation frameworks are characterised by an independent secant stiffness tensor consisting of twenty-one components, with corresponding evolution laws (Carol, Rizzi, and Willam 1994). The problem can be simplified by using damage variables that characterise the degradation state in a simpler way. These damage variables simulate at the macroscopic level the progressive elastic degradation due to the propagation and interconnection of microcracks and pores. This model assumes that no plastic behaviour is developed, in other words, that a linear secant elastic law is followed at unloading, with no residual deformation remaining (Figure 2.4(b)).

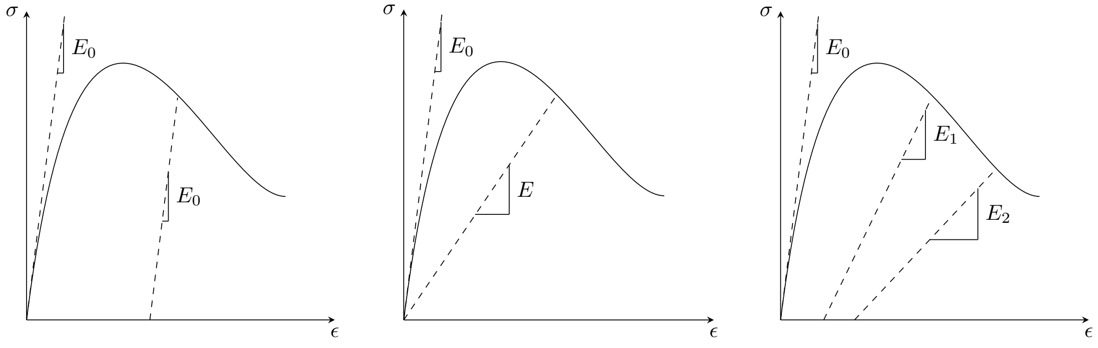

(a) Plastic behaviour (b) Damage behaviour (c) Real coupled behaviour

Figure 2.4: Different mechanical behaviour depending on the material: (a) elasto-plasticity, (b) damage, (c) combination of plasticity and damage.

2.3.1.4 Other approaches

Models based on elastoplasticity and elastic damage theory represent the two extremes of material representation as simplifications of what is observed experimentally. The behaviour followed by quasi-brittle materials presents an intermediate characteristic in which both effects occur: stiffness degradation and residual plastic deformations (Figure 2.4(c)).

2.3.2 Discrete Approach based on Fracture Mechanics

Fracture mechanics is a branch of mechanics that studies the formation and/or propagation of fractures or defects in materials and analyses the evolution of their stresses and strains. Two types of formulation of the basic principles of fracture mechanics can be identified: linear elastic fracture mechanics (LEFM) and non-linear fracture mechanics (NLFM).

2.3.2.1 Linear Elastic Fracture Mechanics

Linear elastic fracture mechanics (LEFM) is based on analytical solutions of the stress distribution at the apex of a crack, assuming that:

1. the crack apex is infinitesimal;
2. at the crack apex the stresses become singular (infinite), with a finite rate of energy dissipation taking place at that point of zero dimension;
3. is applicable to materials which, except for the crack apex singularity, in the rest of the domain satisfy Hooke's law.

The presence of irregularities, in the form of discontinuities in the material, causes an increase in stresses at the edges of the discontinuity, known as stress concentration. Stress concentrations are due to the redistribution of the force lines inside the material when a discontinuity is present (Figure 2.5). The most relevant contributions to this theory

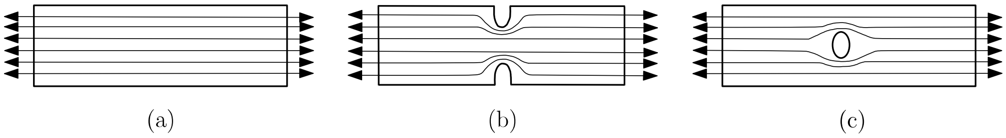
(a) (b) (c)

Figure 2.5: Stress flow lines in a plate subjected to uniform tensile stress (a) with no notch, (b) with some notches in the material and (c) with a hole in the centre.

are attributed to the work developed by Inglis (1913), Griffith (1921), Irwin (1958) and Timoshenko and Goodier (1970).

Fracture mechanics considers three fundamental modes of crack propagation:

- opening mode or Mode I, in which the crack faces are separated almost parallel to each other. It is assumed that only tensile stresses develop on the crack surface, in this mode;
- sliding mode or Mode II, in which the crack faces slide past each other. It is assumed that, on the crack surface, only tangential stresses can be generated in this mode;
- shear mode or mode III, where the crack faces slide laterally on each other. It is assumed that only tangential stresses also develop on the crack surface also in this case.

Figure 2.6 shows the three fundamental modes of crack propagation in the material. In practice, fracture of the material can occur in Mode I or, in general, as a combination of these three fundamental modes of kinematic crack propagation, which in this case is called mixed fracture mode.

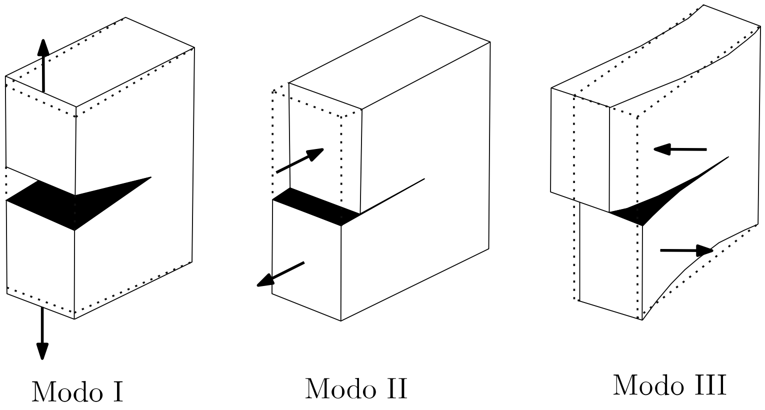

Figure 2.6: Three basic kinematic modes of crack opening.

In summary, linear elastic fracture mechanics is particularly suitable in cases where there is a single defect, as the energy is dissipated only at the crack tip and the rest of the continuum remains elastic (Karihaloo 1995). Therefore, for quasi-brittle materials, such as concrete or rock, where single isolated cracks do not occur, but are characterised by distributed micro-cracks, branching and bridging of the crack in the Fracture Process Zone (FPZ), it has a very limited application; however, it can be used for large structures where the effects on the FPZ are negligible.

2.3.2.2 Non-Linear Fracture Mechanics

Non-linear fracture mechanics (NLFM) is a more suitable approach for quasi-brittle materials, since it considers that inelastic processes occur along an area called the fracture process zone, whose dimensions are related to the size of the material's heterogeneity. If the fracture process zone is very small compared to the size of the structure, linear fracture mechanics is still applicable and its predictions are acceptable; however, if it is too large compared to the structure, and therefore non-negligible, then non-linear fracture models must be used.

Fictitious Crack Model

The Hillerborg, Modéer, and Petersson (1976) model or Fictitious Crack Model (FCM) is based on the work previously developed by Dugdale (1960) and Barenblatt (1962). This model assumes that the effects of microcracking in the fracture process zone (FPZ) are concentrated on a fictitious line of zero-thickness extending from the pre-existing crack. Along this line, the stresses increase from zero from the pre-existing crack tip to the value of the material's uniaxial tensile strength, f_t, at the fictitious crack tip: this causes the faces of the fictitious crack to gradually close towards the tip (Figure 2.7(a)). It is assumed that the crack propagates once the stress at the apex reaches the value f_t. When the crack starts to open, the stress decreases progressively as the crack opening r_N increases, according to a decay law. When the interface opening reaches the value of $\bar{r}_N$ the stress drops to zero (Figure 2.7(b)). When the crack has not yet reached $\bar{r}_N$, meaning $r_N < \bar{r}_N$, it corresponds to a point in the fracture process zone still characterised by a certain resistance. The amount of energy consumed per unit crack area, as the crack width increases from zero to $\bar{r}_N$, must be equal to the fracture energy G_f (geometrically equal to the area under the curve in Figure 2.7(b)), in other words:

$$G_f = \int_0^{\bar{r}_N} \sigma(r_N)\, dr_N \tag{2.3}$$

The Fictitious Crack Model, unlike traditional fracture mechanics, not only predicts the propagation of an existing rift, but also allows to predict crack initiation: in this way, it allows to determine the behaviour of initially uncracked materials.

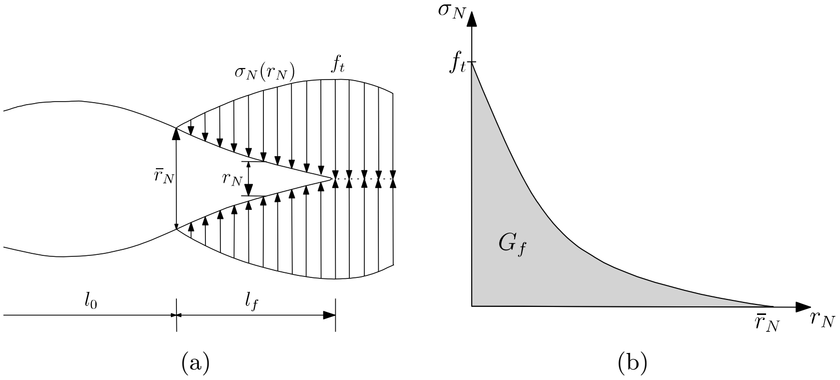

Figure 2.7: Hillerborg, Modéer, and Petersson (1976) Fictitious Crack Model: (a) stress distribution in the fictitious crack and (b) crack opening curve in the normal crack direction as a function of normal stress, where the fracture energy is the area under the curve.

Crack Band Model

The Crack Band Model (CBM) was originally introduced by Bažant (1976) and further developed by Bažant and Cedolin (1979) and Bažant and Oh (1983). This model considers that the fracture process does not develop in a thin and continuous band, but in an area of a certain width h, in which microcracking, branching and bridging processes take place. The band width is assumed to be a material property that can be related to the microstructure of the concrete (Figure 2.8(a)). The law in the plastic field (softening) is formulated as a stress-strain relationship (Figure 2.8(b)), although the latter is related to the inelastic displacement r_N and the fracture energy G_f.

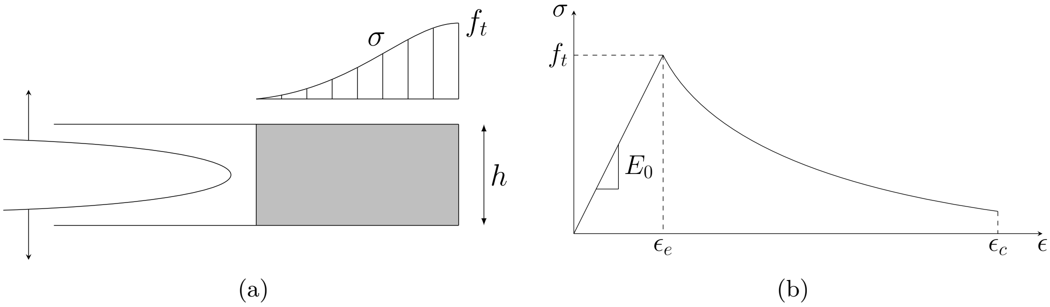

Figure 2.8: Crack Band Model: distribution of microcracks in a band of width h (a) and stress-strain diagram (b).

The application of the two non-linear fracture theories, the Fictional Crack Model and the Cracking Band Model, in the computational domain using the Finite Element Method results in two different numerical approaches to fracturing: the first is used in the discrete cracking approach, while the second is used the context of the smeared crack approach.

2.4 Discontinuity behaviour models

Quasi-brittle materials, such as concrete, maintain a certain strength when cracked due to various localised phenomena in the discontinuities, as shown by the softening branch in tension, frictional sliding or aggregate interlocking. Due to the heterogeneity of the material, the cracking tendency is not planar and shows irregularities, bridges and branches with crack faces characterised by roughness. This causes a coupling between normal and shear stresses under the action of tangential relative sliding, accompanied by a separation of the crack faces: this phenomenon is called dilatancy. Therefore, in the numerical analysis of engineering problems it is often necessary to adequately model the behaviour of interfaces and discontinuities. Initially, several analytical or numerical models considered some partial aspects of the problem, such as crack opening due to normal stresses only (Borst and Nauta 1985; Rots 1988), modelling of the Fracture Process Zone in Mode I (Hillerborg, Modéer, and Petersson 1976; Hillerborg 1978), modelling following Coulomb-type friction laws (Bažant and Gambarova 1980; Walraven 1980; Walraven and Reinhardt 1981). Literature provides some examples of interface laws that consider various complex aspects of mechanical behaviour, such as the coupling of normal and shear effects incorporating fracture concepts, dilatancy effects, response to cyclic actions, crack closure and reopening.

2.4.1 Interface constitutive models based on elasto-plasticity

Interface elements were originally introduced in the late 1960s and early 1970s due to the need to model discontinuities in rock masses. The fundamental aspect of these elements is the constitutive law, since it characterizes the opening and sliding criteria of a crack and its evolution. Based on the pioneering proposal of Goodman, Taylor, and Brekke (1968) and the subsequent advances made by various authors, such as Zienkiewicz et al. (1970), Ghaboussi, Wilson, and Isenberg (1973), Desai et al. (1984), Gens, Carol, and E. Alonso (1989), Gens, Carol, and E.E. Alonso (1995), the interface element formulation has been widely implemented in Finite Element codes and has been applied to numerous practical rock and concrete engineering problems. These laws have also been used, for example, to simulate interface elements in dynamic analysis of dams (Hohberg 1992), aggregate-mortar interfaces in mesostructural analysis of concrete (Vonk 1992; Stankowski, Runesson, and Sture 1993), between mortar and brick (Lotfi and Shing 1994), in fiber reinforced composites (Weihe, König, and Kröplin 1994), among others.

Since about twenty-five years ago, the MECMAT-UPC research group has been developing an elasto-plastic model to simulate the constitutive behaviour of interface-type elements for quasi- brittle materials. Starting from the original formulation (Carol and P. C. Prat 1990; Carol and P. Prat 1991), new proposals and improvements have been incorporated over time in Carol, P. C. Prat, and López (1997), Carol, López, and Roa (2001), López (1999), Caballero, K. Willam, and Carol (2008), López, Carol, and Aguado (2008), among others. A comparison with other models mentioned in the previous paragraph can be found in Carol, P. C. Prat, and López (1997) and López (1999).

The limitations of this elasto-plastic formulation, in order to represent the behaviour in loading and unloading cycles, will be discussed in Chapter 3.

2.4.2 Interface constitutive models based on frictional behaviour

There are several proposals for constitutive laws of Coulomb-type (cohesionless) frictional behaviour with dilatancy and degradation of the contact surface, used to simulate the behaviour of geological discontinuities or interface elements in rocks, generally implemented within a Finite Element code. Among the various models proposed, the works of Plesha (1987), Plesha, Ballarini, and Parulekar (1989), Dowding et al. (1991), Snyman, Bird, and Martin (1991), Snyman and Martin (1992) can be found, among others. Although these models are focused on the behaviour of fully formed cracks, their formulation and concepts are of great importance in dealing with the problem of crack surfaces contact and the dilatancy effect with regard to combined actions of normal and tangential displacements. Therefore, they are often used in combination with damage or plasticity models.

Plesha (1987) proposes a constitutive law for the behaviour of discontinuities, with dilatancy and degradation of the contact surface, applicable to friction problems. It is assumed that the slide does not occur exactly parallel to the midplane of the interface, but along an inclined angle characterising the asperity. The Coulomb criterion is proposed to be satisfied in the inclined plane, expressing it in terms of the components of the interface stress vector, so that it can reflect the main features of the sliding to one side or the other with respect to the initial position. The observed interface degradation under cyclic loading is explained by the decrease of the asperity angle as a function of the plastic work dissipated by the shear component. Later, in Plesha, Ballarini, and Parulekar (1989) the implementation of this friction law in two-dimensional finite elements is incorporated and some numerical results are presented.

In Dowding et al. (1991), an interface model is proposed with dilatancy, degradation of the asperities and settlement due to cyclic behaviour associated with earthquakes or explosions. It takes into account the non-associated plasticity in the slip between the asperities, a phenomenon that causes the dilatancy. The most important contribution is the addition of a continuity condition for the normal displacements during sliding at interfaces to consider the increase of the material volume in shear cycles when the asperities are degraded.

In Snyman, Bird, and Martin (1991), a first version of a friction model with dilatancy is presented that takes into account the different situations, both contact and non-contact, between the interface faces. However, this implies a limitation when there is a change in the direction of shear deformations; this has been corrected in the further version (Snyman and Martin 1992). A detailed description of this friction law is given in Section 3.2.2 of Chapter 3.

2.4.3 Interface constitutive models which combine damage and plasticity

Several authors have proposed interface constitutive laws that combine damage and plasticity behaviour in order to ensure that the global model reflects the most appropriate aspects of each.

Jefferson (2002) presents a cohesive-type interface model with three components: one for damage, one for bridging and one for the fully decoupled case. The value of these components, which represent a portion of a representative volume of material (REV), changes according to evolution functions that are developed from cyclic experimental test data. The undamaged component is handled as elastic damage, the bridging component is divided into two further components, which are elasto-plastic and elastic with contact and, finally, the completely decoupled component, which is handled as elasto-plastic with contact.

Alfano, Marfia, and Sacco (2006) propose a cohesive damage and friction model for interfaces capable of simulating crack propagation in different fracture modes. Crack closure and reopening are both considered. Friction and dilatancy are characterised by decreasing friction angles and dilatancy values, respectively, recovering the latter during cyclic loading. A numerical model is developed and implemented in a finite element code, and several simulations and comparisons with experimental data are performed. A weak aspect of this model is the formulation of the damage type, which uses uncoupled stress-displacement relationships in respect of Mode I and Mode II fracture modes.

A new cohesive model combining damage and friction is proposed in Alfano and Sacco (2006) for mesomechanical examples. A decomposition of a representative interface area into a damaged area and an undamaged area has been performed, assuming that friction effects only occur in the fully damaged area. The incremental increase of the friction effect is a consequence of the gradual increase of the damaged area at the interface: it goes from an initial intact state to a total loss of cohesion. For the damage part a Crisfield interface model is used and for the friction part a Coulomb model is used.

Chapter 3

Interface constitutive law

In this chapter, an interface constitutive model is developed in which an existing cohesive-frictional type of behaviour is incorporated with the effect of the degradation of the material strength parameters due to chemical processes.

In Section 3.1, the original interface constitutive law, proposed by Carol, P. C. Prat, and López (1997), is briefly described, formulated in the framework of elasto-plastic theory and also including fracture mechanics concepts and fracture energy parameters.

In order to solve some of the limitations of this elasto-plastic law in load-unload-reload situations, an interface constitutive model has recently been proposed within the MECMAT-UPC research group. This model consists of a parallel combination of two models: on the one hand, a cohesive behaviour based on the scalar damage theory, and on the other hand, a frictional behaviour with dilatancy. In Section 3.2, this constitutive model is presented, and the new features developed in this Masters Thesis to incorporate the effect of chemical degradation of the material strength parameters due to acid attack, are also described.

3.1 Elasto-plastic constitutive law

This section briefly describes the original interface constitutive law, which has been the starting point for subsequent versions and improvements, at first proposed in Carol and P. C. Prat (1990), and later modified in Carol, P. C. Prat, and López (1997), Carol and López (1998), López (1999), Carol, López, and Roa (2001), López, Carol, and Aguado (2008) and Caballero, K. Willam, and Carol (2008).

The model is based on the theory of elastoplasticity and incorporates concepts from fracture mechanics including fracture energy parameters. The behaviour is formulated in terms of the normal and tangential components of the stresses on the interface midplane surface $\boldsymbol{\sigma} = [\sigma_N, \sigma_T]^{\mathrm{t}}$ (t = transposed) and the corresponding relative displacements $\mathbf{r} = [r_N, r_T]^{\mathrm{t}}$. These displacements may be identified as the crack opening and sliding (Figure 3.1).

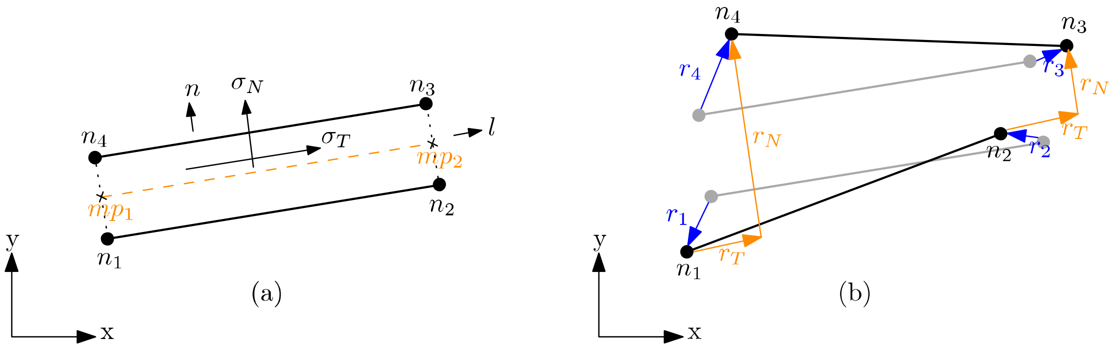

Figure 3.1: 2D representation of the stress components (a) and interface relative displacements (b); where n_i are the element nodes and mp_i are the nodal points in the element's midplane.

3.1.1 Cracking surface and work dissipated in the fracture process

The cracking process starts when the stress on the interface midplane surface reaches the condition $F = 0$, where F is the cracking function defined in the space of normal and shear stresses, which also depends on some strength parameters, grouped in the vector $\mathbf{\Phi}$. The adopted surface is a hyperbola dependent on three mechanical parameters:

$$F(\boldsymbol{\sigma}, \mathbf{\Phi}) = \sqrt{{\sigma_T}^2 + (c - \chi \tan \phi)^2} - (c - \sigma_N \tan \phi) \tag{3.1}$$

where σ_N is the normal stress, σ_T the tangential stress, χ is the distance from the origin to the apex of the hyperbola representing the tensile strength, and c and $\tan \phi$, the apparent cohesion and the coefficient of internal friction respectively, are the parameters characterising the asymptote (Figure 3.2(a)).

When cracking begins, the cracking surface F contracts and moves, so that the current stress state decreases (since it always has to remain on the surface). For a given initial fracture surface F_0 (Figure 3.2(c)), its evolution will depend on the fracture mode to which the interface element is subjected (Figure 3.2(b)). In the case of pure tensile (Mode I), a fully developed fracture is characterised by a single kinematic condition, i.e. separation in the normal direction of the two interface faces. Because of material heterogeneity, the separated faces in the fracture process are irregular and the final cracking surface is a hyperbola with apex at the origin (surface F_1 in Figure 3.2(c)).

The other limit situation corresponds to a cracking caused by a tangential stress with high compression and no dilatancy, called Asymptotic Mode II (or Mode IIa) in Carol, P. C. Prat, and López (1997). In this condition, slip occurs in the tangential direction, with no dilatancy in the normal direction (Figure 3.2(b)), and the final fracture surface is defined by a straight line representing purely frictional behaviour (surface F_2 in Figure 3.2(c)). In this case, the parameters χ and c have vanished, while the internal friction angle reaches its residual value $\tan \phi_r$.

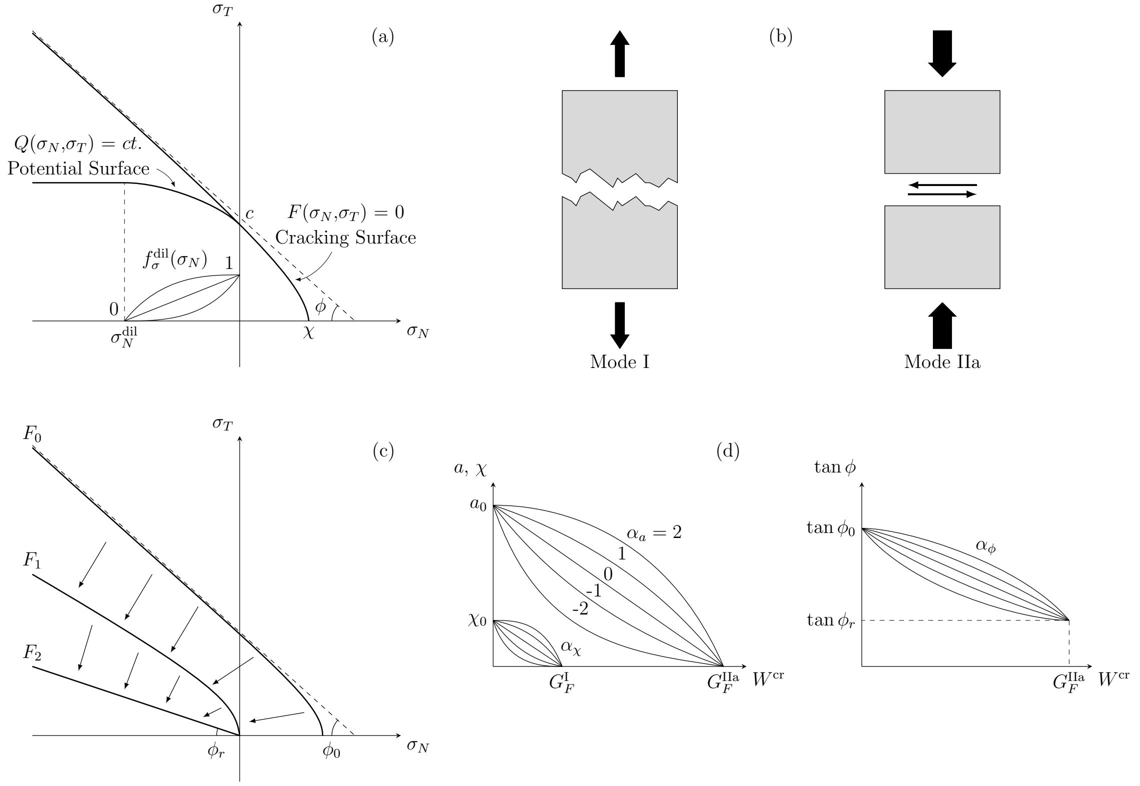

Figure 3.2: Interface model: (a) cracking surface F and plastic potential Q; (b) basic fracture modes; (c) evolution of cracking surface F; evolution of parameters χ, a and $\tan\phi$ (Carol, P. C. Prat, and López 1997; López, Carol, and Aguado 2008).

The parameters which control the fracture modes are the Mode I fracture energy, G_F^{I}, and the Mode IIa fracture energy, G_F^{IIa}.

During the fracture process, the surface F parameters, i.e. χ, c and $\tan\phi$, decrease in value (softening). The evolution of these parameters is controlled by an internal history variable, which is the work dissipated during the fracture process W^{cr}, defined incrementally as:

$$dW^{\mathrm{cr}} = \begin{cases} \sigma_N dr_N^{\mathrm{cr}} + \sigma_T dr_T^{\mathrm{cr}}, & \sigma_N \geq 0 \\ \sigma_T dr_T^{\mathrm{cr}} \left(1 - \left|\dfrac{\sigma_N \tan\phi}{\sigma_T}\right|\right), & \sigma_N < 0 \end{cases} \tag{3.2}$$

where dr_N^{cr} and dr_T^{cr} represent the increment of the relative displacements of the opening in the normal and tangential directions, respectively.

Equation (3.2) shows that in the tensile and shear zone, all the work dissipated in the interface comes from fracture processes, while in the compression and shear zone, the contribution comes from the work dissipated in the tangential direction from which the frictional work is subtracted (Carol and P. C. Prat 1990).

3.1.2 Dilatancy and flow rule

In heterogeneous materials, the crack planes are generally irregular due to the tendency to spread according to the weakest zones, for instance between the interfaces of the different material phases. In this context, slippage due to tangential solicitations is associated with the phenomenon of dilatancy, due to the sawtooth effect. To determine the direction of dilatancy, the stress space can be used in a similar way as in classical plasticity theory, where at each point the direction of plastic deformations (flow rule) is perpendicular to a function called plastic potential Q (Figure 3.2(a)). Dilatancy can be interpreted as the angle between the gradient of Q and the vertical axis of tangential stresses, such that a direction parallel to the vertical axis indicates no dilatancy, while a direction parallel to the axis of normal stresses represents the opening of a crack without tangential displacement, as in the case of pure tensile stress. The direction of the normal to the plastic potential surface can be defined as a function of the normal direction to the fracture surface using a transformation matrix $\mathbf{A}$. Using this convention, the flow rule for this model may be expressed as follows:

$$\mathbf{m} = \frac{\partial Q}{\partial \boldsymbol{\sigma}} = \mathbf{A}\mathbf{n} \tag{3.3}$$

$$\mathbf{n} = \frac{\partial F}{\partial \boldsymbol{\sigma}} = \begin{pmatrix} \frac{\partial F}{\partial \sigma_N} \\ \frac{\partial F}{\partial \sigma_T} \end{pmatrix} = \begin{pmatrix} \tan\phi \\ \frac{\sigma_T}{\sqrt{{\sigma_T}^2 + (c - \chi \tan\phi)^2}} \end{pmatrix} \tag{3.4}$$

$$\begin{aligned} \mathbf{A} &= \begin{pmatrix} 1 & 0 \\ 0 & 1 \end{pmatrix}, \quad \sigma_N \geq 0 \\ \mathbf{A} &= \begin{pmatrix} f_\sigma^{\mathrm{dil}} f_c^{\mathrm{dil}} & 0 \\ 0 & 1 \end{pmatrix}, \quad \sigma_N < 0 \end{aligned} \tag{3.5}$$

If $\mathbf{A}$ corresponds to the identity matrix, then the flow rule is associated. In the model, an associated formulation, $Q = F$, is adopted in tension but not in compression (Figure 3.2(a)).

Experimental results on quasi-brittle materials (Amadei et al. 1989) show that the higher the value of the compressive stress, the smaller the dilatancy effect. Furthermore, the dilatancy variation decreases with the increase of the interface degradation state, so that, for a shear test with constant compression, the dilatancy angle decreases with the increase of the relative normal and tangential displacement (Pande, Beer, and Williams 1990).

Dilatancy effects are taken into account by a reduction of the normal component of the matrix $\mathbf{A}$ using the factors f_σ^{dil} and f_c^{dil}. The dilatancy reduction caused by the increase of the compressive stresses cancels out when a predefined compression value, σ^{dil}, is reached. The function f_σ^{dil} decreases as shown in Figure 3.2(a), and is defined as:

$$f_\sigma^{\text{dil}} = 1 - S\left(\frac{|\sigma_N|}{\sigma^{\text{dil}}}, \alpha_{\sigma_{\text{dil}}}\right) \tag{3.6}$$

Dilatancy reduction also occurs as the fracture surface degrades, until it becomes zero when it reaches the state of pure friction (surface F_2 in Figure 3.2(c)):

$$f_c^{\text{dil}} = 1 - S\left(\xi_a, \alpha_a\right) \tag{3.7}$$

In Equations (3.6) and (3.7), S is given by the expression:

$$S(\xi, \alpha) = \frac{\xi e^{-\alpha}}{1 + \left(e^{-\alpha} - 1\right)\xi} \tag{3.8}$$

The increase in relative plastic displacements is expressed as:

$$d\mathbf{r}^{\text{cr}} = d\lambda \frac{\partial Q}{\partial \boldsymbol{\sigma}} \tag{3.9}$$

This vector is characterised by the direction of the plastic relative displacements, given by the partial derivatives of the potential function Q, while the magnitude is determined by $d\lambda$, which is a non-negative scalar called the plastic multiplier.

3.1.3 Cracking surface evolution

The evolution of the cracking surface F is produced by the decrease of the parameters of the hyperbola (Equation (3.1)): the tensile strength χ, the apparent cohesion c and the angle of internal friction $\tan\phi$, vary as a function of the increase of the dissipated work W^{cr} during crack formation (Equation (3.2)). To define the evolution of the parameters, a scaling function $S(\xi, \alpha)$ (Equation (3.8)) is used to obtain a family of curves with different evolution depending on the chosen value of the shape parameter α (Carol and P. C. Prat 1990; Carol, P. C. Prat, and López 1997).

3.1.3.1 Tensile strength

The tensile strength χ decreases from the initial value χ_0 until it becomes zero when $W^{\text{cr}} = G_F^{\text{I}}$. The scaling function $S(\xi_\chi, \alpha_\chi)$ is applied, considering $\xi_\chi = W^{\text{cr}}/G_F^{\text{I}}$ and $\alpha = \alpha_\chi$ (Figure 3.2(d)). The evolution of χ is given by:

$$\chi = \begin{cases} \chi_0 \left[1 - S\left(\xi_\chi, \alpha_\chi\right)\right], & W^{\text{cr}} < G_F^{\text{I}} \\ 0, & W^{\text{cr}} \geq G_F^{\text{I}} \end{cases} \tag{3.10}$$

3.1.3.2 Cohesion

To obtain a proper evolution of the cohesion c, it is convenient to define this parameter indirectly through χ, $\tan\phi$ and the parameter a (Figure (3.3)), which represents the distance between the apex of the hyperbola and its asymptotes. The relationship is given by the expression:

$$c = (\chi + a)\tan\phi \tag{3.11}$$

For the evolution of a, a decrease from the initial value a_0 (obtained with Equation (3.11) and using the initial parameters χ_0, c_0 and $\tan\phi_0$) to the value zero when $W^{\mathrm{cr}} = G_F^{\mathrm{IIa}}$ is adopted. The scaling function $S(\xi_a, \alpha_a)$ is applied, considering $\xi_a = W^{\mathrm{cr}}/G_F^{\mathrm{IIa}}$ and $\alpha = \alpha_a$ (Figure 3.2(d)). The evolution of c can be expressed as:

$$c = \begin{cases} c_0 \left[\frac{\chi_0}{c_0}\tan\phi\left[S\left(\xi_a,\alpha_a\right) - S\left(\xi_\chi,\alpha_\chi\right)\right] + \frac{\tan\phi}{\tan\phi_0}\left[1 - S\left(\xi_a,\alpha_a\right)\right]\right], & W^{\mathrm{cr}} < G_F^{\mathrm{IIa}} \\ 0, & W^{\mathrm{cr}} \geq G_F^{\mathrm{IIa}} \end{cases} \tag{3.12}$$

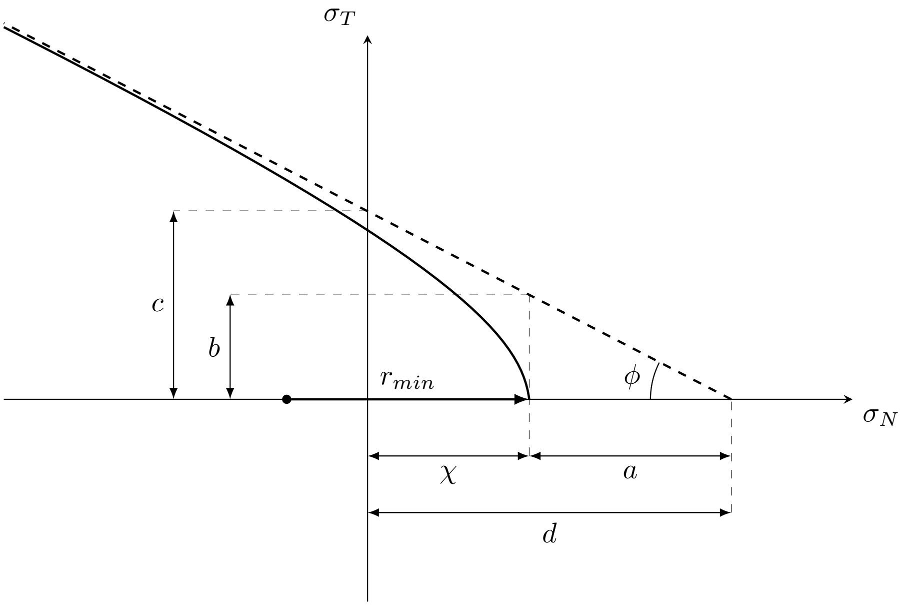

Figure 3.3: Cracking surface F parameters.

3.1.3.3 Internal friction coefficient angle

The evolution of the internal coefficient friction angle $\tan\phi$ is given by:

$$\tan\phi = \begin{cases} \tan\phi_0 - \left[\tan\phi_0 - \tan\phi_r\right] S\left(\xi_\phi,\alpha_\phi\right], & W^{cr} < G_F^{\mathrm{IIa}} \\ \tan\phi_r, & W^{cr} \geq G_F^{\mathrm{IIa}} \end{cases} \tag{3.13}$$

where ϕ_0 is the initial friction angle and ϕ_r is the residual friction angle. Therefore, $\tan\phi$ varies from its initial value to a residual value when the final cracking surface is reached (Figure 3.2). In this case, the coefficients of $S(\xi_\phi, \alpha_\phi)$ in Equation (3.13) are given by $\xi_\phi = W^{\mathrm{cr}}/G_F^{\mathrm{IIa}}$ and $\alpha = \alpha_\phi$.

3.1.4 Constitutive verification and examples

In order to illustrate the behaviour of the elastoplastic interface law, two examples are presented. The first is a numerical simulation of pure tensile loading. An increasing positive value of the relative normal displacement is prescribed exclusively. The parameters used are: stiffness $K_N = 1000$ MPa/mm, tensile strength $\chi_0 = 3$ MPa, shape coefficients $\alpha_\chi = 0$, fracture energy G_F^{I} equal to 0.01, 0.02, 0.03, 0.05 and 0.1 N/mm (all other parameters are irrelevant in this example). The results are presented in Figure 3.4, showing perfect agreement with the exact exponential solution (Carol, P. C. Prat, and López 1997) and the expected influence of the fracture energy G_F^{I} (the area enclosed under each complete curve is equal to the prescribed value of G_F^{I}).

The second example is a shear case with constant compression. In a first loading step, a certain amount of compressive stress is applied. Subsequently, the relative shear displacement is progressively increased while keeping the compression constant. The test is repeated for different values of compressive stress. The parameters used are: $K_N = K_T = 25000$ MPa/mm, $\tan\phi = 0.8785$, $\chi_0 = 3$ MPa, $c_0 = 4.5$ MPa, $G_F^{\mathrm{I}} = 0.03$ N/mm, $G_F^{\mathrm{IIa}} = 0.06$ N/mm, $\sigma_N^{\mathrm{dil}} = 30$ MPa, $\alpha_\sigma^{\mathrm{dil}} = 2$, and $\alpha_\chi = \alpha_c = \alpha_c^{\mathrm{dil}} = 0$. The results are presented in Figure 3.5 in terms of the shear stresses versus relative shear displacements for compressive normal stress values of 0.1, 2, 6 and 10 MPa. The family of curves shows the influence of increasing compression on the shear capacity of the interface. After the peak, all the descending curves show a first steeper part given by the decrease of both softening parameters χ and c, followed by a slower decreasing part where W^{cr} overcomes G_F^{I}, χ disappears and only c decreases. Finally, all curves tend to a residual value of the shear stress which is given directly by the friction angle and the applied normal stress as $\sigma_N \tan\phi$.

3.1.5 Limitations of the elastoplastic law

The elastoplastic law for interface elements has been widely used in several studies of concrete structures and meso-structures and other quasi-brittle materials (Carol, López, and Roa 2001, López, Carol, and Aguado 2008, Caballero, López, and Carol 2006, Caballero, Carol, and López 2007, Idiart, López, and Carol 2011). However, it has limitations in representing interface behaviour involving loading-unloading-reloading cycles. On the one hand, in pure tensile or tensile-shear loading states, cracks close completely or partially with unloading, an aspect that cannot be captured by an elastoplastic law in which unloading occurs according to the direction of the initial stiffness (Figure 3.6). Furthermore, in shear loading situations with constant compression, it has clear limitations in terms of

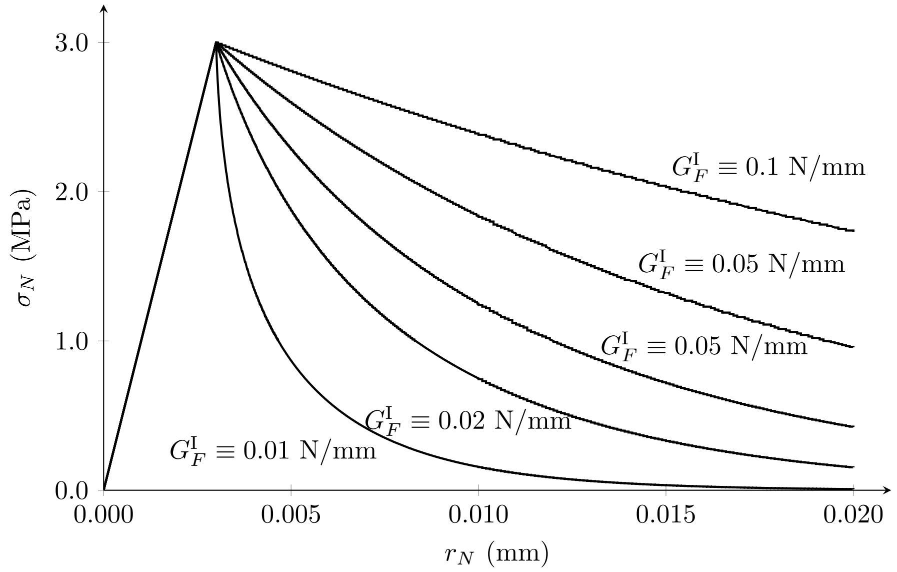

Figure 3.4: Pure tensile example with the elastoplastic law: normal stress as a function of relative normal displacement for different values of fracture energy.

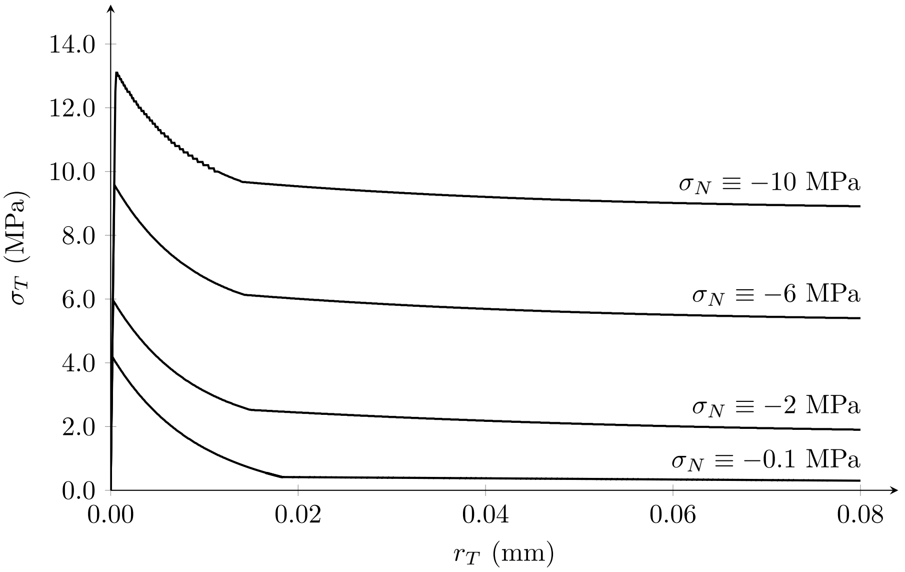

Figure 3.5: Example of shear with constant compression with the elastoplastic law: shear stress as a function of relative shear displacement for different values of normal stress.

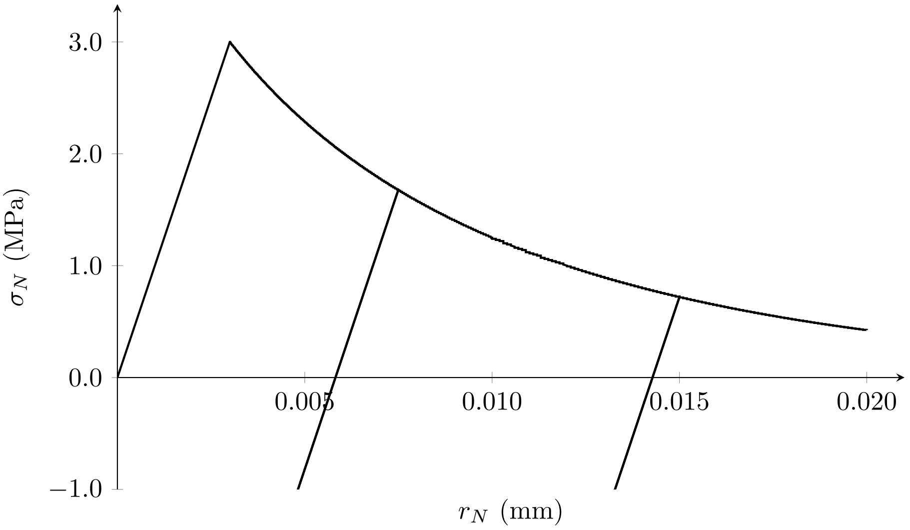

Figure 3.6: Pure tensile case: normal stress as a function of relative normal displacement for two load-unload-reload cycles.

the dilatancy phenomenon as it keeps increasing when the direction of tangential displacement is reversed, which is unrealistic, as there should be a recovery of dilatancy when moving back in the path of the asperities. These aspects have been overcome in Puiggrós (2017) and López, Puiggrós, and Carol (2024), which are discussed in detail in Section 3.2.

On the other hand, the original elastoplastic law did not consider a reduction in strength due to chemical degradation by acid attack such as CO_2. These aspects were investigated in Martínez (2020) and Martínez et al. (2022).

3.2 New cohesive-frictional damage model with chemical degradation

In this new interface constitutive model, a cohesive behaviour based on scalar damage theory is combined with a frictional behaviour with dilatancy, to which the effect of degradation of the material strength parameters due to chemical processes is incorporated. A non-linear relationship between the stresses and the corresponding relative interface displacements is formulated in order to reproduce the non-linear mechanical behaviour of the interface from micro-cracking to complete crack formation.

For this purpose, a representative area A of the Fracture Process Zone (FPZ, Section 2.3.2) of the interface is considered, which can be divided into an undamaged zone A_u and a damaged zone A_f, as shown in Figure 3.7. In the undamaged part, the interface is completely intact, while in the damaged part the contact is only frictional. Considering a

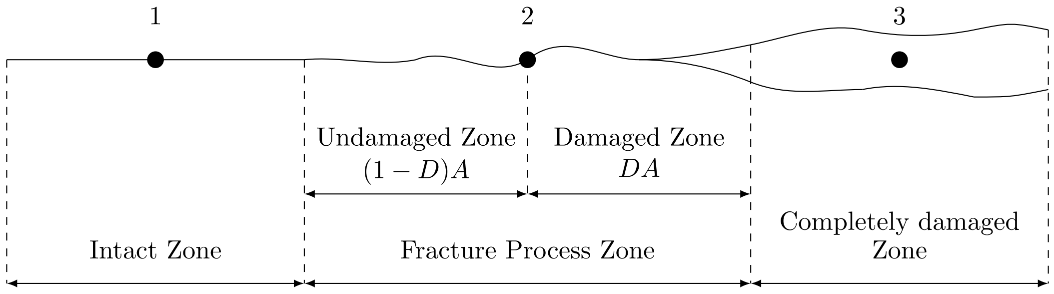

Figure 3.7: Representative interface area.

damage coefficient D, expressed by the ratio A_f/A, it is possible to write:

$$A = A_u + A_f \tag{3.14}$$

where

$$A_u = (1-D)A \tag{3.15}$$

and

$$A_f = DA \tag{3.16}$$

Figure 3.7 shows the three possible scenarios that can occur:

- point 1: completely intact, non-degraded area, where $A_u = A$, $A_f = 0$ and $D = 0$;
- point 2: fracture process zone in which there is an undamaged zone and a damaged zone and $0 < D < 1$;
- point 3: area where the crack is fully formed, with $A_u = 0$, $A_f = A$ and $D = 1$.

The interface constitutive law is defined in a homogenisation context in terms of nominal or average relative stresses and displacements. First, the relative displacements are considered constant in the representative interface area. Therefore:

$$\mathbf{r}^{\mathrm{u}} = \mathbf{r}^{\mathrm{f}} = \mathbf{r} = [r_N, r_T]^{\mathrm{t}} \tag{3.17}$$

where $\mathbf{r}^{\mathrm{u}}$ and $\mathbf{r}^{\mathrm{f}}$ are the relative displacement vectors in the undamaged and damaged parts, respectively, and r_N and r_T are the normal and tangential components of the relative displacement vector, respectively.

Second, the nominal stress vector over the representative interface area is obtained from the weighted contribution of the undamaged and damaged area stresses:

$$\boldsymbol{\sigma} = (1-D)\boldsymbol{\sigma}^{\mathrm{u}} + D\boldsymbol{\sigma}^{\mathrm{f}} \tag{3.18}$$

with

$$\boldsymbol{\sigma} = [\sigma_N, \sigma_T]^{\mathrm{t}} \tag{3.19}$$

where $\boldsymbol{\sigma}^{\mathrm{u}}$ is the stress vector in the undamaged zone; $\boldsymbol{\sigma}^{\mathrm{D}} = (1 - D)\boldsymbol{\sigma}^{\mathrm{u}}$ is the stress vector determined from the damage-plasticity model (Section 3.2.1), where the evolution of D is also defined; $\boldsymbol{\sigma}^{\mathrm{f}}$ are the stresses obtained from the friction model with dilatancy (Section 3.2.2).

3.2.1 Scalar damage-plastic model

As discussed in Chapter 2, models based on elastoplastic (Figure 3.8(a)) and elastic damage theory (Figure 3.8(b)) represent two extremes of material idealisation that are simplifications of typical experimentally observed behaviour. The observed behaviour of quasi-brittle materials has an intermediate characteristic where both effects take place: stiffness degradation and remanent (plastic) deformations (Figure 3.8(c)).

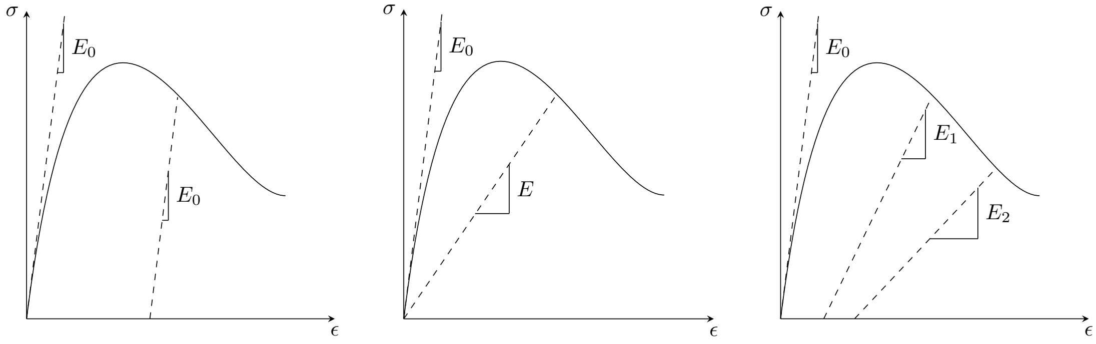

(a) Plastic behaviour (b) Damage behaviour (c) Real coupled behaviour

Figure 3.8: Typical $\sigma - \epsilon$ curves: (a) elastoplasticity, (b) damage, (c) combination of plasticity and damage.

A model of the type shown in Figure 3.8(c) is adopted that combines both effects, with isotropic damage in which the degradation of the stiffness matrix depends on the evolution of a single scalar-type variable, so that all the components of the stiffness tensor are reduced by the same coefficient $(1 - D)$. To facilitate the writing of the various formulae in this section, the stresses in the scalar damage model, which are referred to as $\boldsymbol{\sigma}^{\mathrm{D}}$ in the previous section, here are referred simply as $\boldsymbol{\sigma}$.

In Figure 3.9, the relative damage stress-displacement diagram is presented, in its total components, whose characteristic equations can be expressed by the following relationships:

$$\boldsymbol{\sigma} = (1 - D)\boldsymbol{\sigma}^{\mathrm{u}} = (1 - D)\mathbf{K}^0 : (\mathbf{r} - \mathbf{r}^{\mathrm{dp}}) = \mathbf{K} : (\mathbf{r} - \mathbf{r}^{\mathrm{dp}}) \tag{3.20}$$

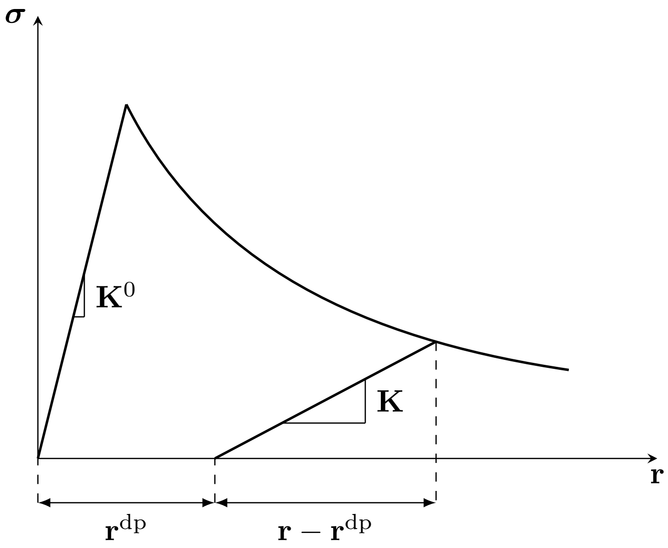

Figure 3.9: Diagram of damage stresses-relative displacements in total components.

where $\mathbf{r}^{\mathrm{dp}}$ is the plastic relative displacements (non-recoverable) and $\mathbf{K}$ is the degraded stiffness matrix whose expression is given by:

$$\mathbf{K} = (1-D)\mathbf{K}^0 \qquad ; \qquad \mathbf{K}^0 = \mathrm{diag}\,[K_N, K_T] \tag{3.21}$$

where D is the damage variable varying from zero to one and the elastic stiffness matrix $\mathbf{K}^0$ is assumed to be a diagonal matrix consisting of the constant coefficients K_N and K_T in the normal and tangential directions, respectively.

Following the work of Carol, Rizzi, and Willam (1994) and Carol, Rizzi, and K. Willam (2001), a logarithmic damage variable L is introduced, defined as:

$$L = \ln\frac{1}{1-D} \qquad ; \qquad D = 1-e^{-L} \tag{3.22}$$

where it can be seen that L varies between 0 and ∞ and allows to rewrite Equation (3.21) as:

$$\mathbf{K} = e^{-L}\mathbf{K}^0 \tag{3.23}$$

On the other hand, in Figure 3.10 the damage stresses-relative displacements plot is shown in its differential form.

The increase of the relative displacement vector can be expressed as:

$$d\mathbf{r} = d\mathbf{r}^{\mathrm{e}} + d\mathbf{r}^{\mathrm{dd}} + d\mathbf{r}^{\mathrm{dp}}, \qquad \text{with} \quad d\mathbf{r}^{\mathrm{di}} = d\mathbf{r}^{\mathrm{dd}} + d\mathbf{r}^{\mathrm{dp}} \tag{3.24}$$

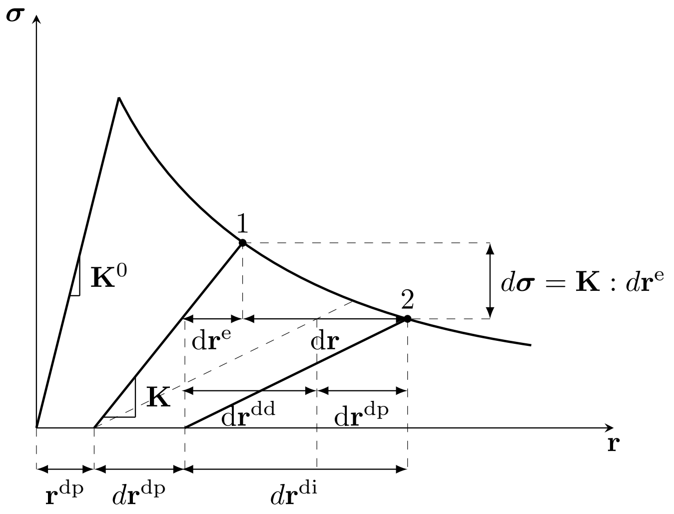

Figure 3.10: Diagram of damage stresses-relative displacements in differential components.

where $d\mathbf{r}^{\mathrm{e}}$ is the elastic component and $d\mathbf{r}^{\mathrm{dd}}$ and $d\mathbf{r}^{\mathrm{dp}}$ are the damage and plasticity components, respectively. The flow rule of the latter terms can be expressed as:

$$d\mathbf{r}^{\mathrm{dd}} = \mathbf{m}^{\mathrm{d}} d\lambda \qquad ; \qquad d\mathbf{r}^{\mathrm{dp}} = \mathbf{m}^{\mathrm{p}} d\lambda \tag{3.25}$$

$$d\mathbf{r}^{\mathrm{di}} = d\mathbf{r}^{\mathrm{dd}} + d\mathbf{r}^{\mathrm{dp}} = \mathbf{m}^{\mathrm{dp}} d\lambda, \qquad \text{with} \quad \mathbf{m}^{\mathrm{dp}} = \mathbf{m}^{\mathrm{d}} + \mathbf{m}^{\mathrm{p}} \tag{3.26}$$

where $\mathbf{m}^{\mathrm{dp}}$ defines the direction and $d\lambda$ is the inelastic/plastic multiplier, which determines the magnitude.

As can be appreciated in Figure 3.10 the stress increment is given by:

$$d\boldsymbol{\sigma} = \mathbf{K} : d\mathbf{r}^{\mathrm{e}} = \mathbf{K} : (d\mathbf{r} - d\mathbf{r}^{\mathrm{dd}} - d\mathbf{r}^{\mathrm{dp}}) = \mathbf{K} : (d\mathbf{r} - d\mathbf{r}^{\mathrm{dp}}) - \mathbf{K} : d\mathbf{r}^{\mathrm{dd}} \tag{3.27}$$

Differentiating Equation (3.20) one obtains:

$$d\boldsymbol{\sigma} = \mathbf{K} : (d\mathbf{r} - d\mathbf{r}^{\mathrm{dp}}) + d\mathbf{K} : (\mathbf{r} - \mathbf{r}^{\mathrm{dp}}) \tag{3.28}$$

Comparing Equations (3.27) and (3.28) and operating one finally obtains (Carol, Rizzi, and Willam 1994):

$$d\mathbf{r}^{\mathrm{dd}} = dL(\mathbf{r} - \mathbf{r}^{\mathrm{dp}}) \tag{3.29}$$

Comparing Equation (3.29) and the corresponding one in (3.25) it can be seen that:

$$d\lambda = dL = \frac{dD}{1-D} \qquad ; \qquad \mathbf{m}^{\mathrm{d}} = \mathbf{r} - \mathbf{r}^{\mathrm{dp}} \tag{3.30}$$

so that the increment of the logarithmic damage variable dL can be identified with the multiplier $d\lambda$, and the direction of the relative damage displacements (term $\mathbf{m}^{\mathrm{d}}$) is determined in this theory by the updated values of the relative displacements minus the plastic ones. This is in accordance with Carol, Rizzi, and Willam (1994) and Carol, Rizzi, and K. Willam (2001) that, for an isotropic scalar damage model of the $(1-D)$ type, the flow rule for the damage deformations must be equal to the total deformation variable.

3.2.1.1 History variables

The model has two history variables, one internal reflecting deterioration due to the fracture process and the other external reflecting degradation due to chemical processes. The external history variable (η) is assumed to be a result of the simulation of chemical-transport processes leading to the degradation of the material and is therefore, for the interface constitutive law, considered as a given value. Furthermore, it is considered to be a dimensionless variable, ranging from $\eta = 0$, for a non-degraded material, to $\eta = 1$, for a fully degraded material. Moreover, the degradation process is assumed to be irreversible ($d\eta \geq 0$), so no healing processes are considered. Depending on the problem under consideration, the variable η can be defined as a function of different history variables of the chemical-transport simulation, such as the concentration of solid phases or the porosity of the material.

On the other hand, for the internal history variable that reflects the deterioration due to the fracture process, the logarithmic damage variable L is considered directly, whose value is obtained by summing (integrating) all the $dL = d\lambda$, so that:

$$L = \int d\lambda \tag{3.31}$$

This form has been found to be more convenient than the history variable considered in the original law proposed in Carol, P. C. Prat, and López (1997), which was the work dissipated in fracture processes during the formation of a crack (W^{cr}), which in the current model is derived as post-process from dL, so that:

$$W^{\mathrm{cr}} = \int \frac{\partial W^{\mathrm{cr}}}{\partial \lambda} d\lambda \tag{3.32}$$

3.2.1.2 Cracking surface and evolution laws

Cracking begins when the stress on the interface plane reaches the condition $F(\boldsymbol{\sigma}, \mathbf{p}) = 0$, where F is the adopted cracking surface defined in the space of normal and shear stresses, and vector $\mathbf{p}$ collects the current values of the cracking surface parameters. The cracking surface adopted in this paper (Figure 3.11(a)) is the same three-parameter hyperbolic surface proposed by Carol and P. C. Prat (1990), expressed more conveniently for the

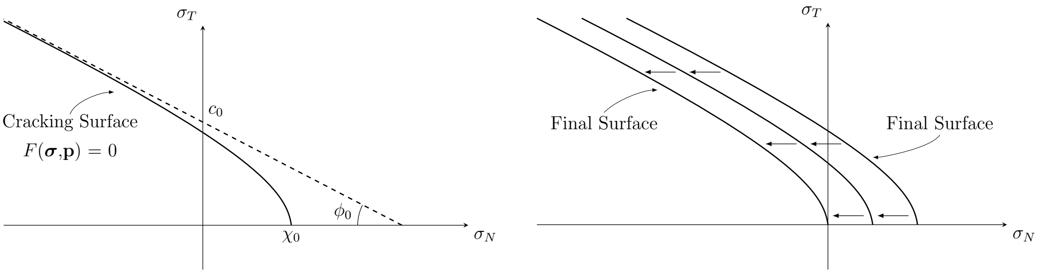

(a) (b)

Figure 3.11: Failure surface: (a) hyperbolic cracking surface F for $L = 0$ and (b) evolution of cracking surface.

purposes of numerical implementation as in Caballero, K. Willam, and Carol (2008) as follows:

$$F(\boldsymbol{\sigma},\mathbf{p}) = \sqrt{{\sigma_T}^2 + (c - \chi\tan\phi)^2} - (c - \sigma_N \tan\phi) \tag{3.33}$$

It is assumed that the surface may shrink representing softening behaviour, as it is discussed in the following, where $\mathbf{p} = [\chi,\ c,\ \tan\phi]^{\mathrm{t}}$, and χ is the abscissa of the hyperbola representing the tensile strength, c is the apparent cohesion and $\tan\phi$ is the coefficient of internal friction. The last two parameters define the asymptote of the hyperbola, as shown in Figure 3.11(a).

The evolution of the cracking surface $F = 0$ is controlled by the evolution of the parameter χ, as a function of the internal history variable L and the external history variable η; the evolution of c is defined in such a way that it results in a translation of the hyperbola to the origin (kinematic softening), while parameter $\tan\phi$ remains constant throughout the degradation process.

The tensile strength parameter χ is reduced from its initial value χ_0 until it is zero by the following softening law:

$$\chi = \chi_0[1 - \xi(L)][1 - \eta] \tag{3.34}$$

where

$$\xi(L) = \frac{1}{\chi_0}\int \frac{\partial \chi}{\partial L} dL \tag{3.35}$$

and

$$\eta = 1 - \exp\left(-\frac{c_{mp}}{\bar{c}}\right) \tag{3.36}$$

where η varies in an exponential way, as for example adopted in Martínez (2020), where η was assumed to be a function of the concentration of carbon dioxide in pore solution c_{mp}, and $\bar{c}$ is a characteristic concentration value.

In this work, the parameter $c_{mp}/\bar{c}$ is arbitrarily adopted as an input value, as will be shown in the examples in Chapter 4.

On the other hand, $\frac{\partial \chi}{\partial L} = \frac{\partial \chi}{\partial \lambda}$ can be expressed as follows (developed in detail in a journal article currently under preparation):

$$\frac{\partial \chi}{\partial \lambda} = \frac{-\chi_0(1+2B)e^{\lambda} n \frac{r_0}{G_F}}{\left(\frac{\chi}{\chi_0}\right)^{\frac{1}{n}-3} + \frac{2r_0}{G_F} n \left(Be^{\lambda} + B'\right) \left(\frac{\chi}{\chi_0}\right)^{-1}} \tag{3.37}$$

where G_F is the model parameter representing the Mode I fracture energy, r_0 is the elastic energy, the coefficient n is a non-negative scalar that determines the shape of the tensile softening expression, the coefficients B and B' are related to β and β' as follows:

$$B = \frac{\beta}{1-\beta} \quad ; \quad B' = -\frac{\beta'}{1-\beta} \quad ; \quad \beta' = \beta + \gamma - \beta\gamma \tag{3.38}$$

being β a coefficient that varies between zero (pure damage case with unloading at the origin) and one (elastoplastic case with elastic unloading) and γ is a positive scalar parameter defining the proportion of plastic relative displacement at the end of the softening curve (ratio between the values of the maximum plastic relative displacement and the elastic relative displacement at the peak).

It can be expected that chemical degradation will reduce the fracture energy of the material. To introduce this effect, G_F it is assumed to vary as a function of chemical degradation according to the following expression:

$$G_F = G_{F_0}^{\mathrm{I}}(1-\eta) + G_{F_{min}}^{\mathrm{I}}\eta \tag{3.39}$$

where $G_{F_0}^{\mathrm{I}}$ and $G_{F_{min}}^{\mathrm{I}}$ are the values of G_F^{I} for $\eta = 0$ (non-degraded material) and $\eta = 1$ (fully degraded material), respectively, which are input parameters of the model. The evolution of the apparent cohesion c occurs in such a way that it results in a shift of the hyperbola to the origin (kinematic softening) whose expression is given by (López 1999):

$$c = c_0 - \tan\phi\,(\chi_0 - \chi) \tag{3.40}$$

from which $\frac{\partial c}{\partial L} = \frac{\partial c}{\partial \lambda}$ can be expressed as:

$$\frac{\partial c}{\partial \lambda} = \tan\phi \frac{\partial \chi}{\partial \lambda} \tag{3.41}$$

Therefore, from the initial hyperbola, the surface is shifted as a function of decreasing χ until the final state of the hyperbola with apex at the origin (as shown in Figure 3.11(b)) is reached when the tensile strength is exhausted and the damage variable $D = 1$.

3.2.1.3 Flow rule

Equations (3.25) and (3.26) express the flow rule of the damage and plasticity components of the relative displacement increments, where $\mathbf{m}^{\mathrm{d}}$ and $\mathbf{m}^{\mathrm{p}}$ defines the direction and $d\lambda$ is the inelastic/plastic multiplier.

As determined in Equation (3.30) the direction of the relative damage displacements ($\mathbf{m}^{\mathrm{d}}$ term) is given in the scalar damage theory by the updated values of the total relative displacements minus the plastic ones, which can also be expressed in the following form, more suitable for the constitutive integration procedure:

$$\mathbf{m}^{\mathrm{d}} = \left(\mathbf{r} - \mathbf{r}^{\mathrm{dp}}\right) = \mathbf{K}^{\mathbf{-1}}\boldsymbol{\sigma} = (\mathbf{K}^{\mathbf{0}})^{-1}\boldsymbol{\sigma} e^{\lambda} \tag{3.42}$$

In the above-mentioned paper in preparation, the expression for m_N^{p} has been obtained for load cases with $\sigma_N \geq 0$. As for m_T^{p}, in the absence of information, a null value is adopted (it should be noted that in cases with compression, the dilatancy of the interface model is mainly provided by the friction model as described in Section 3.2.2).

In heterogeneous materials such as concrete or rock, the coupling between normal and shear stresses is accompanied by a separation between the crack faces, a phenomenon known as dilatancy. As discussed above in the description of the elastoplastic law, experimental results show that the dilatancy that occurs under null or low compression states, decreases with the level of compression and finally disappears at very high levels of compression (Atkinson et al. 1989). To account this effect, a function is introduced that reduces the dilatancy incidence of the model with increasing compressive stress, until it cancels out when a value σ^{dil}, which is an input parameter, is reached. The expression of this dimensionless factor f^{dil}, which varies between 1 and 0, is as follows:

$$f^{\mathrm{dil}} = \begin{cases} 1, & \sigma_N \geq 0 \\ 1 - \dfrac{|\sigma_N|}{\sigma^{\mathrm{dil}}}, & \sigma_N < 0 \end{cases} \tag{3.43}$$

In this way, the expression of $\mathbf{m}^{\mathrm{dp}}$ is the following:

$$\mathbf{m}^{\mathrm{dp}} = \begin{bmatrix} \frac{\sigma_N}{K_N^0} e^{\lambda} + \left[B\left(1 + \frac{1}{\chi}\frac{\partial \chi}{\partial \lambda}\right) m_N^d + \frac{B'}{K_N^0}\frac{\partial \chi}{\partial \lambda} \right] f^{\mathrm{dil}} \\ \frac{\sigma_T}{K_T^0} e^{\lambda} \end{bmatrix} \tag{3.44}$$

for which $\frac{\partial \chi}{\partial \lambda}$ corresponds to Equation (3.37).

3.2.2 Frictional behaviour model with dilatancy

As mentioned in Section 2.4.2 of Chapter 2, there are several proposals in the literature for constitutive laws with Coulomb-type frictional behaviour (without cohesion) with dilatancy and deterioration of the contact surface: these laws are mainly used to simulate the behaviour of discontinuities or interfaces between rocks and are generally implemented within a finite element code. The work of Plesha (1987), Plesha, Ballarini, and Parulekar (1989), Dowding et al. (1991), Snyman, Bird, and Martin (1991) and Snyman and Martin (1992) may be mentioned, among others.

In this thesis work, the frictional constitutive law adopted is a formulation based on the model proposed by Snyman and Martin (1992). In Snyman, Bird, and Martin (1991) a first version of a frictional model with dilatancy is presented which, however, differs from the physical behaviour when there is a reversal in the direction of the shear deformations. This aspect is corrected in the later version (Snyman and Martin 1992). In the following, the general formulation of the law is described considering that there is no deterioration of the asperities: in this case, consequently, the dilatancy remains constant.

The behaviour is formulated as a function of the normal and tangential component of the stresses in the plane of the interface $\boldsymbol{\sigma}^{\mathrm{f}} = [\sigma_N^{\mathrm{f}}, \sigma_T^{\mathrm{f}}]^{\mathrm{t}}$ (the superscript f is used to denote the friction model as in Equation (3.18)), and the corresponding relative displacements $\mathbf{r} = [r_N, r_T]^{\mathrm{t}}$. Figure 3.12 illustrates the normal and tangential components of the stresses and corresponding displacements at the top face of the interface.

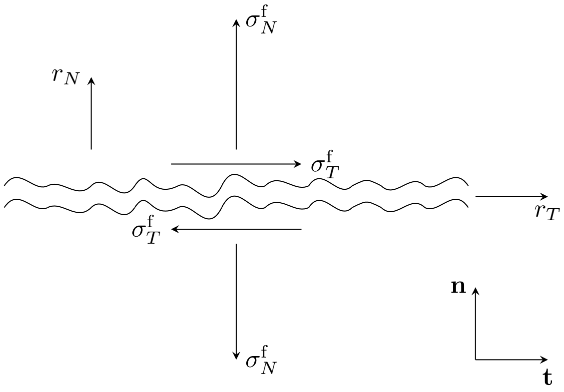

Figure 3.12: Representation of the interface: normal and tangential stress components and their corresponding relative displacements.

The total relative displacements are expressed as the sum of a reversible (elastic) component and an irreversible (plastic) component, denoted by the superscripts e and p, respectively, so that it can be expressed:

$$\begin{aligned} r_N &= r_N^{\mathrm{e}} + r_N^{\mathrm{p}} \\ r_T &= r_T^{\mathrm{e}} + r_T^{\mathrm{p}} \end{aligned} \tag{3.45}$$

The stresses are related to the elastic relative displacements by the expression:

$$\begin{bmatrix} \sigma_N^{\mathrm{f}} \\ \sigma_T^{\mathrm{f}} \end{bmatrix} = \begin{bmatrix} K_N & 0 \\ 0 & K_T \end{bmatrix} \begin{bmatrix} r_N^{\mathrm{e}} \\ r_T^{\mathrm{e}} \end{bmatrix} \tag{3.46}$$

where the elastic stiffness matrix is assumed to be a diagonal matrix formed by the constant coefficients K_N and K_T in the normal and tangential directions, respectively.

To implement an interface element law within the Finite Element Method, incremental integration algorithms of the Newton-Raphson type are used to solve incremental non-linear equations. The most commonly used procedure for the integration of constitutive laws is based on a step-by-step incremental approach using initially an elastic predictor, followed by a plastic corrector. Assuming that, at a given initial time t_n, the stress state, the relative displacements and the state variables are known, and having prescribed the relative displacement increments in a time increment of $\Delta t = t_{n+1} - t_n$, the purpose is to be able to determine at the end of the time increment Δt the final state of the stresses and internal variables. This means:

$$\begin{aligned} r_{N,n+1}^{\mathrm{e}} &= r_{N,n}^{\mathrm{e}} + \Delta r_{N,n+1}^{\mathrm{e}} = r_{N,n}^{\mathrm{e}} + \left(\Delta r_{N,n+1} - \Delta r_{N,n+1}^{\mathrm{p}}\right) \\ r_{T,n+1}^{\mathrm{e}} &= r_{T,n}^{\mathrm{e}} + \Delta r_{T,n+1}^{\mathrm{e}} = r_{T,n}^{\mathrm{e}} + \left(\Delta r_{T,n+1} - \Delta r_{T,n+1}^{\mathrm{p}}\right) \end{aligned} \tag{3.47}$$

and thus

$$\begin{bmatrix} \sigma_N^{\mathrm{f}} \\ \sigma_T^{\mathrm{f}} \end{bmatrix} = \begin{bmatrix} K_N & 0 \\ 0 & K_T \end{bmatrix} \begin{bmatrix} r_{N,n+1}^{\mathrm{e}} \\ r_{T,n+1}^{\mathrm{e}} \end{bmatrix} \tag{3.48}$$

Therefore, the main problem is to determine the plastic increment components of the total relative displacements.

Figure 3.13 shows a horizontal interface where the irregularities of the contact surfaces were idealised as sawtooth-shaped asperities oriented with an angle μ with respect to the plane of the interface, from the point of the initial state, i.e. no acting stresses. Figure 3.14 shows the contact surfaces after some inelastic deformation $[r_N^{\mathrm{p}}, r_T^{\mathrm{p}}]$ has occurred.

It should be noticed that, if tangential displacements have already occurred, the model response is sensitive depending on the direction of the acting shear: therefore, if at a certain point the direction is inverted, it moves back towards the origin, causing a contraction; whereas if it is continued according to the direction in which the asperity develops, the result will be an increase in dilatancy. If displacements are generated from the origin to one side or the other, and the behaviour of the stresses is assumed according to Coulomb's friction law, there will be a friction angle ϕ in each plane of inclination μ which, with respect to the vertical axis that identifies the space of relative normal displacements will form the angle $\phi^+ = \phi + \mu$, as shown in Figure 3.13.

We now consider the plastic corrector approximation problem, where we impose finite increments of relative displacement $[\Delta r_N, \Delta r_T]$ from the virgin (initial) state and try to determine the interface stresses $[\sigma_N^{\mathrm{f}}, \sigma_T^{\mathrm{f}}]$.

The displacements from the initial state are equivalent to those of the Coulomb model and can therefore be expressed in terms of three different regions identified in the space of relative displacements (Figure 3.13). Each of these regions represents different contact conditions. For instance, if the pair of coordinates identifying the relative displacement is in Region 1, bounded by the half-lines containing the segments $\overline{O_0A} - \overline{O_0A'}$ having a vertex at the origin with an angle μ in the two half-planes identified by the r_T axis, the separation of the contact surfaces will occur: the interface stress components are zero and, consequently, the elastic components of the relative displacements $[r_N^{\mathrm{e}}, r_T^{\mathrm{e}}]$ are also zero. This condition includes the boundary defining Region 1, where the contact is barely maintained, but the interface stresses are zero.

For sake of simplicity, the elastic stiffnesses are assumed to be equal, $K_N = K_T$: hence the stress components $[\sigma_N^{\mathrm{f}}, \sigma_T^{\mathrm{f}}]$ have the same direction as the associated relative elastic displacement components $[r_N^{\mathrm{e}}, r_T^{\mathrm{e}}]$.

It is possible to define Region 3 (Figure 3.13) by drawing the half-lines containing the segments $\overline{O_0B} - \overline{O_0B'}$ with an angle ϕ^+ in the two half-planes identified by the r_N axis. If the pair of coordinates, identifying the relative displacement, lies in Region 3, or on the half-lines defining it, the total response is entirely elastic and the inelastic components are zero.

In the remaining areas of Figure 3.13, which configure Region 2, both the elastic and inelastic components of the relative displacements will be different from zero, as well as the stress components.

By considering the case where the coordinates of the relative displacement are represented by the vector $\overrightarrow{O_0C}$, a point D in $\overline{O_0A}$ can be located by drawing $\overrightarrow{DC}$ parallel to $\overline{O_0B}$. The inelastic component of the relative displacement is then given by the vector $\overrightarrow{O_0D}$, while the elastic component is given by $\overrightarrow{DC}$.

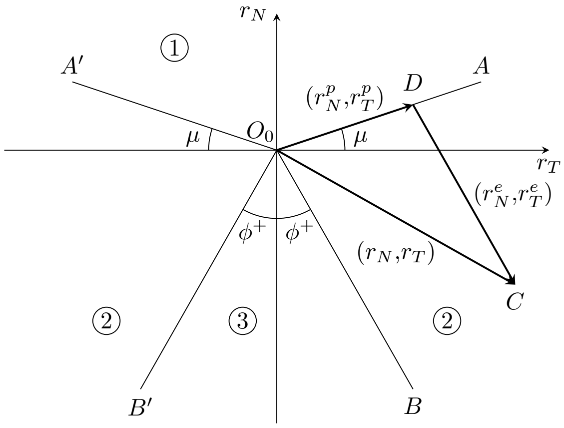

Figure 3.13: Diagram of the initial state of the interface.

The displacements from the position that configures the initial state are identical to those described by the Coulomb model. At the end of the first time step, the diagram in Figure 3.13 needs to be updated.

The updated conditions, however, differ from what the Coulomb model predicts. The interface is assumed to continue its displacement from the virgin position along the right-hand side of the asperity. The updated diagram in Figure 3.14 is constructed by drawing segments $\overline{O_1B}$ and $\overline{O_1C}$ with angles $\phi^+ = \phi + \mu$ and $\phi^- = \phi - \mu$, respectively. The vertex O_1 of these segments is forced to lie only along $\overline{O_0A}$, and must be updated at the end of each time step. Next, the state diagram is completed by drawing the segments $\overline{O_0B'}$ and $\overline{O_0C'}$ from the origin with angles equal to ϕ^+ and ϕ^-, respectively. It should be noted that at each increment of relative displacement of the interface, in addition to opening, expanding or contracting, it can also return towards the origin and rise along the opposite side's asperities.

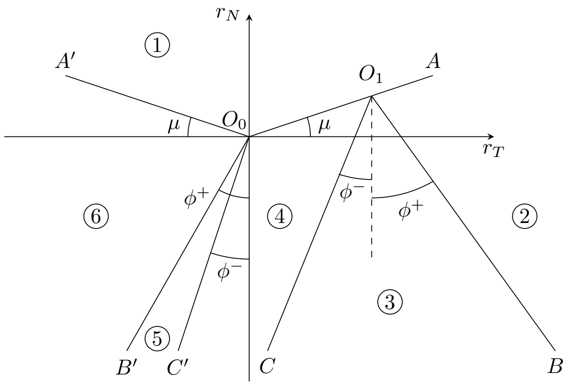

Figure 3.14: Updated state diagram for subsequent steps of relative displacements.

Note that now the point defining the components of the relative displacement of the interface can behave in any of six possible ways, depending on the region in which it is located. Consider an arbitrary increment, for example the $(n+1)th$ increment. Assume that the interface has moved from its virgin state position, that the right-hand side of the asperity is now in contact, and that the vertex has been updated to the point O_n, along the segment $\overline{O_0A}$ as shown in the following figures. In the general case, after a given increment, the new state point $[r_{N,n+1}, r_{T,n+1}]$, indicated by point E, is located at:

- Region 1: the interface element faces are separated, the stresses are zero and therefore the elastic components of the total relative displacements $[r_{N,n+1}, r_{T,n+1}]$ are both zero (Figure 3.15).
  If
  $$r_{N,n+1} \geq |r_{T,n+1}| \tan\mu \tag{3.49}$$
  the surfaces are not in contact. Therefore the update will be:
  $$\begin{aligned} & r^{\mathrm{e}}_{N,n+1} = r^{\mathrm{e}}_{T,n+1} = 0 & & \\ & r^{\mathrm{p}}_{N,n+1} = r_{N,n+1}, & & r^{\mathrm{p}}_{T,n+1} = r_{T,n+1} \\ & r^{\mathrm{dil}}_{N,n+1} = |r_{T,n+1}| \tan\mu, & & r^{\mathrm{dil}}_{T,n+1} = r_{T,n+1} \\ & \sigma_{N,n+1} = \sigma_{T,n+1} = 0 & & \end{aligned} \tag{3.50}$$

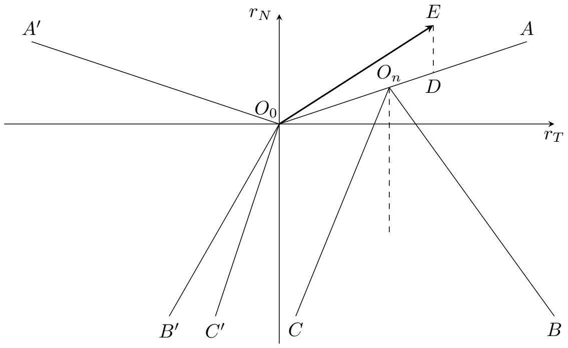

Figure 3.15: Region 1 state diagram.

- Region 2: more dilatancy occurs at the contact surface on the right side of the asperity. If $[r_{N,n+1}, r_{T,n+1}]$ is represented by the vector $\overrightarrow{O_0E}$, it is possible to locate a point D on the segment $\overline{O_0A}$ by drawing $\overline{DE}$ parallel to $\overline{O_nB}$. The plastic component of the relative displacement vector is then given by $\overline{O_0D}$ and the elastic component by $\overline{DE}$ (Figure 3.16).
  If
  $$r_{N,n+1} < r_{T,n+1}\,\mathrm{sgn}\left(r^{\mathrm{dil}}_{T,n}\right) \tan\mu \tag{3.51}$$
  and
  $$r_{N,n+1} > r^{\mathrm{dil}}_{N,n} - \left(r_{T,n+1} - r^{\mathrm{dil}}_{T,n}\right) \mathrm{sgn}\left(r^{\mathrm{dil}}_{T,n}\right) \cot\phi^{+} \tag{3.52}$$
  It is defined $a \equiv \overrightarrow{O_0D}$ and $b \equiv \overrightarrow{DE}$ (Figure 3.16), therefore:
  $$a = \frac{\left(r_{N,n+1} - r^{\mathrm{dil}}_{N,n}\right)\sin\phi^{+} + \left|r_{T,n+1} - r^{\mathrm{dil}}_{T,n}\right|\cos\phi^{+}}{\cos\left(\phi^{+} - \mu\right)} \tag{3.53}$$

and

$$b = \frac{\left(r_{N,n+1} - r^{\mathrm{dil}}_{N,n}\right)\cos\mu + \left|r_{T,n+1} - r^{\mathrm{dil}}_{T,n}\right|\sin\mu}{\cos\left(\phi^{+} - \mu\right)} \tag{3.54}$$

then

$$\begin{aligned}
r^{p}_{N,n+1} &= r^{\mathrm{dil}}_{N,n} + a\sin\mu, & r^{\mathrm{p}}_{T,n+1} &= r^{\mathrm{dil}}_{T,n} + a\cos\mu\,\mathrm{sgn}\left(r_{T,n+1} - r^{\mathrm{dil}}_{T,n}\right)\\
r^{\mathrm{e}}_{N,n+1} &= -b\cos\phi^{+}, & r^{\mathrm{e}}_{T,n+1} &= b\sin\phi^{+}\,\mathrm{sgn}\left(r_{T,n+1} - r^{\mathrm{dil}}_{T,n}\right)\\
r^{\mathrm{dil}}_{N,n+1} &= r^{\mathrm{p}}_{N,n+1}, & r^{\mathrm{dil}}_{T,n+1} &= r^{\mathrm{p}}_{T,n+1}\\
\sigma_{N,n+1} &= K_N r^{\mathrm{e}}_{N,n+1}, & \sigma_{T,n+1} &= K_T r^{\mathrm{e}}_{N,n+1}
\end{aligned} \tag{3.55}$$

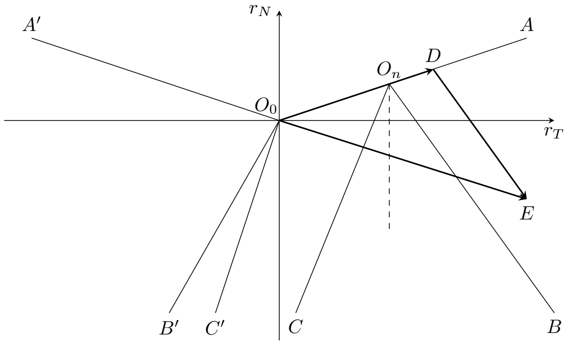

Figure 3.16: Region 2 state diagram.

- Region 3: the response is elastic. There is no variation in plastic deformation (Figure 3.17).
  If

$$r_{N,n+1} \leq r^{\mathrm{dil}}_{N,n} - \left(r_{T,n+1} - r^{\mathrm{dil}}_{T,n}\right)\mathrm{sgn}\left(r^{\mathrm{dil}}_{T,n}\right)\cot\phi^{+} \tag{3.56}$$

and

$$r_{N,n+1} \leq r^{\mathrm{dil}}_{N,\mathrm{n}} + \left(r_{T,n+1} - r^{\mathrm{dil}}_{T,n}\right)\mathrm{sgn}\left(r^{\mathrm{dil}}_{T,n}\right)\cot\phi^{-} \tag{3.57}$$

then the elastic response is

$$\begin{aligned}
r^{\mathrm{e}}_{N,n+1} &= r_{N,n+1} - r^{\mathrm{dil}}_{N,n}, & r^{\mathrm{e}}_{T,n+1} &= r_{T,n+1} - r^{\mathrm{dil}}_{T,n}\\
r^{\mathrm{p}}_{N,n+1} &= r^{\mathrm{dil}}_{N,n}, & r^{\mathrm{p}}_{T,n+1} &= r^{\mathrm{dil}}_{T,n}\\
r^{\mathrm{dil}}_{N,n+1} &= r^{\mathrm{dil}}_{N,n}, & r^{\mathrm{dil}}_{T,n+1} &= r^{\mathrm{dil}}_{T,n}\\
\sigma_{N,n+1} &= K_N r^{\mathrm{e}}_{N,n+1}, & \sigma^{\mathrm{e}}_{T,n+1} &= K_T r^{\mathrm{e}}_{T,n+1}
\end{aligned} \tag{3.58}$$

- Region 4: the interface faces are shifted towards the origin and both elastic and plastic displacements occur. The plastic component of the total displacements moves along the line of inclination μ on the right side in the direction of point O_0 (Figure

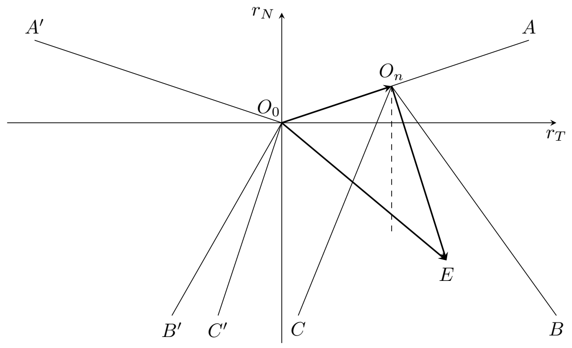

Figure 3.17: Region 3 state diagram.

3.18). To be within this region, the following conditions must be fulfilled simultaneously:

$$\begin{gathered} r_{N,n+1} < \left|r_{T,n+1}\right| \tan\mu \\ r_{N,n+1} > r^{\mathrm{dil}}_{N,n} + \left(r_{T,n+1} - r^{\mathrm{dil}}_{T,n}\right) \operatorname{sgn}\left(r^{\mathrm{dil}}_{T,n}\right) \cot\phi^- \end{gathered} \tag{3.59}$$

and

$$r_{N,n+1} < r_{T,n+1} \operatorname{sgn}\left(r^{\mathrm{dil}}_{T,n}\right) \cot\phi^- \tag{3.60}$$

therefore

$$\begin{aligned} a &= \frac{\left(r_{N,n+1} - r^{\mathrm{dil}}_{N,n}\right) \sin\phi^- + \left|r_{T,n+1} - r^{\mathrm{dil}}_{T,n}\right| \cos\phi^-}{\cos\left(\phi^- + \mu\right)} \\ b &= \frac{-\left(r_{N,n+1} - r^{\mathrm{dil}}_{N,n}\right) \cos\mu - \left|r_{T,n+1} - r^{\mathrm{dil}}_{T,n}\right| \sin\mu}{\cos\left(\phi^- + \mu\right)} \end{aligned} \tag{3.61}$$

then

$$\begin{aligned} r^{\mathrm{p}}_{N+n+1} &= r^{\mathrm{dil}}_{N,n} - a\sin\mu, & r^{\mathrm{p}}_{T,n+1} &= r^{\mathrm{dil}}_{T,n} + a\cos\mu \operatorname{sgn}\left(r_{T,n+1} - r^{\mathrm{dil}}_{T,n}\right) \\ r^{\mathrm{e}}_{N,n+1} &= -b\cos\phi^-, & r^{\mathrm{e}}_{T,n+1} &= b\sin\phi^- \operatorname{sgn}\left(r_{T,n+1} - r^{\mathrm{dil}}_{T,n}\right) \\ r^{\mathrm{dil}}_{N,n+1} &= r^{\mathrm{p}}_{N,n+1}, & r^{\mathrm{dil}}_{T,n+1} &= r^{\mathrm{p}}_{T,n+1} \\ \sigma_{N,n+1} &= K_N r^{\mathrm{e}}_{N,n+1}, & \sigma^{\mathrm{e}}_{T,n+1} &= K_T r^{\mathrm{e}}_{N,n+1} \end{aligned} \tag{3.62}$$

- Region 5: the interface returns to the initial (virgin) state and the plastic part vanishes (Figure 3.19). It enters again into an elastic region and recovers the friction model with angle ϕ^+. The conditions to be fulfilled are:

$$r_{N,n+1} \geq r_{T,n+1} \operatorname{sgn}\left(r^{\mathrm{dil}}_{T,n}\right) \cot\phi^- \tag{3.63}$$

and

$$r_{N,n+1} \leq r_{T,n+1} \operatorname{sgn}\left(r^{\mathrm{dil}}_{T,n}\right) \cot\phi^+ \tag{3.64}$$

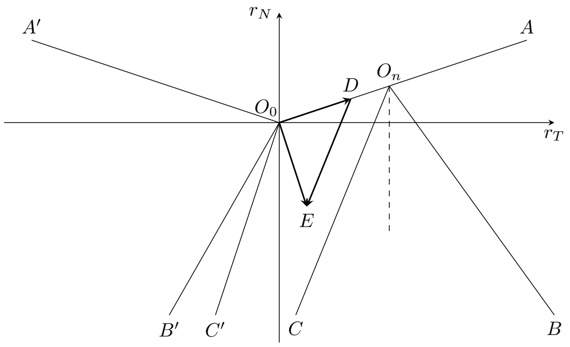

Figure 3.18: Region 4 state diagram.

then

$$\begin{aligned}
r^{\mathrm{e}}_{N,n+1} &= r_{N,n+1}, & r^{\mathrm{e}}_{T,n+1} &= r_{T,n+1} \\
r^{\mathrm{p}}_{N,n+1} &= 0, & r^{\mathrm{p}}_{T,n+1} &= 0 \\
r^{\mathrm{dil}}_{N,n+1} &= 0, & r^{\mathrm{dil}}_{T,n+1} &= 0 \\
\sigma_{N,n+1} &= K_N r^{\mathrm{e}}_{N,n+1}, & \sigma_{T,n+1} &= K_T r^{\mathrm{e}}_{N,n+1}
\end{aligned} \tag{3.65}$$

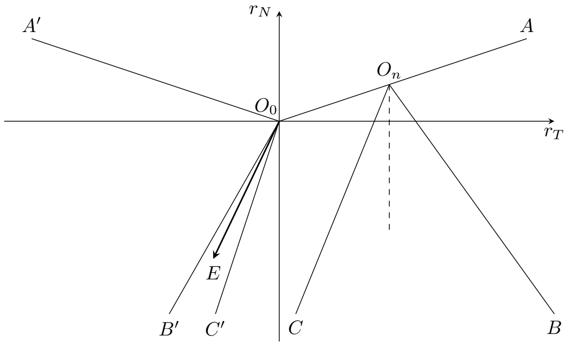

Figure 3.19: Region 5 state diagram.

- Region 6: dilatancy is triggered by contact of the left-hand faces of the asperity. Elastic and inelastic relative displacements are obtained as in Region 2 (Figure 3.20):

$$r_{N,n+1} < |r_{T,n+1}| \tan\mu \tag{3.66}$$

and

$$r_{N,n+1} > r_{T,n+1} \operatorname{sgn}\left(r^{\mathrm{dil}}_{T,n}\right) \cot\phi^{+} \tag{3.67}$$

as a result of this

$$\begin{aligned}
a &= \frac{r_{N,n+1}\sin\phi^{+} + |r_{T,n+1}|\cos\phi^{+}}{\cos\left(\phi^{+}-\mu\right)} \\
b &= \frac{-r_{N,n+1}\cos\mu + |r_{T,n+1}|\sin\mu}{\cos\left(\phi^{+}-\mu\right)}
\end{aligned} \tag{3.68}$$

then

$$\begin{aligned}
&r^{\mathrm{e}}_{N+n+1} = -b\cos\phi^{+}, && r^{\mathrm{e}}_{T,n+1} = -b\sin\phi^{+}\,\mathrm{sgn}\left(r^{\mathrm{dil}}_{T,n}\right)\\
&r^{\mathrm{p}}_{N,n+1} = a\sin\mu, && r^{\mathrm{p}}_{T,n+1} = -a\cos\mu\,\mathrm{sgn}\left(r^{\mathrm{dil}}_{T,n}\right)\\
&r^{\mathrm{dil}}_{N,n+1} = r^{\mathrm{p}}_{N,n+1}, && r^{\mathrm{dil}}_{T,n+1} = r^{\mathrm{p}}_{T,n+1}\\
&\sigma_{N,n+1} = K_N r^{\mathrm{e}}_{N,n+1}, && \sigma_{T,n+1} = K_T r^{\mathrm{e}}_{N,n+1}
\end{aligned} \tag{3.69}$$

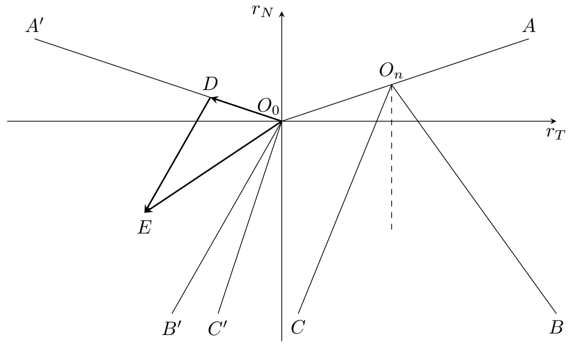

Figure 3.20: Region 6 state diagram.

The tangent matrix formulas, also used in the implementation of this constitutive law (Section 3.2), can be found in Snyman and Martin (1992).

Removing the restriction that $K_N = K_T$ (Figure 3.21), the segments $\overline{O_0B'}$ and $\overline{O_nB}$ will be characterised by the angle ψ^{+} with respect to the vertical:

$$\tan\psi^{+} = \frac{K_N}{K_T}\tan(\phi+\mu) \tag{3.70}$$

and the segments $\overline{O_0C'}$ and $\overline{O_nC}$ are denoted by the angle ψ^{-} with respect to the vertical:

$$\tan\psi^{-} = \frac{K_N}{K_T}\tan(\phi-\mu) \tag{3.71}$$

In this case, the relations defining the state of a point in a given region must be modified to ψ^{+} and ψ^{-} instead of ϕ^{+} and ϕ^{-}, respectively.

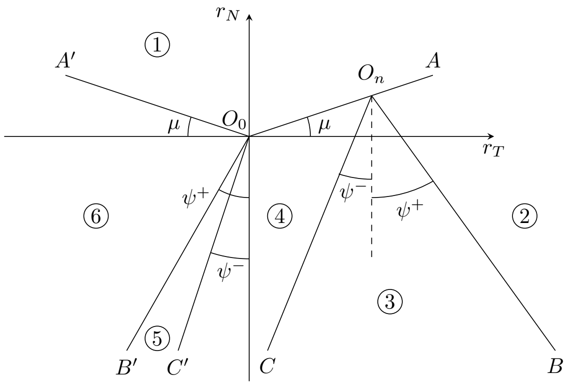

Figure 3.21: Updated state diagram for successive steps of relative displacements and $K_N \neq K_T$.

Finally, the model implemented modifies the proposal of Snyman and Martin (1992) in order to simulate the effect detected in experimental tests that occurs in load-unload cycles of tangential displacements which, upon returning to the origin, gives place to a residual normal displacement (bulking effect). This effect is taken into account by incorporating in the normal component of the frictional behaviour, the influence of the plastic displacement of the damage-plasticity model, in particular with the use of values of the parameter γ greater than zero. This effect will be illustrated in some examples of shear with constant compression presented in Chapter 4.

Chapter 4

Results

This chapter presents the results of the interface constitutive model in which cohesive behaviour based on scalar damage theory is combined with frictional behaviour, where chemical degradation is added, as presented in Chapter 3.

The model has been implemented through a set of constitutive subroutines for two-dimensional analysis. These subroutines only perform the calculation of stresses as a function of relative displacements. For constitutive verification, these subroutines are called from a main program which performs an iterative process when any prescribed degree of freedom corresponds to the stresses. Furthermore, once verified, the same subroutines can be incorporated into a Finite Element calculation program.

In order to illustrate the main features of the law, numerical simulations under pure tensile, tensile-shear and shear loading with constant compression, combined with different chemical degradation sequences, are presented.

The following parameters have been used: elastic stiffness $K_N = K_T = 10000$ MPa/mm (usually in interface elements elastic stiffness coefficients are adopted with very high values, penalty coefficients, in order to minimise elastic deformations); tensile strength $\chi_0 = 3$ MPa; cohesion $c_0 = 7$ MPa; internal friction coefficient $\tan\phi = 0.8785$; initial fracture energy $G^{\mathrm{I}}_{F_0} = 0.08$ N/mm; minimum fracture energy $G^{\mathrm{I}}_{F_{min}} = 0.3\ G^{\mathrm{I}}_{F_0}$; exponential factor affecting tensile softening $n = 3$; $\sigma^{\mathrm{dil}} = 1$ MPa; $\tan\mu = 0.1763$.

4.1 Pure tension tests

In this first example, increments of the normal relative displacement are imposed to the interface, in combination with increasing values of the chemical degradation parameter. Different sequences of displacement and degradation are considered. The results obtained for the different load cases, imposing positive increments of the relative displacement in the normal direction and chemical degradation, are shown from Figures 4.1 to 4.10. In the figures presented, the results on the left side show the curves of the normal stress σ_N as a function of the relative displacement in the normal direction to the interface plane r_N, while the right side of the figures show curves describing the evolution of the degradation during the simulation: the chemical degradation value η, depending on the type of simulation, can be expressed in relation to the normal relative displacements r_N, or in relation to a time variable considered dimensionless because the chemical degradation rates adopted are arbitrary. In these figures, for comparative purposes, the constitutive response of a purely mechanical reference simulation, i.e. without chemical degradation, is also shown.

In Test 1 and Test 2 (Figure 4.1) a normal relative displacement r_N is initially imposed until the tensile strength value χ_0 is reached (point a in Figure 4.1). From this point, the displacement r_N is gradually increased together with the chemical degradation parameter η until a degradation value of 0.50 is reached in Test 1 and 0.90 in Test 2. Comparing the Reference Test with Test 1 and Test 2, it is observed that a higher chemical degradation value implies a faster decay of the softening curve or, in other words, a faster decrease in the tensile strength of the interface. Since the law describing the decay of η is exponential (Equation (3.36)), the normal stresses will tend asymptotically to zero.

In the examples of degradation with tensile loading, it is illustrative to analyse the fracture surface evolution graphs along the loading process (in these examples the friction model only takes part in compression unloading processes). Figure 4.2 shows the evolution of the fracture surface throughout the simulation process, in relation to the points shown in Figure 4.1.

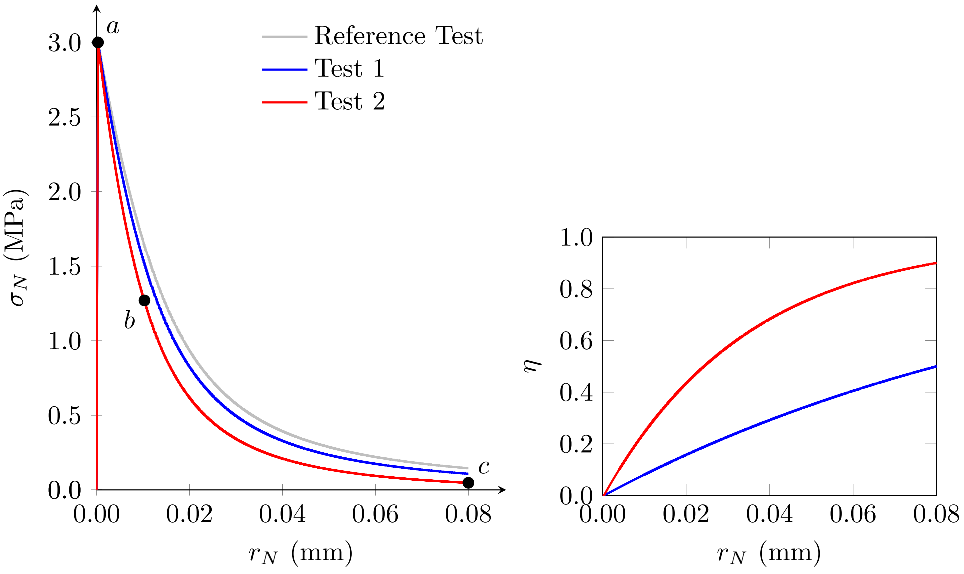

Figure 4.1: Pure tensile test combined with two different values of chemical degradation. The graph on the left shows the normal stress σ_N as a function of the relative normal displacement r_N of the interface. The graph on the right shows the evolution of the chemical degradation η in relation to the relative displacements in the normal direction.

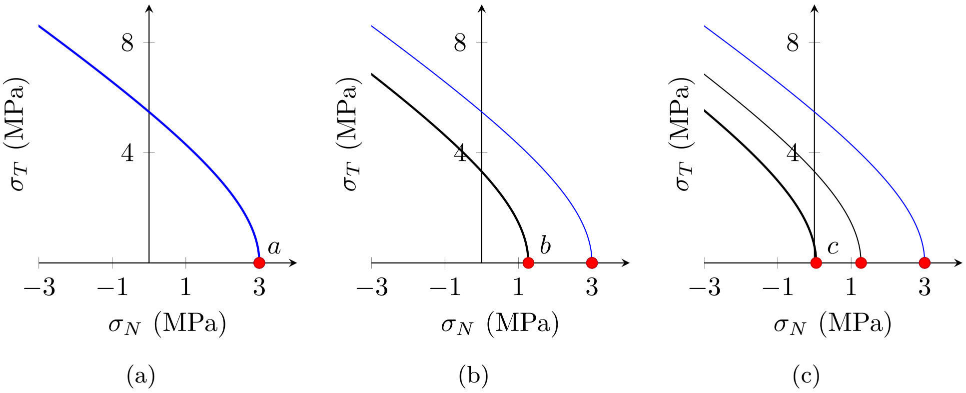

Figure 4.2: Fracture surface evolution for pure tensile tests combined with chemical degradation, in the case of Test 2: (a) undegraded initial state and tensile state of point a characterised by $\sigma_N = \chi_0$; (b) intermediate state in which a translation of the initial fracture surface occurred due to mechanical work and chemical degradation, point b characterised by $\sigma_N < \chi_0$; and (c) state at the end of the simulation, point c.

In Test 3 and Test 4 (Figure 4.3), a relative displacement r_N is initially imposed that is small enough not to exceed the value of χ_0 (points a and e in Figure 4.3), specifically such that $\sigma_N = 2$ MPa. This initial displacement r_N remains constant during the interval in which chemical degradation is gradually increased until it reaches a value of 0.20 in Test 3 and 0.40 in Test 4. According to Equation (3.34) (mostly the right-hand term), this leads to a decrease in tensile strength due to chemical degradation alone. From this point, a progressive increase of relative displacements is applied, without further chemical degradation, resulting in a decrease of the tensile strength of the material due only to the evolution of the mechanical process (term $\xi(L)$ in Equation (3.34)).

A different behaviour is observed by comparing the curve of Test 3 and the one of Test 4. In the first case, the chemical degradation is such that it reduces the tensile strength of the interface to a value approximately equal to 2.4 MPa (point c in Figure 4.3), in other words, a reduction of 20% with respect to χ_0; in the second case, a higher degradation value is imposed, which brings the tensile strength to a value of 1.8 MPa (point f in Figure 4.3), i.e., equal to 60% of χ_0. The chemical attack causes a decrease of the mechanical parameters, with a consequent displacement towards the origin of the initial hyperbola.

Referring to Test 3, once the chemical degradation process is completed, the interface is still in the elastic field (point $b \equiv a$ in Figure 4.4(b)), although the apex of the hyperbola has shifted (Figure 4.4(b)); when a progressive increase of r_N is then applied without additional η, the situation of $F = 0$ is reached (point c in Figure 4.4(c)) and subsequently to point d (Figure 4.4(d)).

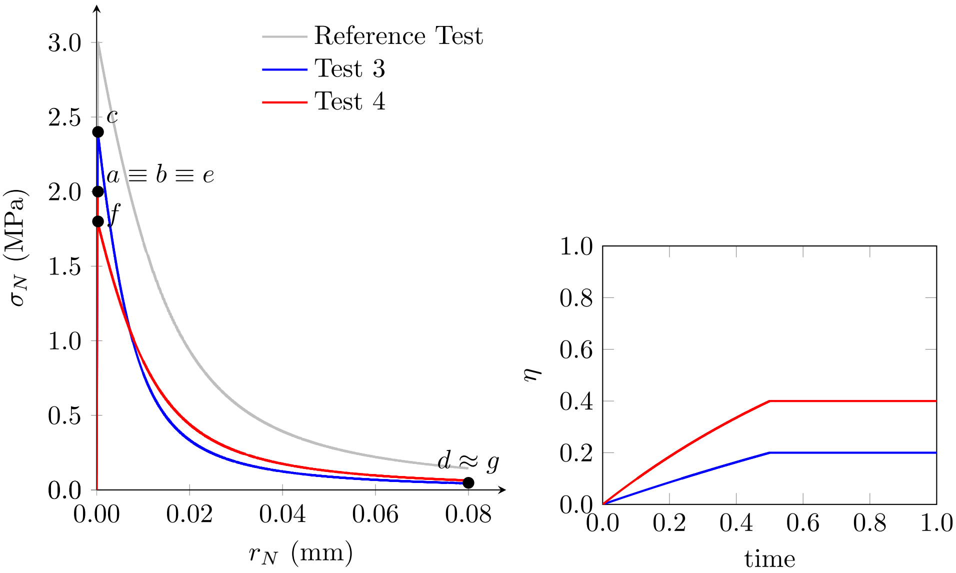

Figure 4.3: Pure tensile test combined with two different values of chemical degradation. The graph on the left shows the normal stress σ_N as a function of the relative normal displacement r_N of the interface. The graph on the right shows the evolution of the chemical degradation η in relation to time evolution.

In the case of Test 4, on the other hand, the chemical degradation process reduces the tensile strength up to point f (Figure 4.5(b)), even lower than point a of the initial load, and then a progressive increase of r_N is applied without additional η, which results in a reduction of the strength due only to the evolution of the cracking process (point g in Figure 4.5(c)).

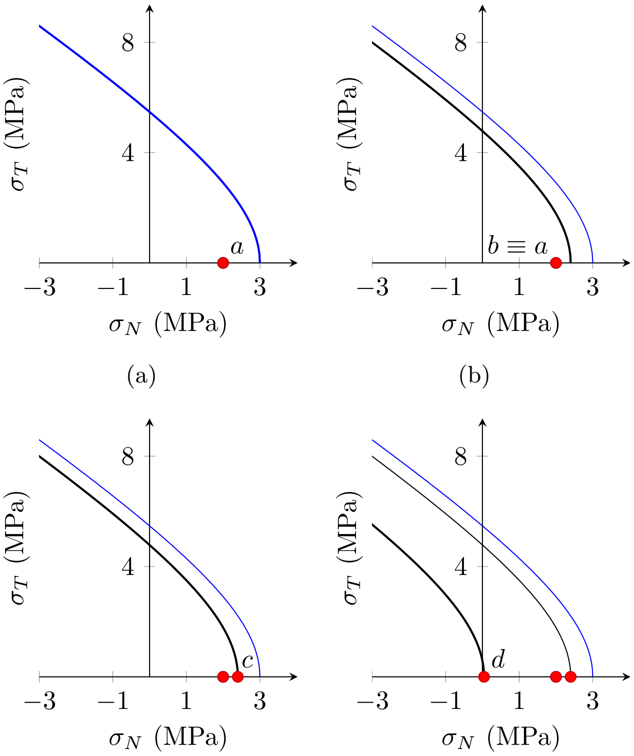

(a) (b)

(c) (d)

Figure 4.4: Fracture surface evolution for pure tensile tests combined with chemical degradation, in the case of Test 3: (a) initial undegraded state and tensile state at point a under elastic conditions, $\sigma_N < \chi_0$; (b) state at the end of chemical degradation, where the fracture surface is shifted but the stress state remains elastic, hence $b \equiv a$; (c) condition where through mechanical work the tensile strength limit of the material is reached, lower than χ_0 due to the chemical degradation process, point c; and (d) condition at the end of the simulation, point d.

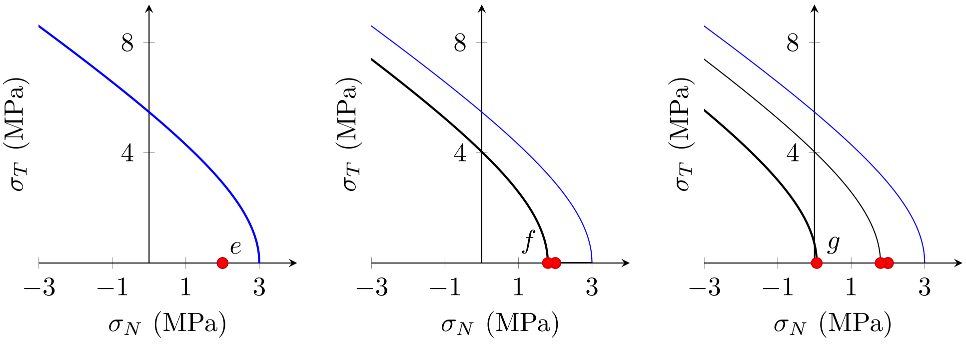

(a) (b) (c)

Figure 4.5: Fracture surface evolution for pure tensile tests combined with chemical degradation, in the case of Test 4: (a) initial state, point e; (b) state at point f at the end of chemical degradation; and (c) state at the end of the simulation at point g.

In Test 5, Test 6 and Test 7 (Figure 4.6) a relative normal displacement r_N is initially imposed up to a point on the softening branch (point b), which causes the shift of the fracture surface (Figure 4.7(b)). Then, while this value of normal relative displacement is maintained constant, the chemical degradation is progressively increased: in Test 5 the value of the chemical degradation prescribed is 0.10, while in Test 6 and Test 7 is 0.30 and 0.50, respectively. The chemical degradation causes a decrease of the normal stress in the interface (up to point c in Test 6 as shown in Figure 4.6 and Figure 4.7(c)), which means that there is a shifting of the fracture surface (the higher the η, the greater the shifting). From here on, a progressive increase of r_N is applied in all cases without further chemical degradation, leading to an increased loss of strength of the material due only to the work dissipated in the fracture process (point d in Figure 4.6 and Figure 4.7(d)). In Figure 4.7, the evolution of the fracture surface and the stress state at the points indicated in Figure 4.6, corresponding to Test 6, is presented.

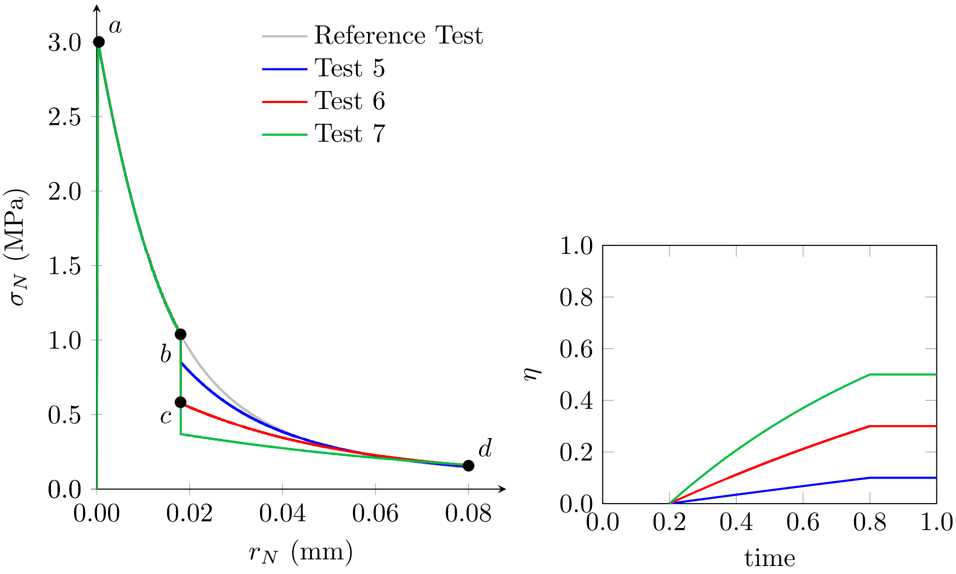

Figure 4.6: Pure tensile test combined with three different values of chemical degradation. The graph on the left shows the normal stress σ_N as a function of the relative normal displacement r_N of the interface. The graph on the right shows the evolution of the chemical degradation η in relation to time evolution.

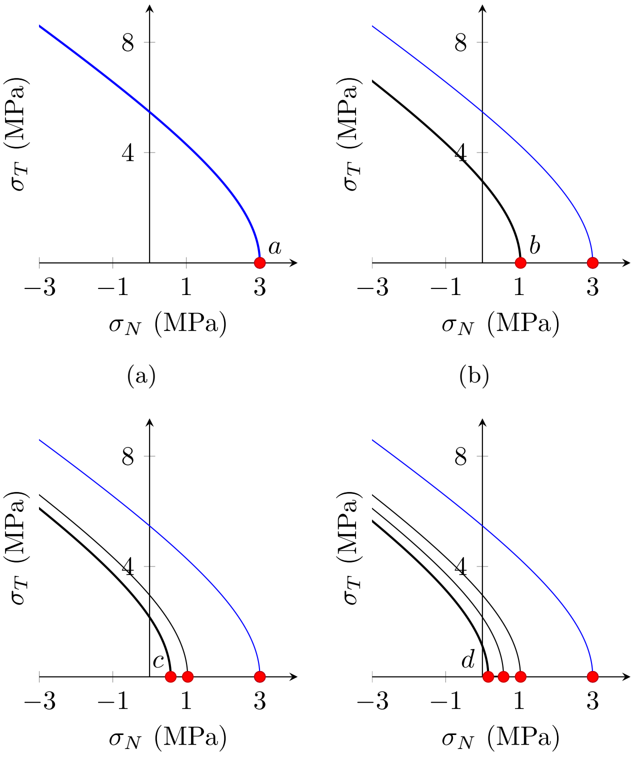

(a) (b) (c) (d)

Figure 4.7: Fracture surface evolution for pure tensile tests combined with chemical degradation, in the case of Test 6: (a) undegraded initial condition and stress state of point a characterised by $\sigma_N = \chi_0$; (b) condition where softening is reached only by mechanical work, point b; (c) condition at the end of chemical degradation, point c; (d) condition at the end of the simulation, point d.

From Test 8 to Test 11 (Figures 4.8 and 4.9), the behaviour with degradation combined with unloading and reloading is illustrated. A relative normal displacement r_N is imposed up to a point on the softening branch (this part coincides with the Reference Test). At this point an unloading is performed until reaching compressive stress levels; it is observed that in tension the unloading takes place with a reduced with stiffness but when the crack closes and stress becomes compression again, the initial stiffness is recovered. At the end of the unloading process, keeping the displacement values constant, the chemical degradation is gradually increased and then positive displacement increments are imposed again. In these simulations, two unloading-reloading processes are performed: the first at 0.015 mm aperture and the second at 0.030 mm aperture. Chemical degradation is only applied at the end of each of the unloading phases: in Tests 8 and 10 a value of η of 0.30 is reached (half in each phase), while in Tests 9 and 11 a value of 0.50 is reached.

In Test 8 and Test 9 (Figure 4.8) the unloading is secant towards the origin (as in Figure 2.4(b), damage behaviour) while in Test 10 and Test 11 (Figure 4.9) the unloading has a plastic relative displacement component (as in Figure 2.4(c), combination of damage and plasticity). As presented in Chapter 3, this effect is achieved in the model with the parameters B ($\beta/(1-\beta)$) and γ, which give different values of the plastic relative displacement. In the cases of Figure 4.8, $B = 0$ ($\beta = 0$) and $\gamma = 0$ have been used, while in the cases of Figure 4.9, $B = 1$ ($\beta = 0.5$) and $\gamma = 0$. It can be noticed in both figures that, as expected, when reloading after the action of chemical degradation in each phase, a lower point of the previous discharge softening curve is reached, with a more pronounced effect as the value of η is higher.

Figure 4.10 shows the evolution of the fracture surface and the stress state at the points indicated in Figure 4.9, corresponding to Test 11.

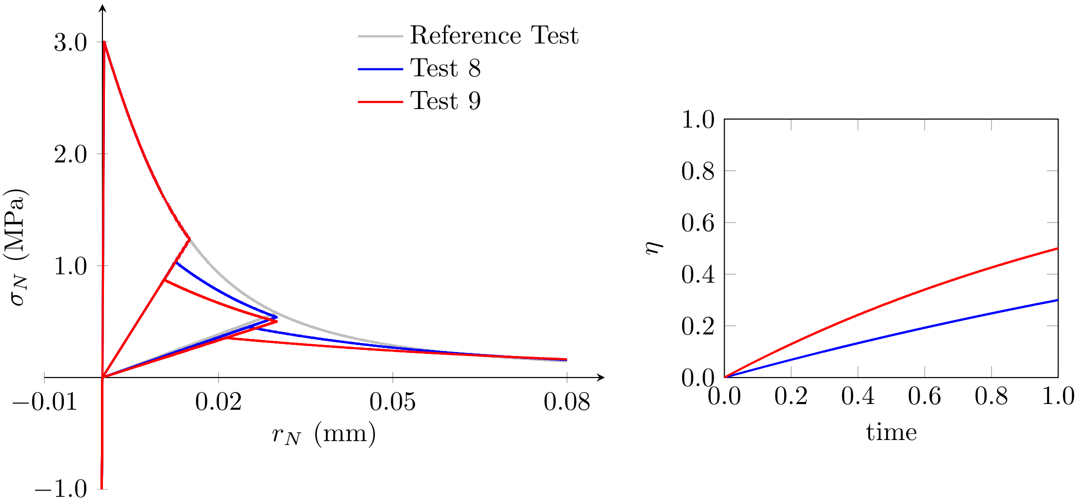

Figure 4.8: Pure tensile test and load-unload-reload processes ($B = 0$) combined with two different values of chemical degradation. The graph on the left shows the normal stress σ_N as a function of the relative normal displacement r_N of the interface. The graph on the right shows the evolution of the chemical degradation η as a function of time evolution.

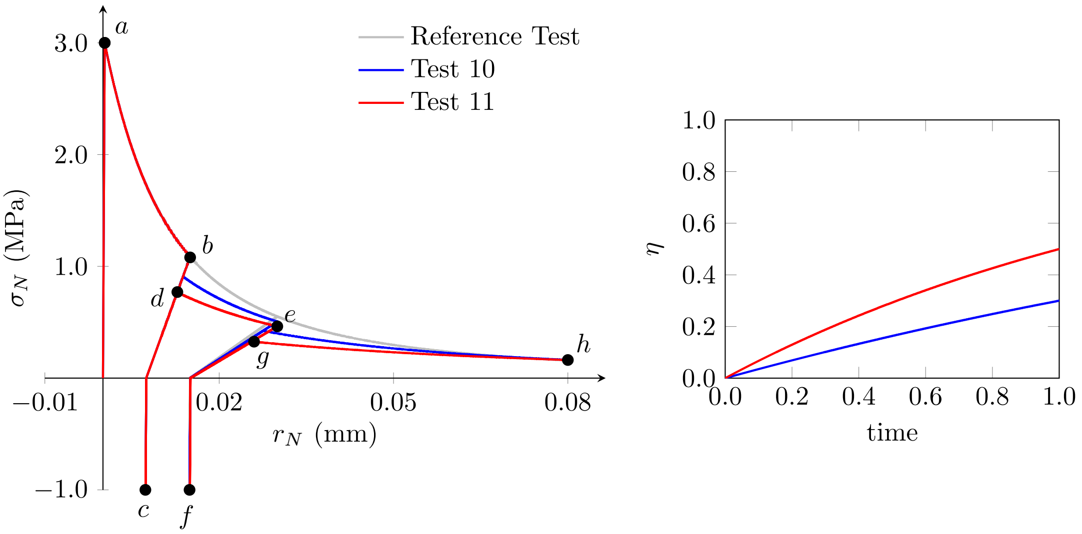

Figure 4.9: Pure tensile test and load-unload-reload processes ($B = 1$) combined with two different values of chemical degradation. The graph on the left shows the normal stress σ_N as a function of the relative normal displacement r_N of the interface. The graph on the right shows the evolution of the chemical degradation η as a function of time evolution.

4.2 Tension-shear tests

In the second example, tension combined with shear loading is considered.This is achieved by prescribing simultaneously the relative normal and shear displacements r_N and r_T with a fixed ratio $\theta = r_N/r_T = 30°$.

From Test 1 to Test 6 (Figures 4.11, 4.12 and 4.13) the chemical degradation was applied in the same way as in Test 1 and Test 2 (Figure 4.1) of Section 4.1, i.e. simultaneously with the relative displacement increments. From Test 7 to Test 10 (Figures 4.15 and 4.16), the chemical degradation was applied in the same way as in Test 8 to Test 11 of Section 4.1.

The simulations from Test 1 to Test 6 have the purpose of comparing the results in relation to the type of parameter that regulates the way the unloading process is carried out, in particular: Test 1 and Test 2 are characterised by $\gamma = \beta = 0$ equal to zero, Test 3 and Test 4 by $\gamma = 10$ and $\beta = 0$, while Test 5 and Test 6 by $\gamma = 0$ and $\beta = 1/2$. Tests 1, 3 and 5 are characterised by a total chemical degradation of 0.50, whereas Tests 2, 4 and 6 by a value of η of 0.99. It can be appreciated in Figures 4.11, 4.12 and 4.13 that the behaviour of the normal and shear stresses is similar to the trend of the corresponding pure tensile cases, and that when passing to the compression zone, a restitution of the initial stiffness is produced.

In Figure 4.14, the evolution of the fracture surface and the stress state at the points shown in Figure 4.11, corresponding to Test 1, is presented.

In Tests 7 to 10, results of combining mechanical actions and chemical degradation are

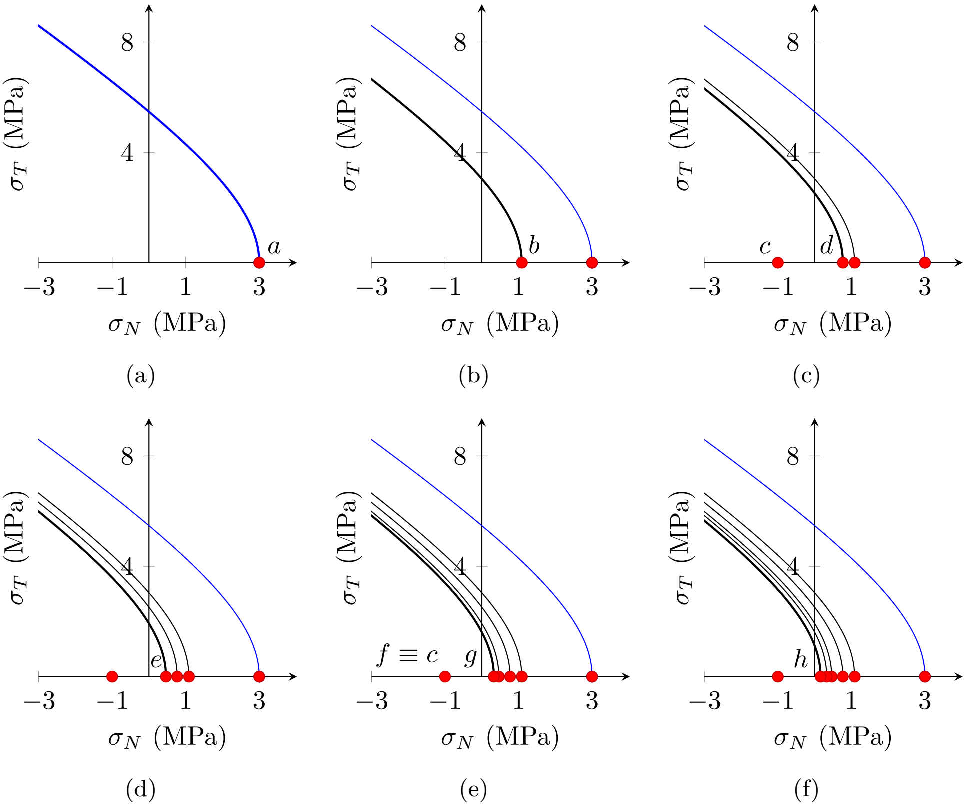

(a) (b) (c)

(d) (e) (f)

Figure 4.10: Fracture surface evolution in pure tensile tests combined with chemical degradation and load-unload-reload cycles, corresponding to Test 11: (a) undegraded initial state and tensile state at point a characterised by $\sigma_N = \chi_0$; (b) state at point b of the softening curve reached by mechanical work only; (c) state at the end of the first unloading process, point c, and at the end of the application of the first part of the chemical degradation and elastic reloading, point d; (d) condition at the end of the first reloading process, point e; (e) condition at the end of the second unloading process, point f, and at the end of the application of the second part of the chemical degradation and elastic reloading, point g; and (f) condition at the end of the simulation, point h.

presented in the same way as in Tests 8 to 11 (Figures 4.8 and 4.9) of the previous section. In these examples, the influence of the plastic relative displacement behaviour is obtained by varying the parameter γ. In the cases of Figure 4.15 $\gamma = 0$ and $B = 0$ have been used, while in the cases of Figure 4.16 $\gamma = 10$ and $B = 0$ have been used. In Tests 7 and 9 a value of η of 0.20 is reached (half in each phase), while in Tests 8 and 10 a value of 0.40 is reached. In both figures, it can be appreciated that the behaviour of the normal and shear components is similar to the one obtained in the similar example in pure tensile.

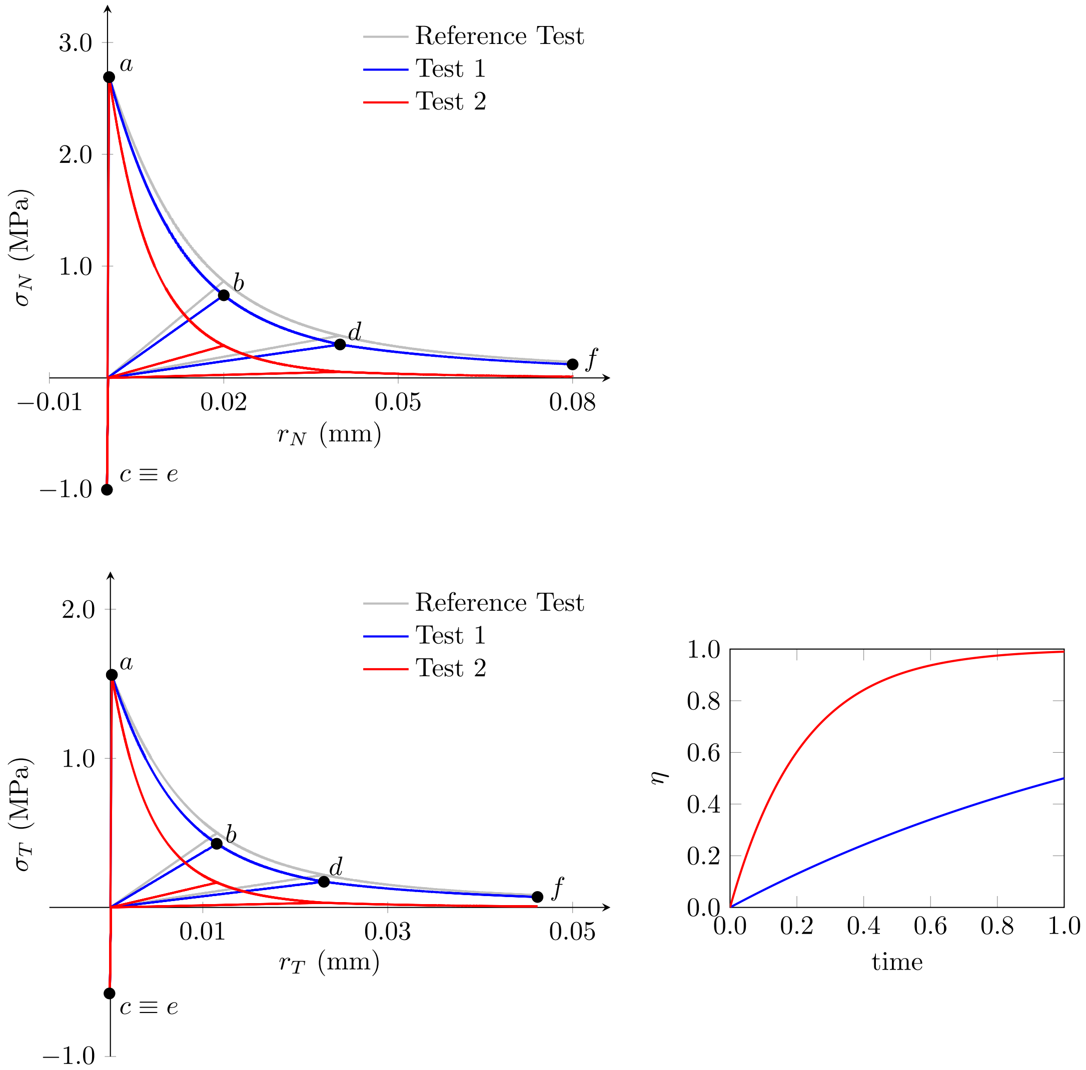

Figure 4.11: Tensile and shear test with $\theta = 30°$ combined with chemical degradation applied simultaneously with positive increments of the relative displacements in the softening branch; $\beta = 0$ and $\gamma = 0$. The graphs on the left show the evolution of each component of stress as a function of the corresponding relative displacement of the interface. The graph on the right shows the evolution of the chemical degradation η as a function of time evolution.

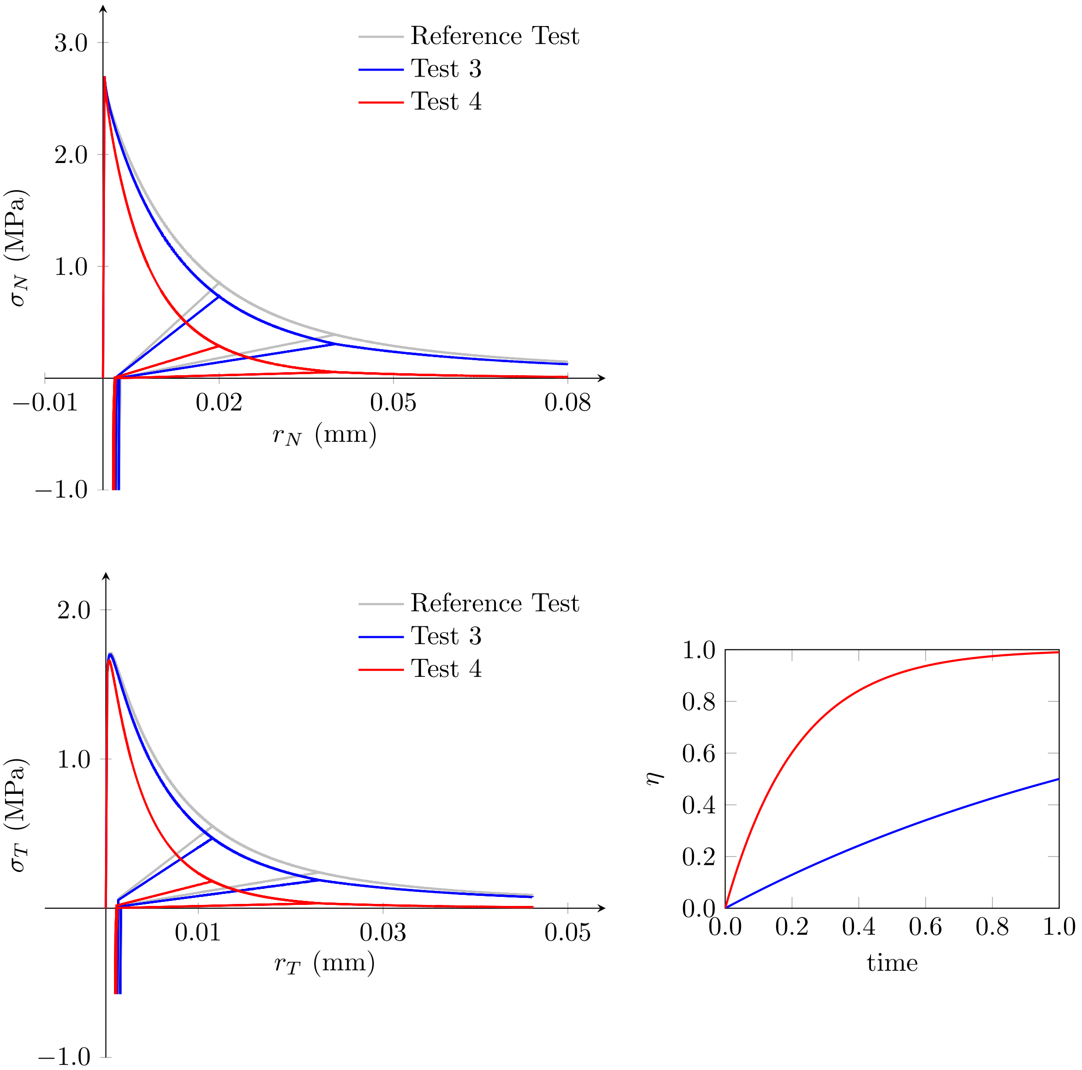

Figure 4.12: Tensile and shear test with $\theta = 30°$ combined with chemical degradation applied simultaneously with positive increments of the relative displacements in the softening branch; $\beta = 0$ and $\gamma = 10$. The graphs on the left show the evolution of each component of stress as a function of the corresponding relative displacement of the interface. The graph on the right shows the evolution of the chemical degradation η as a function of time evolution.

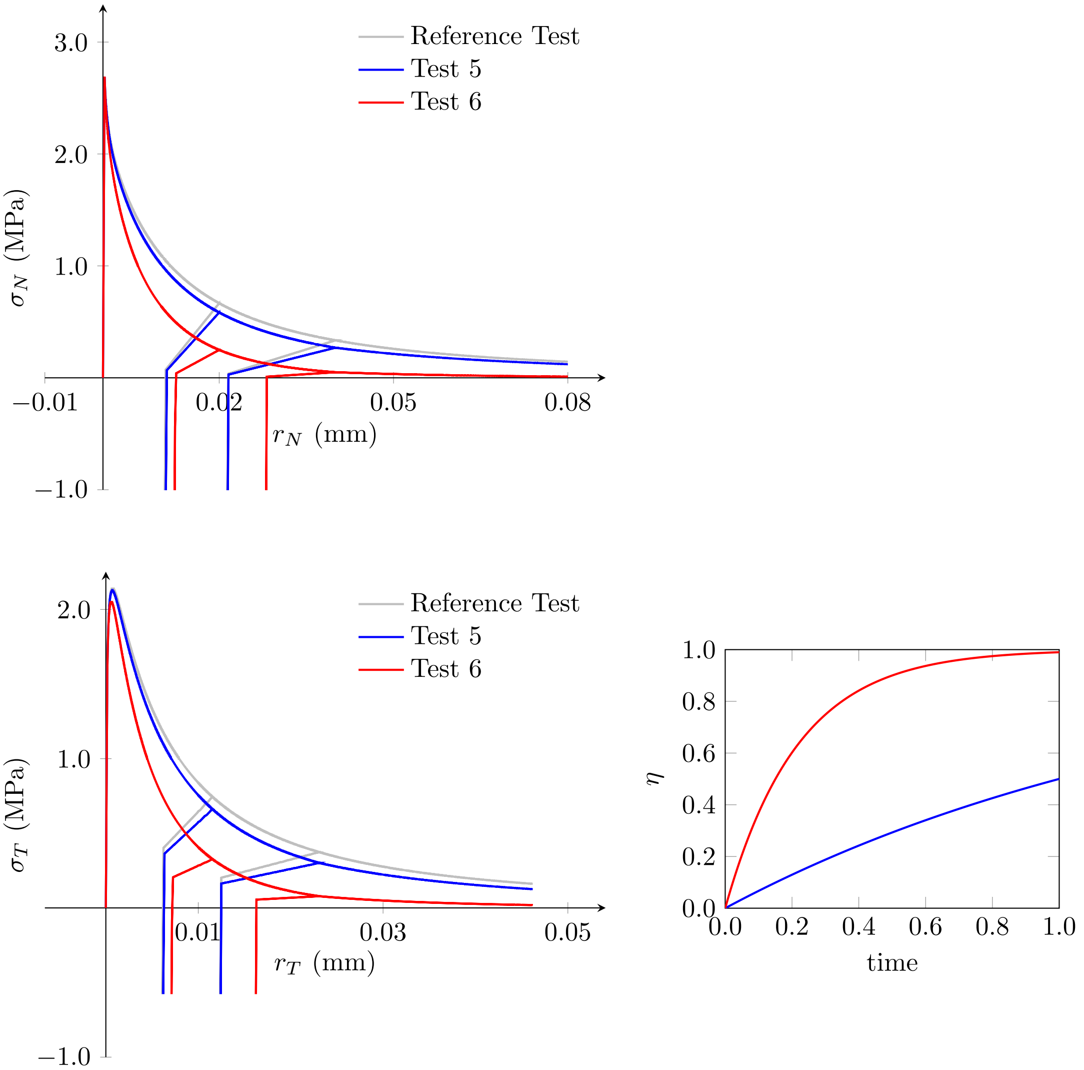

Figure 4.13: Tensile and shear test with $\theta = 30°$ combined with chemical degradation applied simultaneously with positive increments of the relative displacements in the softening branch; $\beta = 1/2$ and $\gamma = 0$. The graphs on the left show the evolution of each component of stress as a function of the corresponding relative displacement of the interface. The graph on the right shows the evolution of the chemical degradation η as a function of time evolution.

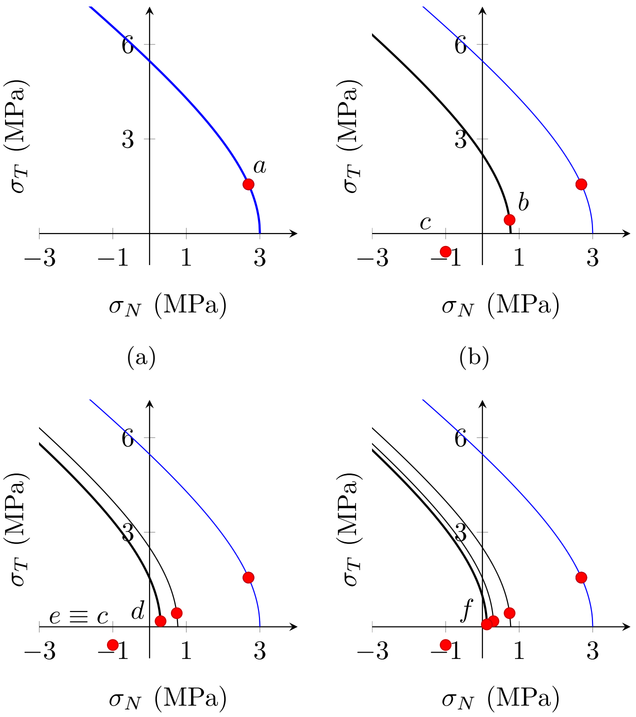

(a) (b)

(c) (d)

Figure 4.14: Fracture surface evolution for tensile and shear tests with $\theta = 30°$ combined with chemical degradation, in the case of Test 1: (a) undegraded initial condition and stress state of point a; (b) condition at which softening is reached by mechanical work and chemical degradation, point b, and at the end of the first unloading process, point c; (c) condition where softening is reached after the first reloading process by mechanical work and chemical degradation, point d, and at the end of the second unloading process, point $e \equiv c$; and (d) condition at the end of the simulation, after the second reloading process by mechanical work and chemical degradation, point f.

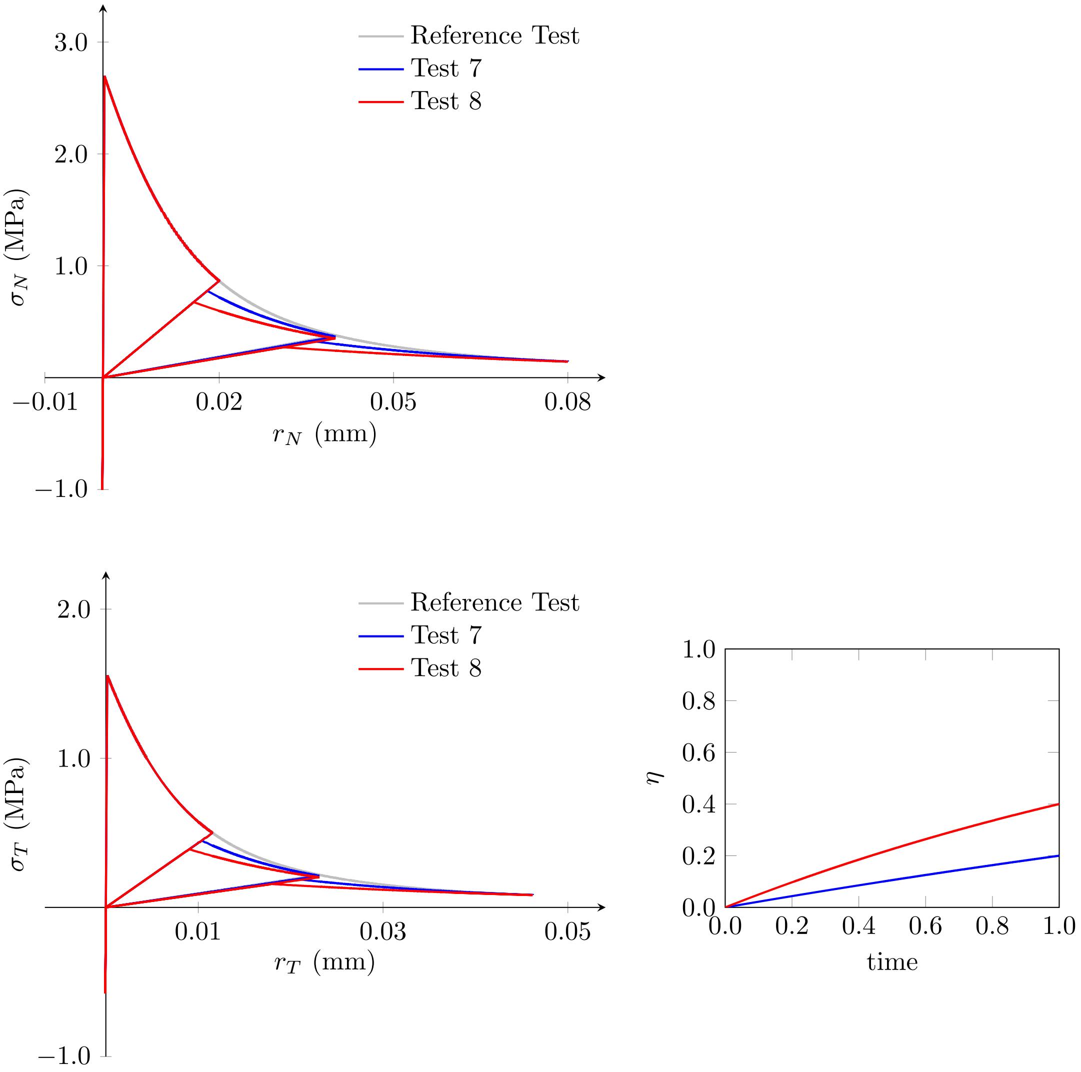

Figure 4.15: Tensile and shear test with $\theta = 30°$ combined with chemical degradation applied at the end of the unloading process with $\gamma = 0$. The graphs on the left show the evolution of each component of stress as a function of the corresponding relative displacement of the interface. The graph on the right shows the evolution of the chemical degradation η as a function of time evolution.

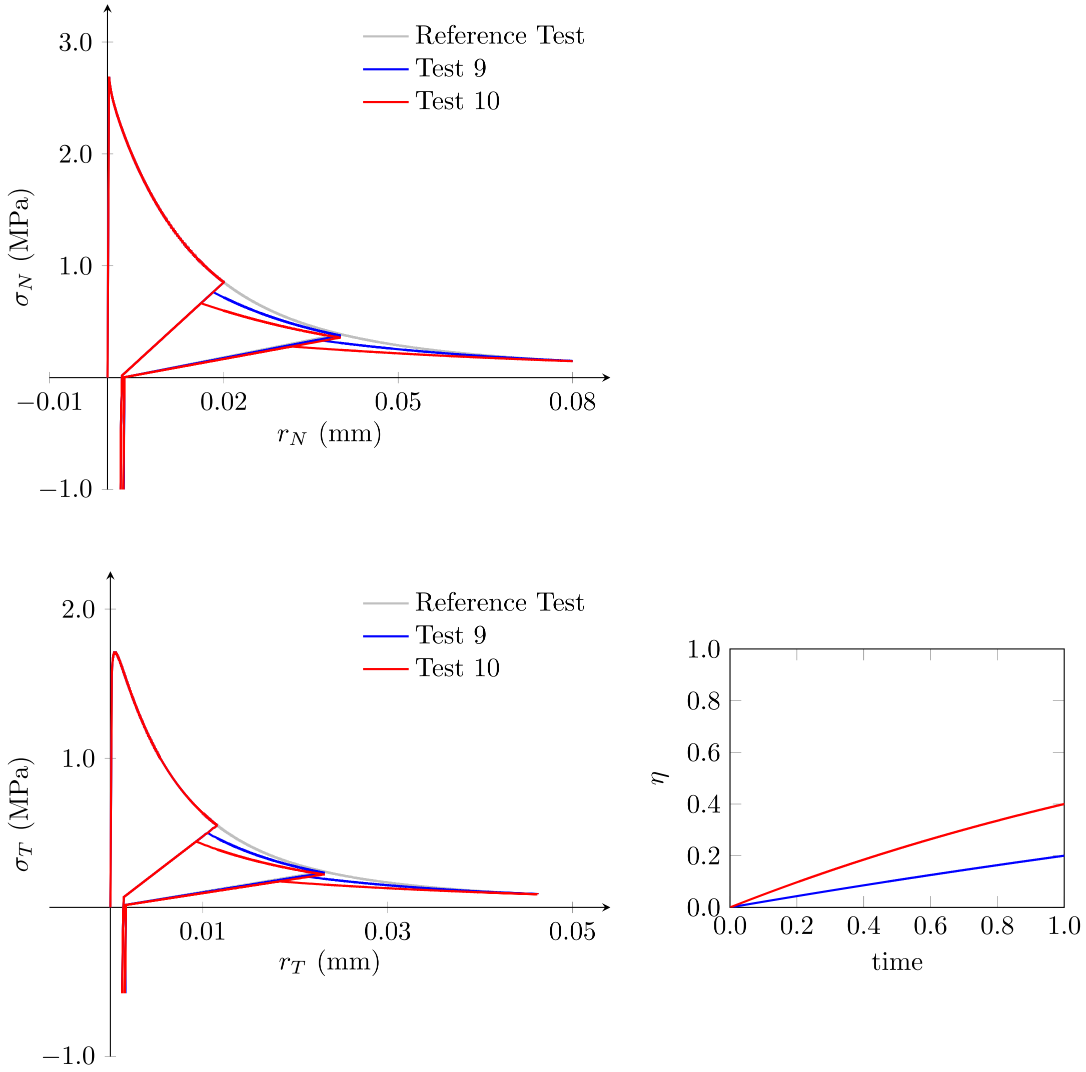

Figure 4.16: Tensile and shear test with $\theta = 30°$ combined with chemical degradation applied at the end of the unloading process with $\gamma = 10$. The graphs on the left show the evolution of each component of stress as a function of the corresponding relative displacement of the interface. The graph on the right shows the evolution of the chemical degradation η as a function of time evolution.

4.3 Shear with constant compression

In this section, examples of shear with constant compression in combination with different chemical degradation sequences are presented.

The different results obtained are shown from Figure 4.17 to Figure 4.31. In all cases, a compressive stress is initially applied ($\sigma_N = -2$ MPa, except in Tests 9 and 10 with $\sigma_N = -4$ MPa) and thereafter different combinations of increments of relative tangential displacement and chemical degradation are applied, always keeping the initial compression value constant; the cases called Reference Test are without any chemical degradation.

In Test 1 and Test 2 (Figure 4.17) the relative shear displacement r_T is imposed until the value of the shear strength is reached; from that point r_T is progressively increased together with the chemical degradation parameter η, respectively, up to a total value of 0.80 and 0.99. In the $\sigma_T - r_T$ graph, it can be observed that the curves degrade faster with increasing η value, and that they tend to a limit value of $\sigma_T = |\sigma_N| \tan \phi^+$, according to the friction model of Snyman and Martin (1992). It can be appreciated that the curves in Figure 4.17 exhibit a continuous softening unlike the behaviour with the elastoplastic law (Figure 3.5), which show an abrupt slope change at the point where the fracture energy G_F^{I} in Mode I is reached (the elastoplastic model has two energy parameters, besides the classical Mode I it also considers Mode IIa as seen in Section 3.1).

In Tests 3 and 4 (Figure 4.18) the increasing r_T is imposed until a stress value lower than the stress peak. Thereafter, while the achieved r_T is kept constant, the rate of chemical degradation is progressively increased to a value of 0.20 for Test 3 and 0.50 for Test 4. Once the application of chemical degradation is completed, r_T increments are applied again.

It can be noticed in Figure 4.18, that in Test 3 once the chemical degradation process is finished, the interface is still in elastic state and when a progressive increase of r_T without additional η is then applied, the situation of $F = 0$ is reached and subsequently softening occurs. In Test 4, the chemical degradation process decreases the tensile strength to a point below the initial load, and then a progressive increase of r_T is applied without additional η, which results in a reduction of the strength due only to the evolution of the cracking process.

In Tests 5 and 6 (Figure 4.19), relative shear displacements r_T have been imposed up to a certain value of stress in the softening branch. Thereafter, in both cases, the displacements are kept constant while the chemical degradation value is progressively increased until a value of 0.40 for Test 5 and 0.60 for Test 6 is reached. Finally, from this point on, a progressive increase of r_T is applied without any increase of the chemical degradation; it can be observed in the figure that, as expected, the degradation effect is more pronounced with higher values of η.

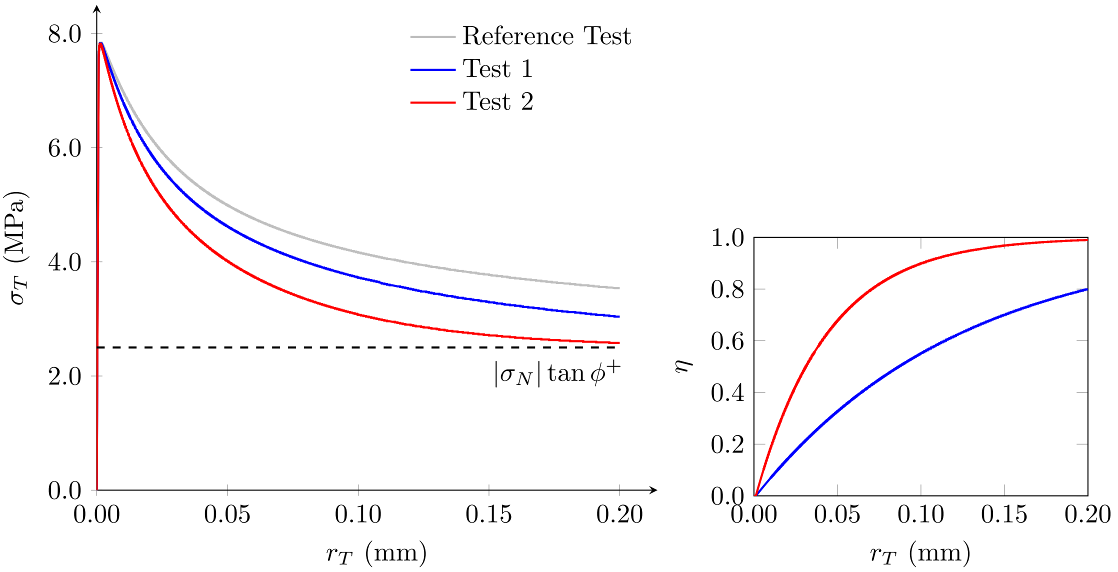

Figure 4.17: Shear with constant compression test combined with two different chemical degradation limit values. The graph on the left shows the tangential stress σ_T as a function of the relative shear displacement r_T of the interface. The graph on the right shows the evolution of the chemical degradation η in relation to the relative displacements in the tangential direction.

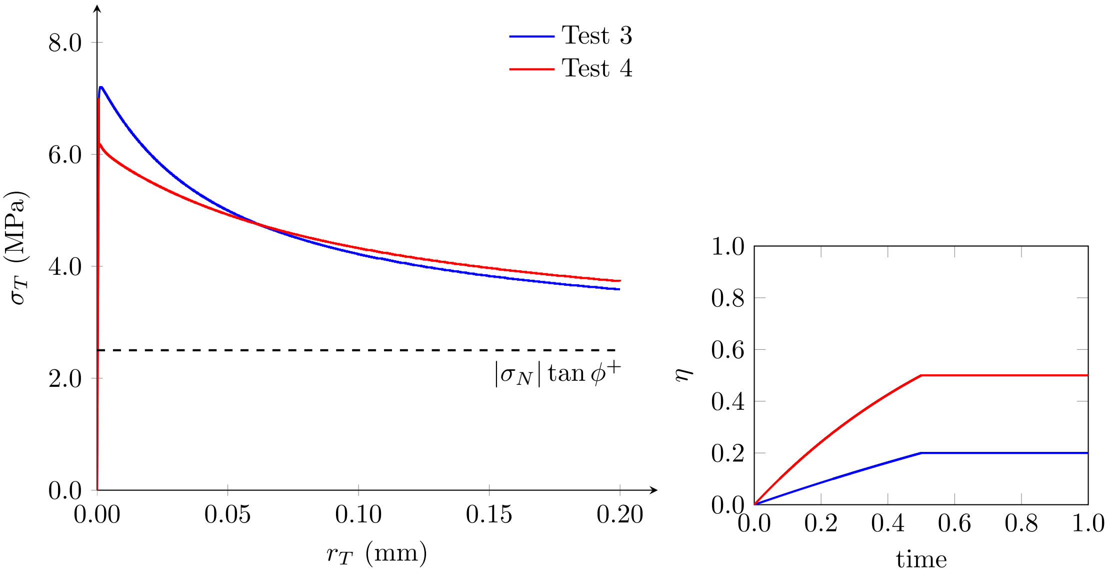

Figure 4.18: Shear with constant compression test combined with two different chemical degradation limit values. The graph on the left shows the tangential stress σ_T as a function of the relative shear displacement r_T of the interface. The graph on the right shows the evolution of the chemical degradation η in relation to time evolution.

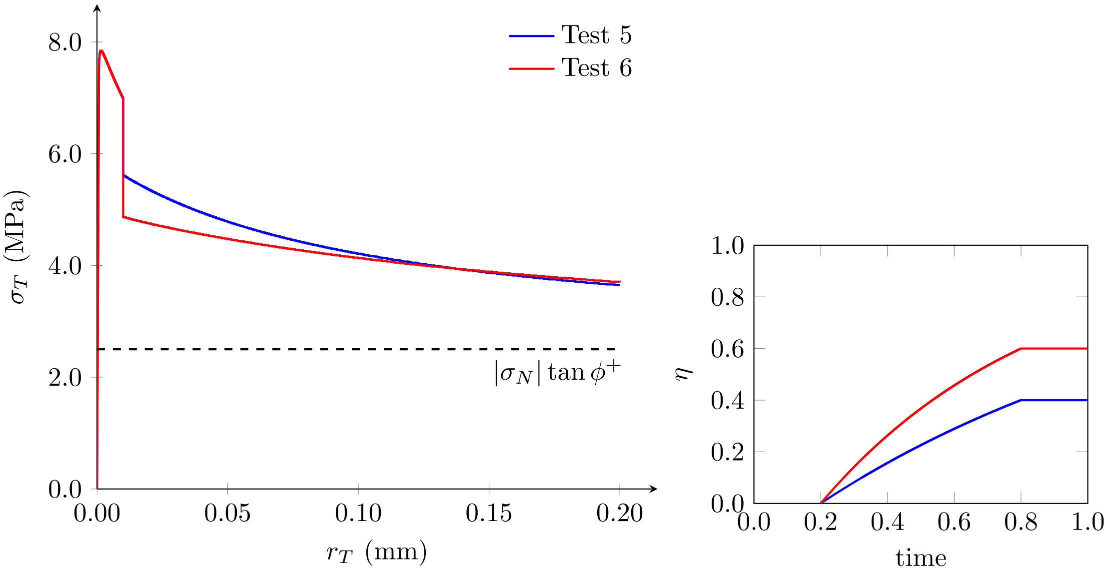

Figure 4.19: Shear with constant compression test combined with two different chemical degradation limit values. The graph on the left shows the tangential stress σ_T as a function of the relative shear displacement r_T of the interface. The graph on the right shows the evolution of the chemical degradation η in relation to time evolution.

The following examples show the results of shear with constant compression tests combined with chemical degradation, involving loading-unloading-reloading processes.

In Tests 7 and 8 (Figure 4.20) the relative shear displacement r_T is imposed until the value of the shear strength is reached; from this point on, r_T is progressively increased together with the chemical degradation parameter η. Once a certain maximum value of displacement is reached in the softening branch, the unloading process is initiated, which continues until the same r_T maximum is reached, but with the negative sign. At this point, the loading process is restarted by increasing r_T again, which continues up to the point where the first unloading process had started; from here on, the simultaneous imposition of tangential displacements and chemical degradation continues, until reaching the point where a new unloading process is started, and so on. At the end of the test, a chemical degradation value of 0.80 for Test 7 and 0.99 for Test 8 is reached.

In this figure and in the following similar ones, it can be seen that, regardless of the degree of chemical degradation, the combined action of the damage and friction models produces the following behaviour: once the peak value is reached in the damage model, the softening branch begins, with the contribution of the stresses of both partial models as a function of the value of D; the first unloading occurs elastically according to the initial stiffness, provided by the friction model; the second unloading occurs according to the secant stiffness given by the damage model until reaching the negative value with angle ϕ^-; already in the zone of negative shear displacement, the shear stresses of negative sign grow according to the initial stiffness, provided by the friction model, until reaching the negative value with angle ϕ^+; then, it starts to rise the asperities of the opposite side and the evolution of the shear stresses is resumed according to the secant stiffness given by the damage model; from this point, increments of relative shear displacement change and they become positive again and a similar behaviour to what happened in the unloading takes place. During the complete cycle that starts and returns to the point of the first unloading, the damage variable D remains constant at the value previously reached. As can be seen in Figure 4.20, similar considerations can be made for the successive cycles. It can be seen from the figure that the curves degrade to a greater value with increasing η and tend to a limiting value of $\sigma_T = |\sigma_N| \tan\phi^+$, according to the friction model of Snyman and Martin (1992).

In Figure 4.21 the graph of the evolution of the dilatancy represented by the ratio between r_N and r_T is illustrated. It can be observed in this figure, especially in the enlarged image on the right, that by reversing the direction of the shear displacements during the loading-unloading-reloading processes, there is a recovery of the dilatancy when returning to the initial position and that the degree of chemical degradation does not influence this behaviour.

Tests 9 and 10 (Figures 4.22 and 4.23) are similar in all aspects to Tests 7 and 8, with the difference that a compression of $\sigma_N = -4$ MPa has been applied. Comparing the results obtained in Figure 4.20 and Figure 4.22, it can be observed the influence of an increasing value of compression on the shear strength capacity of the interface and, logically, a higher value of residual stresses.

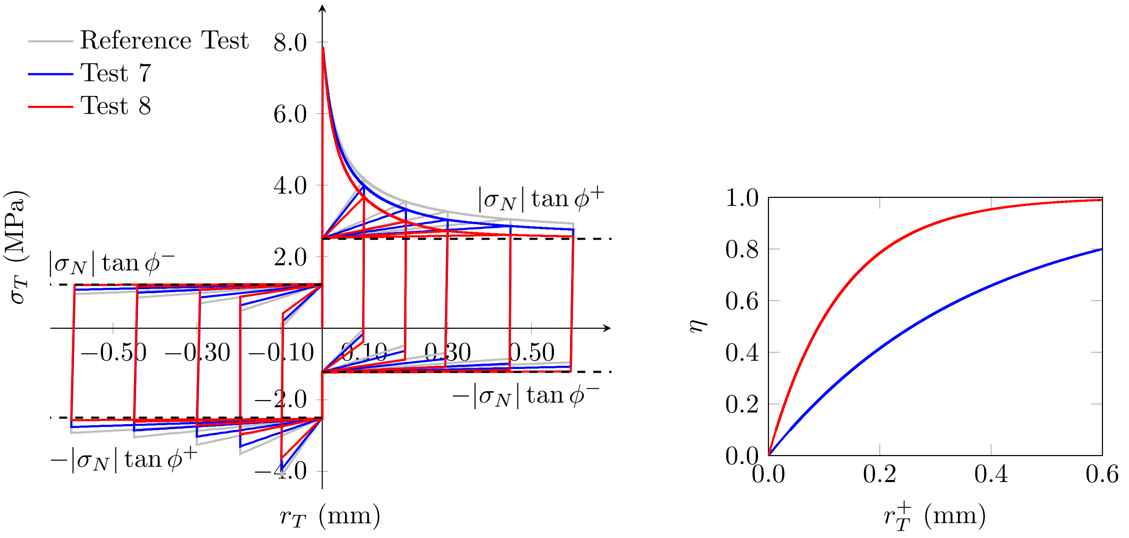

Figure 4.20: Shear with constant compression test at −2 MPa combined with two different chemical degradation limit values and loading-unloading-reloading cycles. The graph on the left shows the shear stress σ_T as a function of the relative tangential displacement r_T of the interface. The graph on the right shows the evolution of the chemical degradation η in relation to the positive relative shear displacements.

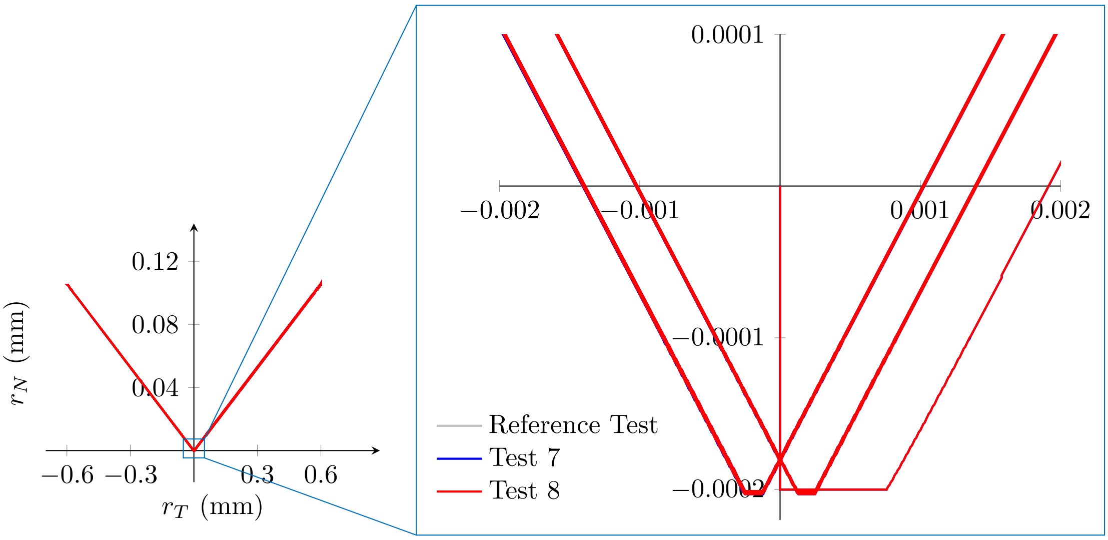

Figure 4.21: Shear with constant compression test at −2 MPa combined with two different chemical degradation limit values and loading-unloading-reloading cycles. The graph on the left shows the relative normal displacement r_N in relation to the relative shear displacement r_T of the interface (dilatancy). The graph on the right shows a zoom of the highlighted part of the image on the left.

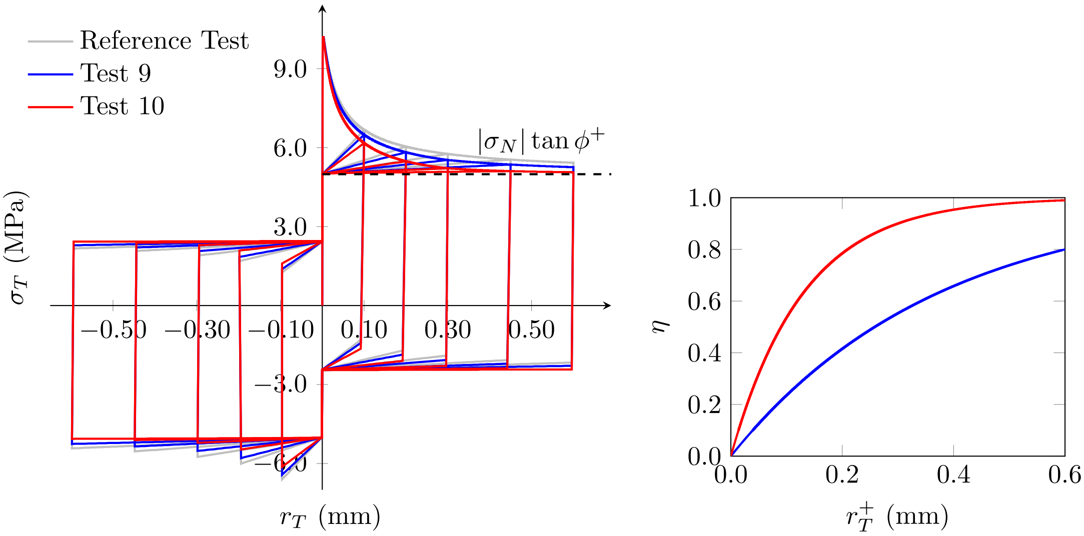

Figure 4.22: Shear with constant compression test at −4 MPa combined with two different chemical degradation limit values and loading-unloading-reloading cycles. The graph on the left shows the shear stress σ_T as a function of the relative tangential displacement r_T of the interface. The graph on the right shows the evolution of the chemical degradation η in relation to the positive relative shear displacements.

Tests 11 and 12 (Figures 4.24 and 4.25) are similar to Tests 7 and 8, except that now the combined increases in relative shear displacements and chemical degradation occur in an alternating way in shear zones with positive and negative sign. The relative tangential

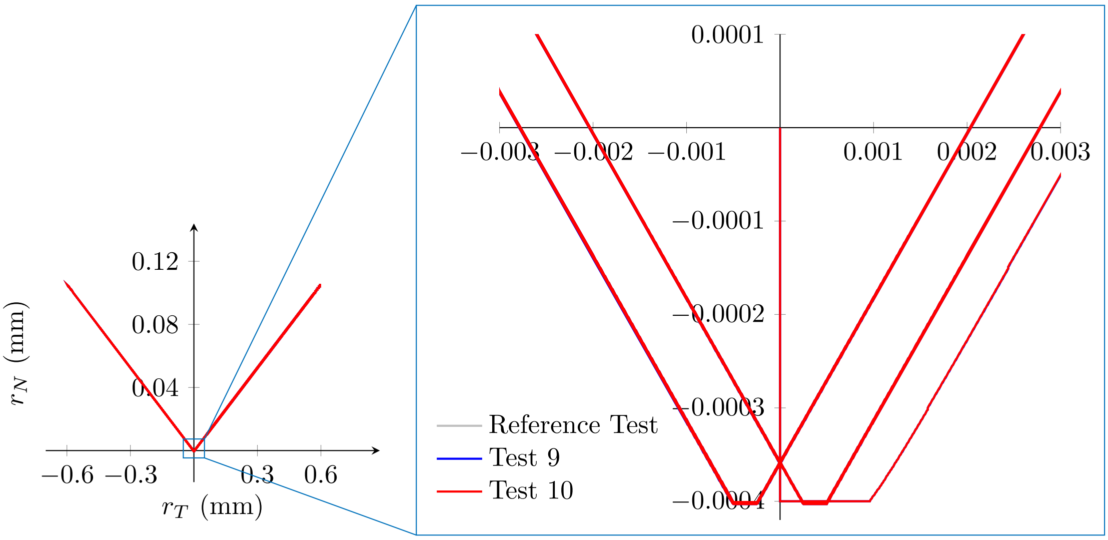

Figure 4.23: Shear with constant compression test at −4 MPa combined with two different chemical degradation limit values and loading-unloading-reloading cycles. The graph on the left shows the relative normal displacement r_N in relation to the relative shear displacement r_T of the interface (dilatancy). The graph on the right shows a zoom of the highlighted part of the image on the left.

displacement r_T is imposed until the shear strength value is reached; thereafter r_T is progressively increased together with the chemical degradation parameter η. Once a certain maximum displacement value is reached in the softening branch, the unloading process starts and continues until the same r_T maximum value is reached, but with negative sign. Then, negative r_T increments continue to be imposed together with chemical degradation, until a certain upper negative value of tangential relative displacements is reached. Then, positive increments of r_T are imposed again until the opposite value of positive sign is reached; from here on, the simultaneous imposition of tangential displacements and chemical degradation is continued, and then repeated in a similar way. At the end of the test a chemical degradation value of 0.80 for Test 11 and 0.99 for Test 12 is achieved.

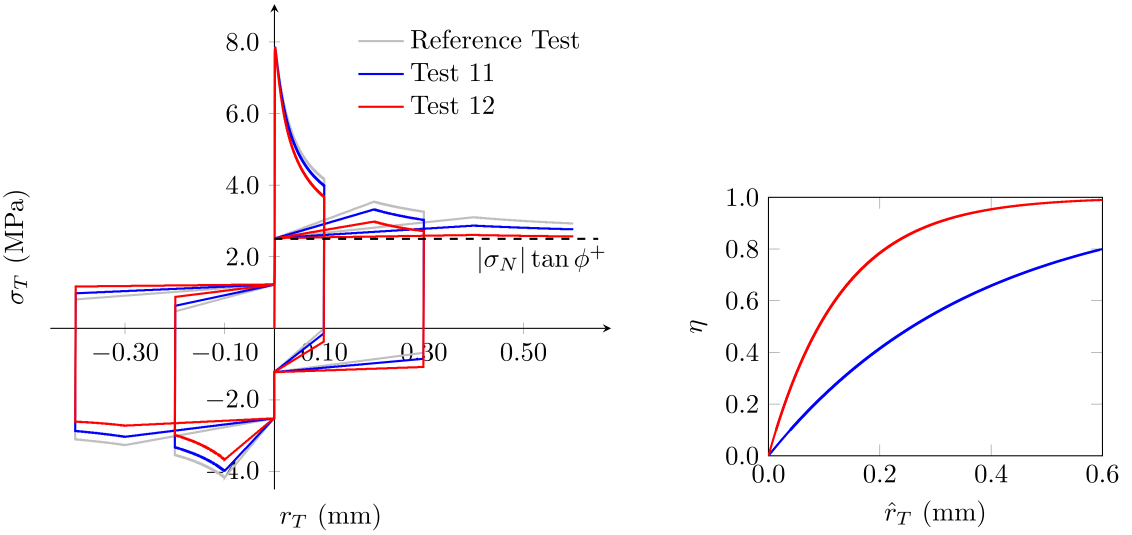

Figure 4.24: Shear with constant compression test at −2 MPa combined with two different chemical degradation limit values and loading-unloading-reloading cycles. The graph on the left shows the shear stress σ_T as a function of the relative tangential displacement r_T of the interface. The graph on the right shows the evolution of the chemical degradation η in relation to the accumulated increments of the relative tangential displacements on both sides, which we will call $\hat{r}_T$.

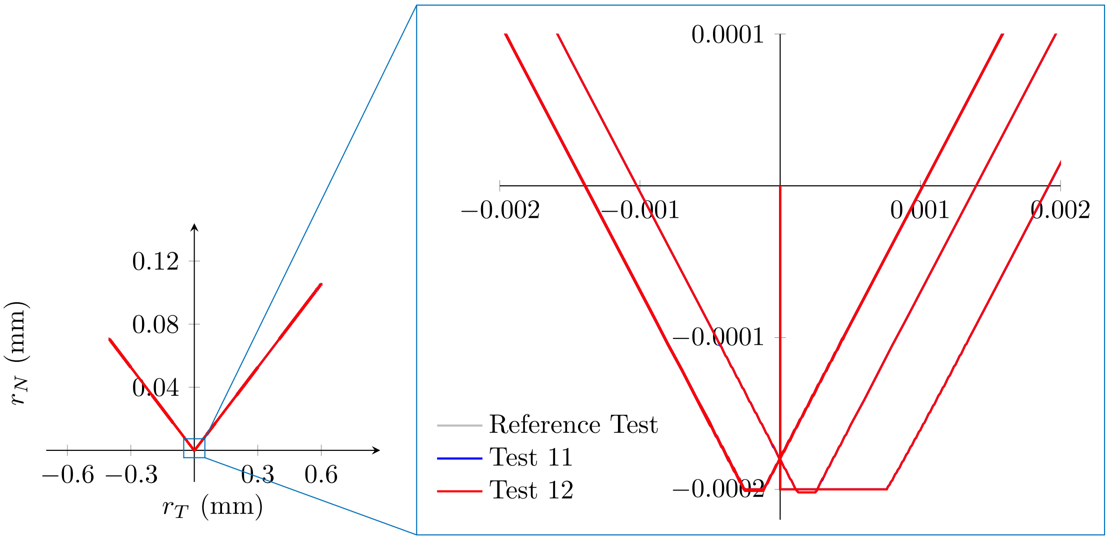

Figure 4.25: Shear with constant compression test at −2 MPa combined with two different chemical degradation limit values and loading-unloading-reloading cycles. The graph on the left shows the relative normal displacement r_N in relation to the relative shear displacement r_T of the interface (dilatance). The graph on the right shows a zoom of the highlighted part of the image on the left.

Next, the results of Test 13 (Figures 4.26 and 4.27) and Test 14 (Figures 4.28 and 4.29) are presented, compared to the Reference Test in which no chemical degradation is applied.

These simulations are analogous to Tests 7 and 8: the mode of application of the tangential displacement and chemical degradation increments and the value of the constant compression are equivalent, so a more detailed explanation is referred to that section; however, it is now of interest to illustrate the influence of the parameter γ. As discussed in Section 3.2.2 where the friction model is described, it is possible to simulate the effect that occurs in load-unload cycles of tangential displacements that on return to the origin gives place to a residual normal displacement, known also as bulking effect, which is taken into account with the plastic displacement of the damage model, specifically with the use of values of γ greater than zero. This effect has been detected in experimental tests.

In Tests 13 and 14, results are presented for the reference curve ($\eta = 0$) and with a chemical degradation value η equal to 0.99, with different values of parameter γ in each case: with a value of five for Test 13 and a value of ten for Test 14. In Figures 4.27 and 4.29 it can be observed how increasing values of γ affect the dilatancy recovery behaviour on unloading back to the initial position, with a larger residual normal displacement with increasing γ value.

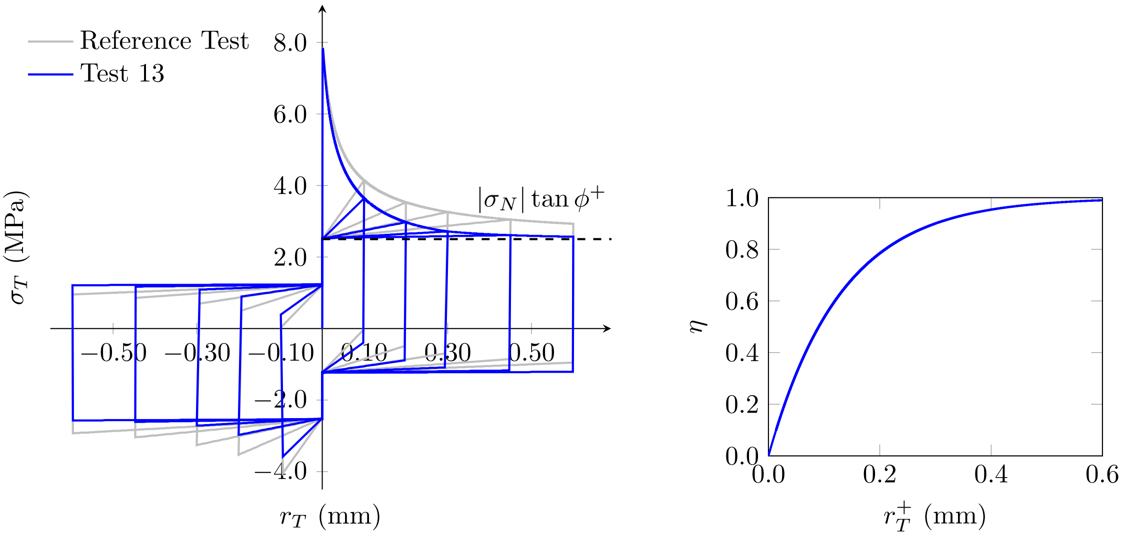

Figure 4.26: Shear with constant compression test at −2 MPa combined with chemical degradation, load-unload-reload cycles and a parameter value $\gamma = 5$. The graph on the left shows the tangential stress σ_T as a function of the relative tangential displacement r_T of the interface. The graph on the right shows the evolution of the chemical degradation η as a function of the positive relative tangential displacements.

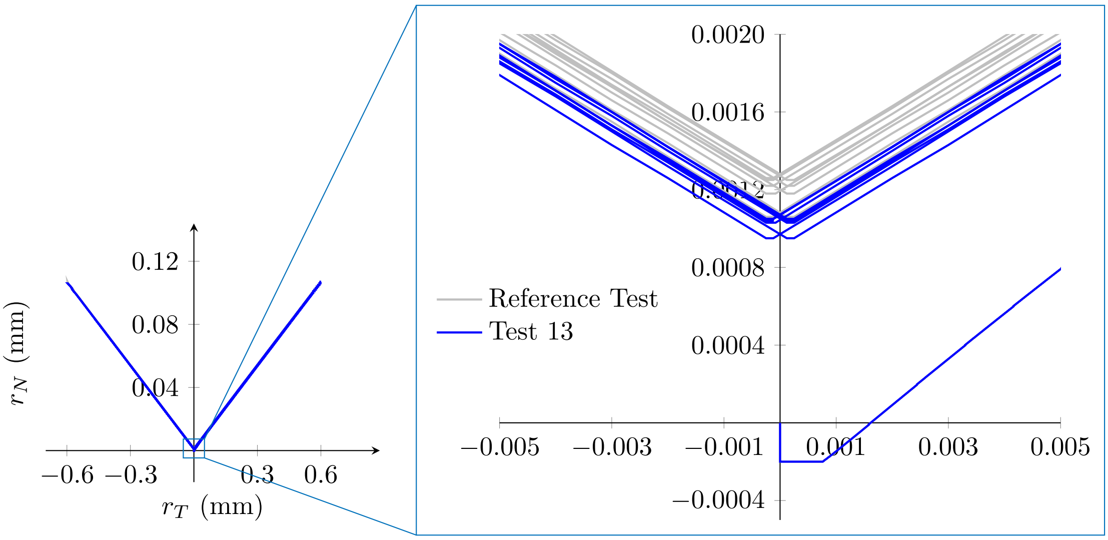

Figure 4.27: Shear with constant compression test at −2 MPa combined with chemical degradation, load-unload-reload cycles and a parameter value $\gamma = 5$. The graph on the left shows the relative normal displacement r_N in relation to the relative tangential displacement r_T of the interface (dilatancy). The graph on the right shows a zoom of the highlighted part of the image on the left.

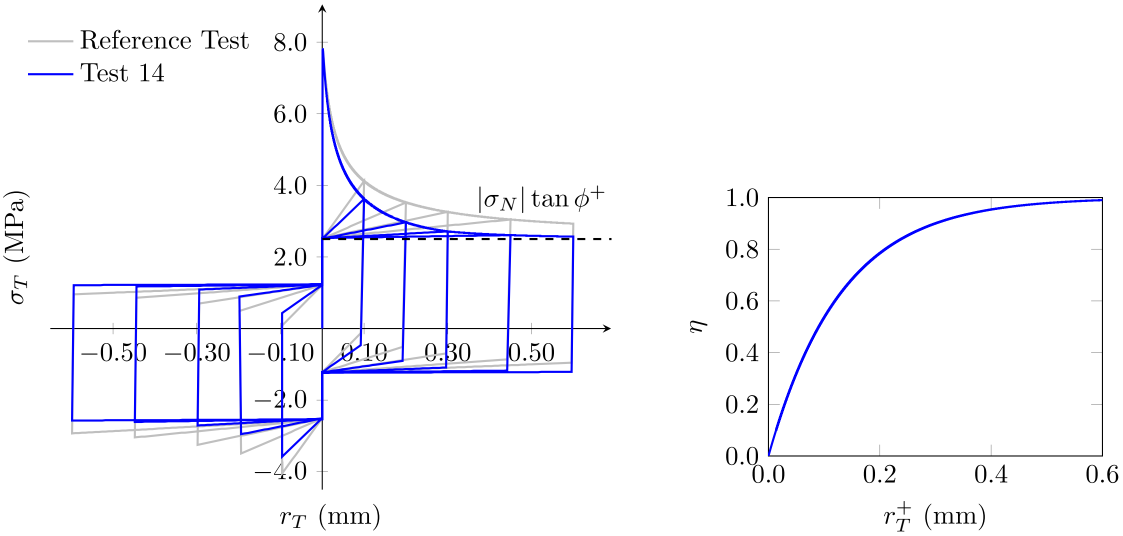

Figure 4.28: Shear with constant compression test at −2 MPa combined with chemical degradation, load-unload-reload cycles and a parameter value $\gamma = 10$. The graph on the left shows the tangential stress σ_T as a function of the relative tangential displacement r_T of the interface. The graph on the right shows the evolution of the chemical degradation η as a function of the positive relative tangential displacements.

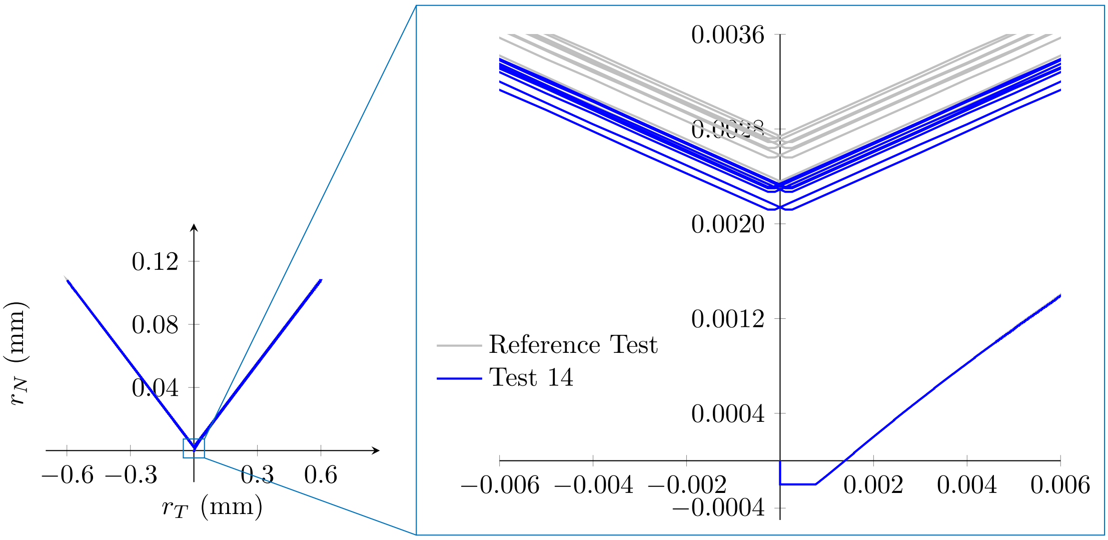

Figure 4.29: Shear with constant compression test at −2 MPa combined with chemical degradation, load-unload-reload cycles and a parameter value $\gamma = 10$. The graph on the left shows the relative normal displacement r_N in relation to the relative tangential displacement r_T of the interface (dilatancy). The graph on the right shows a zoom of the highlighted part of the image on the left.

Finally, in Figure 4.30 a comparison is made between the results obtained in Tests 8, 13 and 14, i.e. the simulations characterised by the same final chemical degradation value of 0.99, by the same sequences of application of relative shear displacements and chemical degradation and by the same value of constant compression $\sigma_N = -2$ MPa, in which, however, the value of γ is varied, equal to zero, five and ten, respectively.

In Figure 4.30 it can be observed that the variation of γ practically does not affect the behaviour $\sigma_T - r_T$: slight differences in the curves can be appreciated in the first part of the softening branch, while when approaching the residual tangential stress value $|\sigma_N| \tan \phi^+$, i.e. when the variable D is very close to unity and the behaviour is practically governed only by the friction model, the results coincide. However, in Figure 4.31 there is a clear influence on the behaviour of the dilatancy, with a marked effect on the residual normal displacement: for a value of $\gamma = 0$ there is no residual normal displacement, but this value increases with increasing values of γ.

In the original friction model of Snyman and Martin (1992), in the $r_T - r_N$ diagram, when the direction of the tangential displacements is inverted, it always returns to the same point. The modification incorporated in this model through the variable γ, allows to take into account the bulking effect, which is a real effect that has been detected in experimental tests.

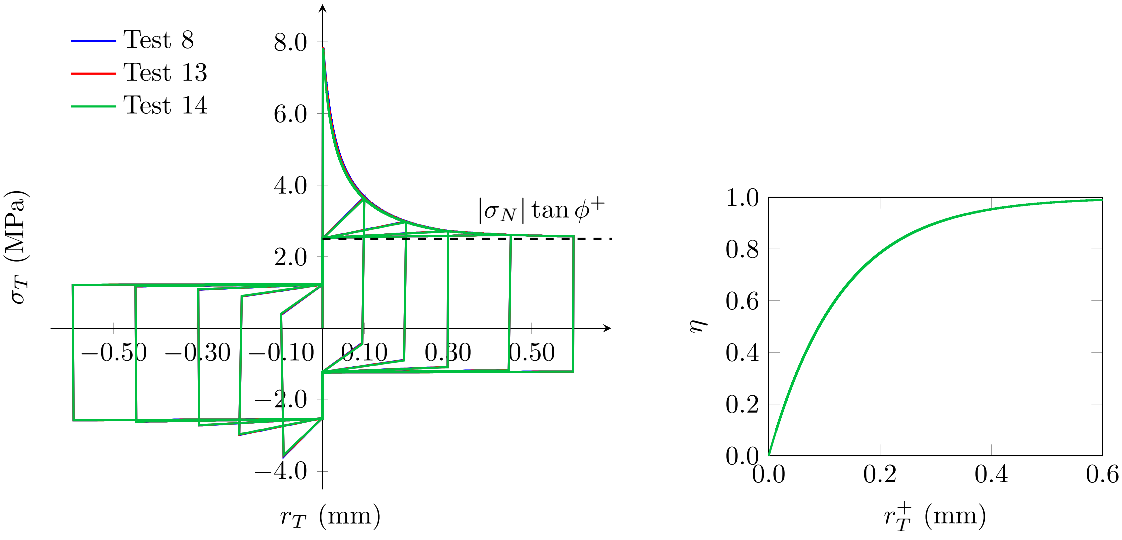

Figure 4.30: Shear with constant compression test at −2 MPa combined with chemical degradation, load-unload-reload cycles and varying γ values. The graph on the left shows the tangential stress σ_T as a function of the relative tangential displacement r_T of the interface. The graph on the right shows the evolution of the chemical degradation η as a function of positive relative tangential displacements.

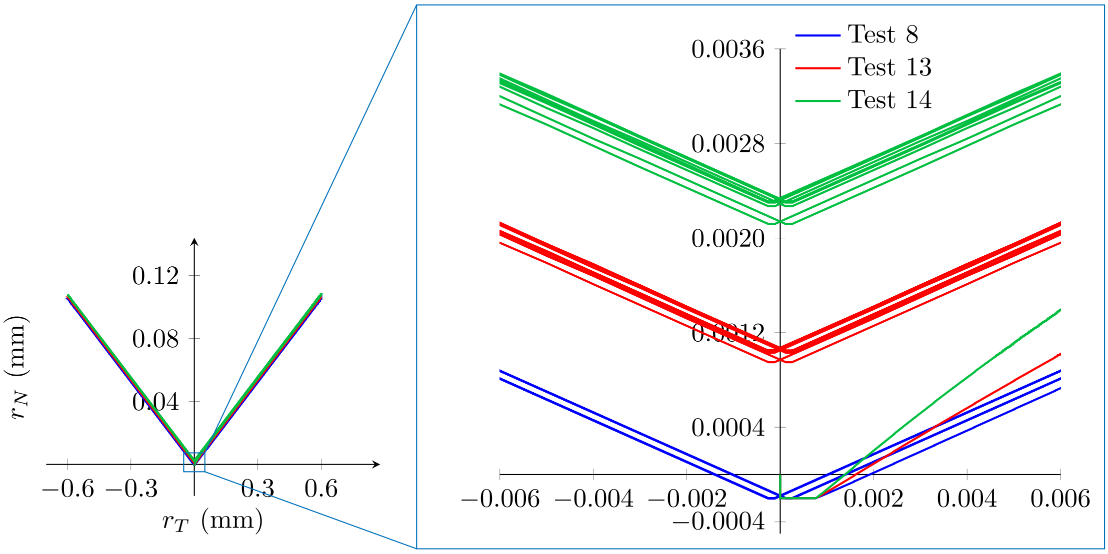

Figure 4.31: Shear with constant compression test at −2 MPa combined with chemical degradation, load-unload-reload cycles and varying γ values. The graph on the left shows the relative normal displacement r_N in relation to the relative tangential displacement r_T of the interface (dilatancy). The graph on the right shows a zoom of the highlighted part of the image on the left.

Chapter 5

Summary, conclusions and future work

A constitutive interface law has been formulated and implemented in which the effect of degradation of material strength parameters due to chemical processes has been incorporated into an existing constitutive law based on damage mechanics combining cohesive behaviour, on the one hand, and frictional behaviour with dilatancy, on the other hand.

The global constitutive law has been determined in a context of homogenisation in terms of nominal or average relative stresses and displacements (the scalar damage and dilatancy friction models are combined in parallel). While the relative displacements are considered the same for both parts of the model, the average stresses in the representative interface area are obtained from the weighted contribution of the stresses acting in the undamaged and damaged areas.

In the isotropic damage model, the degradation of the stiffness matrix depends on the evolution of a single scalar-type variable. The cracking surface is the same as the one used in the elasto-plastic interface model. When cracking starts, the fracture surface starts moving according to the decreasing tensile strength, until it reaches the final state of the hyperbola with apex at the origin, when the strength is exhausted and the damage variable reaches the unit value. The damage-plasticity model has three parameters whose influence can be seen in the examples in Chapter 4: n which is an exponential factor that affects the decay law of χ, and the coefficients β and γ which are factors that affect the plastic relative displacements.

For the component of the model characterising frictional behaviour, the model proposed by Snyman and Martin (1992) has been adopted. This is a formulation that takes into account all possible contact situations between the two surfaces of a discontinuity and allows the restitution of the dilatancy in the loading and unloading cycles.

5.1 Conclusions

The work carried out during the development of this thesis has allowed the following conclusions to be drawn:

- the model has two history variables: an internal one that reflects the deterioration due to the fracture process and which is directly considered by the logarithmic damage variable L, already present in the existing model; and an external one, incorporated in this work, which includes the effect of degradation due to chemical processes. The external history variable (η) is considered in the interface model as a dimensionless given value, between $\eta = 0$ for a non-degraded material, and $\eta = 1$ for a completely degraded material;

- the evolution of the cracking surface is controlled by the evolution of parameter χ, as a function of the internal history variable L and the external history variable η; the evolution of c is defined in such a way that it results in a displacement of the hyperbola to the origin (kinematic softening), and finally the parameter $\tan\phi$ remains constant throughout the degradation process;

- to control the evolution of the fracture surface, an energy parameter corresponding to the classical Mode I fracture energy has been used, which in the new formulation is also reduced as the chemical degradation of the material advances;

- the proposal of Snyman and Martin (1992) has been modified in order to simulate the effect detected in experimental tests that occurs in load-unload cycles of tangential displacements which, on returning to the origin, gives rise to a residual normal displacement (bulking effect). This effect has been taken into account by incorporating in the normal component of the frictional behaviour, the influence of the plastic displacement of the damage-plasticity model, specifically with the use of values of parameter γ greater than zero;

- the performance of the proposed constitutive model has been verified by means of examples at constitutive level subject to some typical loading states: pure tensile, tensile-shear and shear with constant compression, combined with different sequences of chemical degradation;

- the tests that include tensile states show the effect of the damage model, with softening and unloading branch according to a degraded stiffness in each cycle (depending on the parameter that governs the plastic displacement), and with recovery of the initial stiffness value upon unloading as the crack closes and stresses change back to compression values. This was the behaviour sought to adequately represent the total or partial closure of the opening, an aspect that cannot be represented by an elasto-plastic law in which the unloading occurs always according to the initial stiffness value. In the various examples, a higher chemical degradation value implies a more pronounced decay of the softening curve. In the examples illustrating the behaviour with degradation, when unloading and reloading processes take place, it can be seen that, when reloading is carried out after the action of chemical degradation in each phase, a lower point of the softening curve is reached before unloading, with a more pronounced effect as the value of η is higher;

- in shear with constant compression load situations, the new model shows a better behaviour of the shear stress-shear relative displacement diagram, since it reproduces the jump of stresses when passing through the origin and changing the inclination of the asperities. Above all, the improvement is seen in the restitution of the dilatancy in loading and unloading cycles, which in the elasto-plastic model maintains its growth when changing the orientation of the shear displacement, which is unrealistic. The following conclusions refer to the shear examples with constant compression in combination with different chemical degradation sequences;
- the effect of a higher chemical degradation value can be seen in the various examples. In the $\sigma_T - r_T$ graph it can be seen that the curves degrade more with increasing η maximum value and tend to a limit value of $\sigma_T = |\sigma_N| \tan \phi^+$, according to the friction model of Snyman and Martin (1992);
- in the examples showing load-unload-reload processes, it can be seen in the $\sigma_T - r_T$ graphs, that regardless of the degree of chemical degradation, the combined action of the damage and friction models produces a behaviour that is described in detail in Chapter 4; during the complete cycle in which it starts and returns to the point of unloading, the damage variable D remains constant at the value reached at that moment. Regarding the evolution of the dilatancy, it can be seen especially in the magnified image of the corresponding figures, that by varying the trend of the tangential displacements during the loading-unloading-reloading processes, a recovery of the dilatancy occurs when returning to the initial position, and that the degree of chemical degradation does not influence this behaviour;
- the last examples show the effect produced in load-unload cycles of tangential displacements which, on returning to the origin, give rise to a residual normal displacement (bulking effect), which is taken into account in the frictional model with the plastic displacement of the damage-plasticity model, in particular with the use of values of γ greater than zero. This effect has been detected in experimental tests. It can be seen in the figures how the increasing values of γ, practically do not affect the $\sigma_T - r_T$ behaviour, but have a clear influence on the behaviour of dilatancy recovery when returning in unloading to the initial position, with a greater residual normal displacement with the increase in the value of γ (for $\gamma = 0$ there is no residual normal displacement).

5.2 Future work

The model developed has achieved a number of new features, but it can still be improved further in order to incorporate some additional aspects of the constitutive behaviour, which once completed would allow the study of complex structural problems. Some of those possible improvements are mentioned below:

- the frictional behaviour constitutive model would benefit from the incorporation of a law for the deterioration of the angle of the asperities as a function of the work dissipated in the relative sliding of the contact surfaces;
- once the model is completed, its ability to reproduce the dilatancy deterioration in tests on real interface subjected to loading and unloading cycles in shear with constant compression tests available in the literature should be evaluated;
- it would be useful to compare numerical simulations with results obtained in experimental tests with load-unload-reload cycles and exposed to acid-type chemical attacks, but they are not frequently available in literature;
- implementation of the new constitutive law into the research group's finite element code in order to perform more complex structural simulations. These simulations could include tests on a simply supported beam to investigate how the closing and reopening (either partially or fully) of a crack affects the progression of the degradation process within the beam;
- another important example would be the extension of the mechanical analysis carried out in Martínez (2020) on a well system at structural level composed of: rock formation, cement casing, steel pipe and cement plug, in order to assess its integrity due to changes of interstitial pressures in a reservoir during exploitation and abandonment activities. This study, which has highlighted the importance of a constitutive interface law that adequately represents crack closure, could now incorporate the influence of chemical degradation on the material strength. This will allow further analysis of whether stress changes may provide the conditions for the opening and/or propagation of cracks that could potentially become preferential pathways for CO_2 diffusion into the material;
- extension of the model in three dimensions. In the case of the damage-plasticity law, this extension does not seem to pose major difficulties, as has already been done in the elasto-plastic law and also in its extension with chemical degradation (Martínez et al. 2022). The frictional law of Snyman and Martin (1992), formulated in the plane, should be extended to 3D with the above mentioned incorporation of the deterioration of the asperities.

References

Alfano, G., S. Marfia, and E. Sacco (2006). “A cohesive damage–friction interface model accounting for water pressure on crack propagation”. In: *Computer methods in applied mechanics and engineering* 196.1-3, pp. 192–209.

Alfano, G. and E. Sacco (2006). “Combining interface damage and friction in a cohesive-zone model”. In: *International Journal for Numerical Methods in Engineering* 68.5, pp. 542–582.

Amadei, B. et al. (1989). “An evaluation of masonry joint shear strength in existing buildings”. In: *Report to NSF, Department of Civil, Environmental, and Architectural Engineering, University of Colorado, Boulder, EEUU.*

Asamoto, S. et al. (2013). “Well integrity assessment for CO_2 injection: a numerical case study on thermo-mechanical behavior in downhole CO_2 environments”. In: *Engineering Computations* 30.6, pp. 842–853.

Atkinson, R. H. et al. (1989). “Response of masonry bed joints in direct shear”. In: *Journal of Structural Engineering* 115.9, pp. 2276–2296.

Bachu, S. (2003). “Screening and ranking of sedimentary basins for sequestration of CO_2 in geological media in response to climate change”. In: *Environmental Geology* 44.3, pp. 277–289.

Bachu, S. and D. B. Bennion (2009). “Experimental assessment of brine and/or CO_2 leakage through well cements at reservoir conditions”. In: *International Journal of Greenhouse Gas Control* 3.4, pp. 494–501.

Bagheri, M., S. M. Shariatipour, and E. Ganjian (2018). “A review of oil well cement alteration in CO_2-rich environments”. In: *Construction and Building Materials* 186, pp. 946–968.

Barenblatt, G. I. (1962). “The mathematical theory of equilibrium cracks in brittle fracture”. In: *Advances in applied mechanics* 7, pp. 55–129.

Bažant, Z. P. (1976). “Instability, ductility, and size effect in strain-softening concrete”. In: *Journal of the engineering mechanics division* 102.2, pp. 331–344.

Bažant, Z. P. and L. Cedolin (1979). “Blunt crack band propagation in finite element analysis”. In: *Journal of the engineering mechanics division* 105.2, pp. 297–315.

Bažant, Z. P. and P. Gambarova (1980). “Rough cracks in reinforced concrete”. In: *Journal of the Structural Division* 106.4, pp. 819–842.

Bažant, Z. P. and B. H. Oh (1983). “Crack band theory for fracture of concrete”. In: *Matériaux et construction* 16, pp. 155–177.

Borst, R. de and P. Nauta (1985). “Non-orthogonal cracks in a smeared finite element model”. In: *Engineering computations* 2.1, pp. 35–46.

Caballero, A., I. Carol, and C. M. López (2007). “3D meso-mechanical analysis of concrete specimens under biaxial loading”. In: *Fatigue & Fracture of Engineering Materials & Structures* 30.9, pp. 877–886.

Caballero, A., C. M. López, and I. Carol (2006). “3D meso-structural analysis of concrete specimens under uniaxial tension”. In: *Computer methods in applied mechanics and engineering* 195.52, pp. 7182–7195.

Caballero, A., K. Willam, and I. Carol (2008). “Consistent tangent formulation for 3D interface modeling of cracking/fracture in quasi-brittle materials”. In: *Computer Methods in Applied Mechanics and Engineering* 197.33-40, pp. 2804–2822.

Carey, J. W. et al. (2007). “Analysis and performance of oil well cement with 30 years of CO_2 exposure from the SACROC Unit, West Texas, USA”. In: *International journal of greenhouse gas control* 1.1, pp. 75–85.

Carol, I. and C. M. López (1998). “Fracture-based interface model: theory, implementation and applications”. In: *Computational Mechanics—New Trends and Applications: Fourth World Congress on Computational Mechanics, Buenos Aires, Barcelona.*

Carol, I., C. M. López, and O. Roa (2001). “Micromechanical analysis of quasi-brittle materials using fracture-based interface elements”. In: *International Journal for Numerical Methods in Engineering* 52.1-2, pp. 193–215.

Carol, I. and P. Prat (1991). “Smeared analysis of concrete fracture using a microplane based multicrack modell with static constrain”. In: *International Conference on Fracture Processes in Brittle Disordered Materials.*

Carol, I. and P. C. Prat (1990). “A statically constrained microplane model for the smeared analysis of concrete cracking”. In: *Computer aided analysis and design of concrete structures* 2, pp. 919–930.

Carol, I., P. C. Prat, and C. M. López (1997). “Normal/shear cracking model: application to discrete crack analysis”. In: *Journal of engineering mechanics* 123.8, pp. 765–773.

Carol, I., E. Rizzi, and Willam (1994). “A unified theory of elastic degradation and damage based on a loading surface”. In: *International journal of solids and structures* 31.20, pp. 2835–2865.

Carol, I., E. Rizzi, and K. Willam (2001). “On the formulation of anisotropic elastic degradation. I. Theory based on a pseudo-logarithmic damage tensor rate”. In: *International Journal of Solids and Structures* 38.4, pp. 491–518.

Carroll, S. et al. (2016). “Role of chemistry, mechanics, and transport on well integrity in CO_2 storage environments”. In: *International Journal of Greenhouse Gas Control* 49, pp. 149–160.

Choi, Y. S. et al. (2013). “Wellbore integrity and corrosion of carbon steel in CO_2 geologic storage environments: a literature review”. In: *International Journal of Greenhouse Gas Control* 16, S70–S77.

Crow, W. et al. (2010). “Wellbore integrity analysis of a natural CO_2 producer”. In: *International Journal of Greenhouse Gas Control* 4.2, pp. 186–197.

Desai, C. S. et al. (1984). “Thin-layer element for interfaces and joints”. In: *International Journal for Numerical and Analytical Methods in Geomechanics* 8.1, pp. 19–43.

Dowding, C. H. et al. (1991). “Explicit modeling of dilation, asperity degradation and cyclic seating of rock joints”. In: *Computers and Geotechnics* 11.3, pp. 209–227.

Dugdale, D. S. (1960). “Yielding of steel sheets containing slits”. In: *Journal of the Mechanics and Physics of Solids* 8.2, pp. 100–104.

Duguid, A., M. Radonjic, and G. W. Scherer (2011). “Degradation of cement at the reservoir/cement interface from exposure to carbonated brine”. In: *International Journal of Greenhouse Gas Control* 5.6, pp. 1413–1428.

Duguid, A. and G. W. Scherer (2010). “Degradation of oilwell cement due to exposure to carbonated brine”. In: *International journal of greenhouse gas control* 4.3, pp. 546–560.

Fabbri, A., N. Jacquemet, and D. M. Seyedi (2012). “A chemo-poromechanical model of oilwell cement carbonation under CO_2 geological storage conditions”. In: *Cement and Concrete Research* 42.1, pp. 8–19.

Gasda, S. E., S. Bachu, and M. A. Celia (2004). “The potential for CO_2 leakage from storage sites in geological media: analysis of well distribution in mature sedimentary basins”. In: *Environmental Geology* 46.6-7, pp. 707–720.

Gens, A., I. Carol, and E. Alonso (1989). “An interface element formulation for the analysis of soil-reinforcement interaction”. In: *Computers and Geotechnics* 7.1-2, pp. 133–151.

Gens, A., I. Carol, and E.E. Alonso (1995). “Rock joints: FEM implementation and applications”. In: *Studies in Applied Mechanics*. Vol. 42. Elsevier, pp. 395–420.

Ghaboussi, J., E. L. Wilson, and J. Isenberg (1973). “Finite element for rock joints and interfaces”. In: *Journal of the soil mechanics and foundations division* 99.10, pp. 833–848.

Goodman, R. E., R. L. Taylor, and T. L. Brekke (1968). “A model for the mechanics of jointed rock”. In: *Journal of the soil mechanics and foundations division* 94.3, pp. 637–659.

Griffith, A. A. (1921). “The phenomena of rupture and flow in solids”. In: *Philosophical Transactions of the Royal Society of London* 221, pp. 163–198.

Hawkes, C. D., P. J. McLellan, and S. Bachu (2005). “Geomechanical factors affecting geological storage of CO_2 in depleted oil and gas reservoirs”. In: *Journal of Canadian Petroleum Technology* 44.10.

Hillerborg, A. (1978). *A model for fracture analysis.* Division of Building Materials, LTH, Lund University.

Hillerborg, A., M. Modéer, and P. E. Petersson (1976). “Analysis of crack formation and crack growth in concrete by means of fracture mechanics and finite elements”. In: *Cement and concrete research* 6.6, pp. 773–781.

Hohberg, J. M. (1992). *A joint element for the nonlinear dynamic analysis of arch dams.* Vol. 186. Birkhäuser.

Idiart, A. E, C. M. López, and I. Carol (2011). “Modeling of drying shrinkage of concrete specimens at the meso-level”. In: *Materials and structures* 44, pp. 415–435.

Inglis, C. E. (1913). “Stresses in a plate due to the presence of cracks and sharp corners”. In: *Transactions of the Royal Institution of Naval Architects* 55, pp. 219–241.

Irwin, G. (1958). “Fracture”. In: *Encyclopedia of Physics* VI, pp. 551–590.

Jefferson, A. D. (2002). “Tripartite cohesive crack model”. In: *Journal of engineering mechanics* 128.6, pp. 644–653.

Karihaloo, B. L. (1995). “Fracture mechanics & structural concrete”. In: *Longman Scientific and Technical.*

Kutchko, B. G., B. R. Strazisar, D. A. Dzombak, et al. (2007). “Degradation of well cement by CO_2 under geologic sequestration conditions”. In: *Environmental science & technology* 41.13, pp. 4787–4792.

Kutchko, B. G., B. R. Strazisar, G. V. Lowry, et al. (2008). “Rate of CO_2 attack on hydrated class H well cement under geologic sequestration conditions”. In: *Environmental science & technology* 42.16, pp. 6237–6242.

Liaudat, J., C. M. López, and I. Carol (2018). “Coupled CM meso-scale model for ASR expansion in concrete”. In: *Computational Modelling of Concrete Structures.* CRC Press, pp. 363–370.

López, C. M. (1999). “Análisis microestructural de la fractura del hormigón utilizando elementos finitos tipo junta. Aplicación a diferentes hormigones”. PhD thesis. Universitat Politécnica de Catalunya.

López, C. M., I. Carol, and A. Aguado (2008). “Meso-structural study of concrete fracture using interface elements. I: numerical model and tensile behavior”. In: *Materials and structures* 41, pp. 583–599.

López, C. M., L. Puiggrós, and I. Carol (2024). “Modelo constitutivo de junta basado en la mecánica de daño, plasticidad y fractura”. In: *Anales de Mecánica de la Fractura, 40. Congreso del Grupo Español de Fractura, 6-8 de Marzo de 2024, Palma de Mallorca. España.*

Lotfi, H. R. and P. B. Shing (1994). “Interface model applied to fracture of masonry structures”. In: *Journal of structural engineering* 120.1, pp. 63–80.

Mainguy, M. et al. (2007). “Analyzing the risk of well plug failure after abandonment”. In: *Oil & Gas Science and Technology-Revue de l’IFP* 62.3, pp. 311–324.

Martínez, A. (2020). “Estudio numérico del ataque ácido por CO_2 en cementos de pozos de petróleo sellados”. PhD thesis. Universitat Politècnica de Catalunya.

Martínez, A. et al. (2022). “3D zero-thickness interface model for fracture of cement-based materials with chemical degradation”. In: *International Journal of Solids and Structures* 238, p. 111379.

Mason, H. E. et al. (2013). “Chemical and mechanical properties of wellbore cement altered by CO_2-rich brine using a multianalytical approach”. In: *Environmental science & technology* 47.3, pp. 1745–1752.

Metz, B. et al. (2005). *IPCC special report on carbon dioxide capture and storage.* Cambridge: Cambridge University Press.

Nelson, E. B. (1990). *Well cementing.* Newnes.

Onan, D. D. (1984). "Effects of supercritical carbon dioxide on well cements". In: *SPE Permian Basin Oil and Gas Recovery Conference.* SPE, SPE–12593.

Orlic, B. (2009). "Some geomechanical aspects of geological CO_2 sequestration". In: *KSCE Journal of Civil Engineering* 13.4, pp. 225–232.

Pande, G., G. Beer, and J. Williams (1990). "Numerical methods in rock mechanics". In: *New York, NY (USA); John Wiley and Sons Inc.*

Papadakis, V. G., C. G. Vayenas, and M. N. Fardis (1991). "Fundamental modeling and experimental investigation of concrete carbonation". In: *Materials Journal* 88.4, pp. 363–373.

Plesha, M. E. (1987). "Constitutive models for rock discontinuities with dilatancy and surface degradation". In: *International journal for numerical and analytical methods in geomechanics* 11.4, pp. 345–362.

Plesha, M. E., R. Ballarini, and A. Parulekar (1989). "Constitutive model and finite element procedure for dilatant contact problems". In: *Journal of engineering mechanics* 115.12, pp. 2649–2668.

Prat, P. C. et al. (1993). "DRAC: a computer software for the analysis of rock mechanics problems". In: *Application of computer methods in rock mechanics. Shaanxi Science and Technology Press, Xian, China* 13611368.

Puiggrós, L. (2017). "Modelo de comportamiento de juntas basado en la mecánica de daño, plasticidad y fractura". MA thesis. Universitat Politècnica de Catalunya.

Rimmelé, G. et al. (2008). "Heterogeneous porosity distribution in Portland cement exposed to CO_2-rich fluids". In: *Cement and Concrete Research* 38.8-9, pp. 1038–1048.

Robins, N. S. and A. E. Milodowski (1986). "Borehole cements and the downhole environment — a review". In: *Quarterly Journal of Engineering Geology and Hydrogeology* 19.2, pp. 175–181.

Rots, J. G. (1988). "Computational modeling of concrete fracture". PhD thesis. Technische Hogeschool Delft.

Rutqvist, J. (2012). "The geomechanics of CO_2 storage in deep sedimentary formations". In: *Geotechnical and Geological Engineering* 30, pp. 525–551.

Segura, J. M. and I. Carol (2008). "Coupled HM analysis using zero-thickness interface elements with double nodes. Part I: Theoretical model". In: *International journal for numerical and analytical methods in geomechanics* 32.18, pp. 2083–2101.

Shukla, R. et al. (2010). "A review of studies on CO_2 sequestration and caprock integrity". In: *Fuel* 89.10, pp. 2651–2664.

Snyman, M. F., W. W. Bird, and J. B. Martin (1991). "A simple formulation of a dilatant joint element governed by Coulomb friction". In: *Engineering computations* 8.3, pp. 215–229.

Snyman, M. F. and J. B. Martin (1992). “A consistent formulation of a dilatant interface element”. In: *International journal for numerical and analytical methods in geomechanics* 16.7, pp. 493–527.

Stankowski, T., K. Runesson, and S. Sture (1993). “Fracture and slip of interfaces in cementitious composites. I: Characteristics”. In: *Journal of engineering mechanics* 119.2, pp. 292–314.

Teodoriu, C. et al. (2013). “Wellbore integrity and cement failure at HPHT conditions”. In: *International Journal of Engineering* 2.2, pp. 2305–8269.

Timoshenko, S. P. and J. N. Goodier (1970). “Theory of Elasticity”. In: *McGraw-Hill* 3rd Edition.

Vonk, R. A. (1992). “Softening of concrete loaded in compression”. PhD thesis. Eindhoven University of Technology, Eindhoven (Netherland).

Walraven, J. C. (1980). “Aggregate interlock: a theoretical and experimental analysis”. PhD thesis. Delft University Press.

Walraven, J. C. and H. W. Reinhardt (1981). “Concrete mechanics. Part A: Theory and experiments on the mechanical behavior of cracks in plain and reinforced concrete subjected to shear loading”. In: *Nasa Sti/recon Technical Report N* 82, p. 25417.

Walsh, S. D. C. et al. (2013). “Permeability of wellbore-cement fractures following degradation by carbonated brine”. In: *Rock Mechanics and Rock Engineering* 46, pp. 455–464.

Weihe, S., M. König, and B. Kröplin (1994). “A treatment of mixed mode fracture in debonding”. In: *Computational materials science* 3.2, pp. 254–262.

Zhang, M. and S. Bachu (2011). “Review of integrity of existing wells in relation to CO_2 geological storage: What do we know?” In: *International Journal of Greenhouse Gas Control* 5.4, pp. 826–840.

Zienkiewicz, O. C. et al. (1970). “Analysis of non linear problems in rock mechanics with particular reference to jointed rock systems”. In: *ISRM Congress*. ISRM, ISRM–2CONGRESS.